

**INSTITUTO TECNOLÓGICO DE AERONÁUTICA**



**Mateus Silva Borges**

**ADAPTIVE CONTROL STRATEGIES FOR BASELINE  
MAINTENANCE IN MULTI-SATELLITE SAR  
FORMATIONS**

Final Paper  
2025

**Course of Aerospace Engineering**

**Mateus Silva Borges**

**ADAPTIVE CONTROL STRATEGIES FOR BASELINE  
MAINTENANCE IN MULTI-SATELLITE SAR  
FORMATIONS**

Advisor

Prof. Dr. Willer Gomes dos Santos (ITA)

Co-advisor

Prof<sup>a</sup>. Dr<sup>a</sup>. Francesca Scala (DLR)

**AEROSPACE ENGINEERING**

**SÃO JOSÉ DOS CAMPOS**  
**INSTITUTO TECNOLÓGICO DE AERONÁUTICA**

**Cataloging-in Publication Data**  
**Documentation and Information Division**

Silva Borges, Mateus  
Adaptive Control Strategies for Baseline Maintenance in Multi-Satellite SAR Formations /  
Mateus Silva Borges.  
São José dos Campos, 2025.  
98f.

Final paper (Undergraduation study) – Course of Aerospace Engineering– Instituto Tecnológico de Aeronáutica, 2025. Advisor: Prof. Dr. Willer Gomes dos Santos. Co-advisor: Prof<sup>a</sup>. Dr<sup>a</sup>. Francesca Scala.

1. Synthetic Aperture Radar. 2. Formation Flying. 3. Control. 4. Optimization. I. Instituto Tecnológico de Aeronáutica. II. Title.

**BIBLIOGRAPHIC REFERENCE**

SILVA BORGES, Mateus. **Adaptive Control Strategies for Baseline Maintenance in Multi-Satellite SAR Formations**. 2025. 98f. Final paper (Undergraduation study) – Instituto Tecnológico de Aeronáutica, São José dos Campos.

**CESSION OF RIGHTS**

AUTHOR'S NAME: Mateus Silva Borges

PUBLICATION TITLE: Adaptive Control Strategies for Baseline Maintenance in Multi-Satellite SAR Formations.

PUBLICATION KIND/YEAR: Final paper (Undergraduation study) / 2025

It is granted to Instituto Tecnológico de Aeronáutica permission to reproduce copies of this final paper and to only loan or to sell copies for academic and scientific purposes. The author reserves other publication rights and no part of this final paper can be reproduced without the authorization of the author.

---

Mateus Silva Borges  
Rua H8B, Ap. 214  
12.228-461 – São José dos Campos–SP

# ADAPTIVE CONTROL STRATEGIES FOR BASELINE MAINTENANCE IN MULTI-SATELLITE SAR FORMATIONS

This publication was accepted like Final Work of Undergraduation Study

---

Mateus Silva Borges

Author

---

Willer Gomes dos Santos (ITA)

Advisor

---

Francesca Scala (DLR)

Co-advisor

Aos meus pais, Cremilda e Waldemir,  
por todo o amor e apoio em cada etapa  
desta jornada.

# Acknowledgments

Agradeço aos meus pais, Cremilda e Waldemir, por terem me apoiado em cada decisão e acreditado em cada passo desta jornada. Sei que fizeram tudo o que podiam para me proporcionar a melhor educação possível e, sem o amor de vocês, eu não teria chegado até aqui.

Agradeço por todas as amizades que essa jornada trouxe e que levarei para vida. Ao meu amigo, Felipe Marquezini, por todas as aventuras gastronômicas e propostas de rolês indecorosos que tornaram os anos de ITA ainda mais divertidos e memoráveis. À minha amiga, Ana Beatriz, por todas as conversas, cafézinhos e apoio em todos os momentos, especialmente nos mais difíceis.

Aos meus amigos, João Raphael, Marcelo de Deus, Pedro Batista, Fernando Victor, Arthur Stevenson e Emmanuel da Silva, que em meio ao caos das noites e dos rolês mais aleatórios, tornaram as tortuosas semanas de estudo mais leves e divertidas. Ao meu amigo Galba, com quem, neste último ano dessa jornada, compartilhei o quarto, os estudos, o trabalho, os dias difíceis no mar e até mesmo a família que me acolheu e me fez sentir em casa.

Aos meus amigos Rafael Bueno, Luísa Dallmann, Victor Bustos, Luis Felipe e Mateus Miranda, que me acompanharam em nossas aventuras europeias e que, apesar da distância, fizeram-me sentir mais próximo de casa. Agradeço pelas resenhas diárias na sala dos maninhos, pelos rolês nos confins de Fürstfeldbruck, pelos jogos de totó, pelas competições de pontos e pelas viagens inesquecíveis. Agradeço também aos meus amigos e colegas de apartamento, Vinícius e Cecília, que estiveram comigo em meio ao caos do cotidiano, garantindo que nenhum neurônio sobrasse ileso no fim do dia.

Gostaria de agradecer também aos meus familiares Joice, Nice, Rosângela e Renilda; aos meus amigos de infância, Roberto, Ayalla e Rebeca; e às amigas, Erica, Waldelice e Nilza, que foram como mães e tias para mim, cuidando de mim com tanto carinho, que, mesmo de longe, sempre me apoiaram e torceram por mim. Por fim, agradeço a todos os meus professores e orientadores, que me guiaram com sabedoria e me ensinaram muito mais do que estava nas páginas dos livros.

*“It is the mark of an educated man  
to look for precision in each class of things  
just so far as the nature of the subject admits”*

— ARISTOTLE

# Resumo

Aplicações de Radar de Abertura Sintética (SAR) multi-satélite beneficiam-se significativamente de conceitos distribuídos, como satélites voando em formação. A tendência de missões SAR baseadas em pequenos satélites viabiliza o uso de propulsores mais eficientes, particularmente motores elétricos e de íons, para a manutenção da linha de base. Este estudo foca na otimização de controladores lineares contínuos para a manutenção da linha de base em formações SAR multi-satélite. O método proposto aborda os desafios de ajuste dos parâmetros de controladores lineares contínuos, como as matrizes de peso no Regulador Linear Quadrático (LQR) e os ganhos de controle em controladores Proporcional-Integral-Derivativo (PID), identificando a combinação ideal de algoritmos e estratégias de otimização. Essa abordagem facilita o desenvolvimento de um regulador autoajustável robusto e flexível, capaz de lidar com diversos erros de estado, geometrias de formação e perturbações ou incertezas do sistema, resultando em uma estratégia de controle adaptativo para a dinâmica de voo em formação. Os resultados desta análise podem ser aplicados no design preliminar de missões, operações do segmento terrestre e implementações a bordo, possibilitando um ajuste eficiente e adaptativo em tempo real.

# Abstract

Multi-satellite Synthetic Aperture Radar (SAR) applications benefit significantly from distributed concepts, such as satellites formation flying. The trend toward small satellite-based SAR missions enables the use of more efficient thrusters, particularly electric and ion engines, for baseline maintenance. This study focuses on optimizing continuous linear controllers for baseline maintenance in multi-satellite SAR formations. The proposed method addresses the challenges in tuning the parameters of continuous linear controllers, such as the weight matrices in the Linear Quadratic Regulator (LQR) and the control gains in Proportional-Integral-Derivative (PID) controllers, by identifying the optimal combination of optimization algorithms and strategies. This approach facilitates the development of a robust and flexible self-tuning regulator capable of handling various state errors, formation geometries, and system perturbations or uncertainties, resulting in an adaptive control strategy for formation flying dynamics. The results of this analysis can be applied to preliminary mission design, ground segment operations, and onboard implementations, enabling efficient and adaptive online tuning.

# List of Figures

<p>FIGURE 1.1 – HELIX satellite formation for TanDEM-X. (Left) Orbital arrangement. (Right) Cross-track baselines as function of the orbit position. The positions correspond to one complete orbit cycle, where NH and SH mean Northern and Southern Hemispheres, respectively (Krieger <i>et al.</i>, 2007). . . . .</p>	21
<p>FIGURE 3.1 – Illustration of the SAR imaging geometry. <math>r(t)</math> stands for the shortest approach distance, <math>\Theta_a</math> for the azimuth beamwidth and <math>v</math> for the sensor velocity (Moreira <i>et al.</i>, 2013). . . . .</p>	30
<p>FIGURE 3.2 – Across-track SAR interferometry employs antennas that move on parallel but mutually displaced flight paths (the flight paths are not shown since they are pointing into the page). The slant range <math>r_0</math>, the incident angle <math>\theta_i</math> and the effective baseline <math>B_{\perp}</math> are all defined in a plane perpendicular to the flight paths. A change in the surface height by <math>\Delta h</math> causes a change in the range difference by <math>\Delta r</math> (Moreira <i>et al.</i>, 2013). . . . .</p>	31
<p>FIGURE 3.3 – The Earth-centered inertial (ECI) coordinate system. Also shown are <math>r</math> and <math>v</math>, the position and velocity vectors, respectively, as well as the right ascension, <math>\alpha_r</math>, and the declination, <math>\delta_d</math> (Alfriend <i>et al.</i>, 2010). . . . .</p>	33
<p>FIGURE 3.4 – Local-vertical, local-horizon rotating coordinate system, centered at the spacecraft (Alfriend <i>et al.</i>, 2010). . . . .</p>	34
<p>FIGURE 3.5 – Relative motion of two bodies in an inertial reference frame (Curtis, 2014). . . . .</p>	34
<p>FIGURE 3.6 – Geocentric equatorial frame and the orbital elements (Curtis, 2014). . . . .</p>	36
<p>FIGURE 3.7 – Central acceleration and perturbative accelerations as a function of the distance <math>r</math> of the satellite from the center of the Earth, shown on a log-log scale (Capderou, 2014). . . . .</p>	38

FIGURE 3.8 – Sun-synchronous Condition: Inclination vs. Altitude ( $e = 0$ ) (Boain, 2005).	39
FIGURE 3.9 – Rotating Euler–Hill frame, centered at the chief spacecraft (Alfriend <i>et al.</i> , 2010).	40
FIGURE 3.10 – 3D relative motion and its projection on the coordinate planes for a formation with $e = 0.001$ , $a = 7,000$ km, $\delta e = 1 \times 10^{-4}$ , $\delta \Omega = 0.005^\circ$ , and different choices for the two perigees ( $0^\circ, 45^\circ, 90^\circ$ ) (D’Errico, 2012).	44
FIGURE 3.11 – Evolution of TDX-TSX relative motion in the Hill frame: radial/along-track separation (left) and radial/normal separation (right). The formation geometries were flown during the period from December 2010 (dotted ellipse) to December 2011 (bold black ellipse). Arrows indicate the relative motion direction. The filled black circle indicates the TDX relative position at $90^\circ$ argument of latitude (Kahle <i>et al.</i> , 2012; D’Errico, 2012).	45
FIGURE 3.12 – Transient response of a unit-step input showing rise time, overshoot, settling time, and steady-state error (Ogata, 2002).	49
FIGURE 3.13 – Classification of metaheuristic methods (Naimi Sadigh <i>et al.</i> , 2012).	52
FIGURE 3.14 – A Pareto-optimal set (LIU; YANG; WHIDBORNE, 2003).	56
FIGURE 4.1 – Simulation test scenarios for the geometry-independence hypothesis.	63
FIGURE 4.2 – Simulation test scenarios for the optimization analysis.	64
FIGURE 4.3 – Simulation workflow.	64
FIGURE 5.1 – Representation of the fitness function landscape for an optimization problem with 2 decision variables. The horizontal and vertical axes represent controller decision variables, while the color map shows the objective function value to be minimized. The crosses indicate the best solutions found for each group, and the red dot indicates the overall best solution.	72
FIGURE 5.2 – Comparison of the mean values of the objective function estimation for each algorithm in the multiobjective optimization of the LQR controller across different formation geometries. The y-axis represents the average estimated value of the objective function, which is the daily control usage $\Delta V$ . The x-axis lists the optimization algorithms used.	73

FIGURE 5.3 – Comparison of the mean values of the objective function estimation for each algorithm in the single objective optimization of the LQR controller across different formation geometries. The y-axis represents the average estimated value of the objective function, which is the daily control usage $\Delta V$ . The x-axis lists the optimization algorithms used. . . . .	74
FIGURE 5.4 – Simulation of LQR controller with the literature-suggested (Alfriend <i>et al.</i> , 2010) weighting matrices using the unperturbed reference formation. (a) State error evolution; (b) Control acceleration profile. . . . .	76
FIGURE 5.5 – Simulation of LQR controller with the literature (Alfriend <i>et al.</i> , 2010) inspired weighting matrices using the unperturbed reference formation. (a) State error evolution; (b) Control acceleration profile. . . . .	77
FIGURE 5.6 – Mean estimation of the single objective optimization of the LQR controller for the TDX geometry tracking the unperturbed reference trajectory. . . . .	78
FIGURE 5.7 – Mean estimation of the single objective optimization of the LQR controller for the TDX geometry tracking the perturbed reference trajectory. . . . .	79
FIGURE 5.8 – Simulation of LQR controller with the single objective optimized weighting matrices using the unperturbed reference formation. (a) State error evolution; (b) Control acceleration profile. . . . .	80
FIGURE 5.9 – Mean estimation of the single objective optimization of the LQR controller for the TDX geometry tracking the perturbed reference trajectory without radial thrust. . . . .	80
FIGURE 5.10 – Mean estimation of the multiobjective optimization of the LQR controller for the TDX geometry tracking the unperturbed reference trajectory. . . . .	81
FIGURE 5.11 – Simulation of LQR controller with the multiobjective optimized weighting matrices using the unperturbed reference formation. (a) State error evolution; (b) Control acceleration profile. . . . .	82
FIGURE 5.12 – Mean estimation of the multiobjective optimization of the LQR controller for the TDX geometry tracking the perturbed reference trajectory. . . . .	83
FIGURE 5.13 – Mean estimation of the multiobjective optimization of the LQR controller for the TDX geometry tracking the perturbed reference trajectory without radial thrust. . . . .	83

---

FIGURE 5.14 –Root locus of the closed-loop system with a PID controller for the Z-axis, showing the effect of varying the proportional gain ( $K_p$ ) on the pole locations. . . . .	85
FIGURE 5.15 –Root locus of the closed-loop system with a PID controller for the X and Y axes, showing the effect of varying the proportional gain ( $K_p$ ) on the pole locations. . . . .	86
FIGURE 5.16 –Simulation of the PID controller with the literature (Ogata, 2010) inspired Ziegler-Nichols method using the unperturbed reference formation. (a) State error evolution; (b) Control acceleration profile. . . . .	87
FIGURE 5.17 –Mean estimation of the single objective optimization of the PID controller for the TDX geometry tracking the unperturbed reference trajectory. . . . .	88
FIGURE 5.18 –Simulation of PID controller with the multiobjective optimized weighting matrices using the unperturbed reference formation. (a) State error evolution; (b) Control acceleration profile. . . . .	89

# List of Tables

TABLE 3.1 – Ziegler–Nichols tuning rules based on the critical gain $K_{cr}$ and the critical period $P_{cr}$ (second method) (Ogata, 2010) . . . . .	51
TABLE 4.1 – Comparison of Programming Languages for Simulation and Optimization . . . . .	59
TABLE 4.2 – Formation geometry and initial conditions for the simulation scenarios.	63
TABLE 4.3 – Numerical integration parameters. . . . .	65
TABLE 4.4 – Bounds of the optimization variables. . . . .	65
TABLE 4.5 – Summary of decision variable sets for LQR optimization. . . . .	67
TABLE 4.6 – Summary of decision variable sets for PID controller optimization. .	68
TABLE 5.1 – Comparison of the controllers performance tracking the unperturbed reference. . . . .	89
TABLE 5.2 – Comparison of the LQR controllers performance tracking the perturbed reference. . . . .	90

# List of Abbreviations and Acronyms

ACO	Ant Colony Optimization
AIAA	American Institute of Aeronautics and Astronautics
CMA-ES	Covariance Matrix Adaptation Evolution Strategy
DE	Differential Evolution
DLR	German Space Center (Deutsches Zentrum für Luft- und Raumfahrt)
DEM	Digital Elevation Model
ECI	Earth-Centered Inertial
FF	Formation Flying
GA	Genetic Algorithm
GMAT	General Mission Analysis Tool
GMOEAD	Multiobjective Evolutionary Algorithm with Decomposition Generational
LQR	Linear Quadratic Regulator
LVLH	Local-Vertical Local-Horizontal
MHACO	Multiobjective Hypervolume-based Ant Colony Optimization
MOEAD	Multiobjective Evolutionary Algorithm with Decomposition
NSGA2	Non-dominated Sorting Genetic Algorithm II
NSPSO	Non-dominated Sorting Particle Swarm Optimization
P	Proportional
PD	Proportional-Derivative
PI	Proportional-Integral
PID	Proportional-Integral-Derivative
PSO	Particle Swarm Optimization
ROE	Relative Orbital Elements
SA	Simulated Annealing
SADE	Self-Adaptive Differential Evolution
SAR	Synthetic Aperture Radar
SGA	Simple Genetic Algorithm
SSO	Sun-Synchronous Orbit
TSX	TerraSAR-X
TDX	TanDEM-X

# List of Symbols

$a_0$	Semi-major axis of the chief satellite's orbit
$A$	State matrix in state-space representation
$B_{\perp}$	Perpendicular baseline for SAR interferometry
$B$	Input matrix in state-space representation
$C(s)$	Controller transfer function
$d_x, d_y, d_z$	Orbital disturbances not modelled
$e$	Eccentricity of an orbit
$e(t)$	Error signal as a function of time
$e_0$	Eccentricity of the chief satellite's orbit
$e_{ss}$	Steady-state error of a dynamical system time-domain response
$E_0$	Allowable error tolerance
$E(s)$	Laplace Transform of the error signal
$f_0$	True anomaly of the chief satellite
$f_l$	Objective function of the referenced objective $l$
$F$	Feasible region defined by the constraints
$G$	Universal gravitational constant
$G(s)$	Transfer function of a system
$G_p(s)$	Transfer function of a system plant
$h$	Specific angular momentum of an orbit
$i_0$	Inclination of the chief satellite's orbit
$\mathcal{J}$	LQR cost function
$\mathcal{J}_{ITAE}$	Integral of Time-weighted Absolute Error
$K$	LQR optimal feedback gain matrix
$K_{cr}$	Critical gain of a dynamical system time-domain response
$K_d$	Derivative gain of a PID controller
$K_i$	Integral gain of a PID controller
$K_p$	Proportional gain of a PID controller
$m_1, m_2$	Mass of body 1 and body 2, respectively
$M_0$	Mean anomaly of the chief satellite
$\dot{M}_0$	Mean motion of the chief satellite ( $n_0$ )

---

$M_p$	Overshoot metric of a dynamical system time-domain response
$n$	Sample size for statistical analysis
$n_0$	Mean motion of the chief satellite
$P$	Solution matrix of the Algebraic Riccati Equation (ARE)
$P_{cr}$	Critical period of a dynamical system time-domain response
$Q$	State-weighting matrix for LQR
$S$	Solution of the algebraic Riccati Equation
$r(t)$	Shortest approach distance between SAR sensor and target
$r_0$	Magnitude of the chief satellite's position vector, $\ \mathbf{r}_0\ $
$\mathbf{r}$	Relative position vector between two bodies
$\ddot{\mathbf{r}}$	Relative acceleration vector between two bodies
$\mathbf{r}_0$	Inertial position vector of the chief satellite
$\ddot{\mathbf{r}}_0$	Inertial acceleration vector of the chief satellite
$\mathbf{r}_1$	Inertial position vector of the deputy satellite
$\ddot{\mathbf{r}}_1$	Inertial acceleration vector of the deputy satellite
$R$	Control-weighting matrix for LQR
$\mathbf{R}_1, \mathbf{R}_2$	Inertial position vectors of body 1 and body 2
$\mathbf{R}_G$	Inertial position vector of the two-body system's center of mass
$t_p$	Peak time of a dynamical system time-domain response
$t_r$	Rise time of a dynamical system time-domain response
$t_s$	Settling time of a dynamical system time-domain response
$\hat{\mathbf{u}}_r$	Radial unit vector in the rotating reference frame
$T_d$	Derivative time constant of the PID controller
$T_i$	Integral time constant of the PID controller
$U(s)$	Laplace Transform of the control input
$U_z(s)$	Laplace Transform of the control input in the Z-axis
$\mathbf{U}$	Control input vector
$u_x, u_y, u_z$	Scalar components of the control input vector $\mathbf{U}$
$v$	Platform velocity in the azimuth direction
$\mathbf{X}$	State vector
$\dot{\mathbf{X}}$	Time derivative of the state vector
$x, y, z$	Components of the relative position vector $\boldsymbol{\rho}$ in the rotating frame
$\dot{x}, \dot{y}, \dot{z}$	Components of the relative velocity vector $\dot{\boldsymbol{\rho}}$ in the rotating frame
$\ddot{x}, \ddot{y}, \ddot{z}$	Components of the relative acceleration vector $\ddot{\boldsymbol{\rho}}$ in the rotating frame
$y(t)$	Output signal as a function of time
$Y(s)$	Laplace Transform of the output signal
$Z(s)$	Transfer function of the Z-axis output
$Z_{\alpha/2}$	Critical value from the standard normal distribution

---

$\delta a$	Relative semi-major axis
$\delta h$	Topographic height variation
$\delta \lambda$	Relative mean argument of latitude
$\delta \dot{\lambda}$	Relative rate of the mean argument of latitude
$\delta n$	Relative mean motion
$\delta r$	Change in the interferometric range difference
$\delta \Omega$	Relative right ascension of the ascending node
$\epsilon$	Constrain upper bound
$\phi_1, \phi_2$	Optimization objective functions
$\lambda_0$	Mean argument of latitude of the chief satellite
$\mu$	Standard gravitational parameter, $G(m_1 + m_2)$
$\boldsymbol{\rho}$	Relative position vector from chief to deputy satellite ( $\mathbf{r}_1 - \mathbf{r}_0$ )
$\ddot{\boldsymbol{\rho}}$	Relative acceleration vector between deputy and chief
$\sigma$	Estimated standard deviation
$\theta_i$	Incidence angle for across-track SAR interferometry
$\theta_0$	Argument of latitude of the chief satellite
$\dot{\theta}_0$	Rate of change of the chief's argument of latitude
$\ddot{\theta}_0$	Second time derivative of the chief's argument of latitude
$\Theta_a$	Antenna beamwidth in the azimuth direction
$\omega_0$	Argument of perigee of the chief satellite's orbit
$\Omega_0$	Right ascension of the ascending node of the chief satellite's orbit

# Contents

1	INTRODUCTION . . . . .	21
1.1	<b>Problem definition</b> . . . . .	21
1.2	<b>Hypotheses</b> . . . . .	23
1.3	<b>Objectives</b> . . . . .	23
1.4	<b>Motivation</b> . . . . .	24
1.5	<b>Work Organization</b> . . . . .	25
2	LITERATURE REVIEW . . . . .	26
2.1	<b>Formation Flying for Synthetic Aperture Radar</b> . . . . .	26
2.2	<b>Formation Flying Control</b> . . . . .	27
2.3	<b>Control Cost Optimization</b> . . . . .	28
3	THEORETICAL FOUNDATION . . . . .	29
3.1	<b>Synthetic Aperture Radar</b> . . . . .	29
3.1.1	Interferometry . . . . .	30
3.1.2	TanDEM-X Mission . . . . .	32
3.2	<b>Orbital Mechanics</b> . . . . .	32
3.2.1	Coordinates Systems . . . . .	33
3.2.2	Equations of Motion . . . . .	34
3.2.3	Orbital Elements . . . . .	35
3.2.4	Orbital Perturbations . . . . .	37
3.2.5	Sun-Synchronous Orbit . . . . .	39
3.3	<b>Formation Flying</b> . . . . .	40
3.3.1	Relative Dynamics . . . . .	40

---

3.3.2	Linear Equations of Relative Motion . . . . .	42
3.3.3	Helix Formation . . . . .	42
<b>3.4</b>	<b>Control Theory . . . . .</b>	<b>45</b>
3.4.1	Linear Quadratic Regulator Controller . . . . .	47
3.4.2	Frequency Domain . . . . .	48
3.4.3	Time Domain . . . . .	48
3.4.4	Proportional-Integral-Derivative (PID) Controller . . . . .	50
3.4.5	Ziegler-Nichols Tuning Method . . . . .	51
<b>3.5</b>	<b>Optimization . . . . .</b>	<b>51</b>
3.5.1	Metaheuristics Methods . . . . .	52
3.5.2	Multiobjective Optimization . . . . .	54
3.5.3	Statistical Validation Framework . . . . .	56
<b>4</b>	<b>METHODOLOGY . . . . .</b>	<b>58</b>
<b>4.1</b>	<b>Software . . . . .</b>	<b>58</b>
<b>4.2</b>	<b>Classical Control Analysis . . . . .</b>	<b>60</b>
4.2.1	Proportional (P) Controller . . . . .	60
4.2.2	Proportional-Integral (PI) Controller . . . . .	60
4.2.3	Proportional-Derivative (PD) Controller . . . . .	61
4.2.4	Proportional-Integral-Derivative (PID) Controller . . . . .	61
<b>4.3</b>	<b>Simulation . . . . .</b>	<b>62</b>
<b>4.4</b>	<b>Decision Variables . . . . .</b>	<b>66</b>
<b>4.5</b>	<b>Statistical Analysis . . . . .</b>	<b>68</b>
<b>5</b>	<b>NUMERICAL RESULTS AND DISCUSSION . . . . .</b>	<b>71</b>
<b>5.1</b>	<b>Geometry-Independence Hypothesis . . . . .</b>	<b>72</b>
<b>5.2</b>	<b>Linear Quadratic Regulator (LQR) . . . . .</b>	<b>75</b>
5.2.1	Reference Study Case . . . . .	75
5.2.2	Single Objective Optimization . . . . .	77
5.2.3	Multiobjective Optimization . . . . .	81
<b>5.3</b>	<b>Proportional-Integral-Derivative (PID) Control . . . . .</b>	<b>84</b>

---

5.3.1	Ziegler-Nichols Tuning and Root Locus Analysis . . . . .	84
5.3.2	Single Objective Optimization . . . . .	87
5.3.3	Multiobjective Optimization . . . . .	87
<b>5.4</b>	<b>Comparison of Optimization Strategies . . . . .</b>	<b>89</b>
<b>6</b>	<b>CONCLUSIONS . . . . .</b>	<b>92</b>

# 1 Introduction

This chapter presents the definition of the problem to be addressed, the guiding hypotheses of the study, the main goals of the study, the justification for its importance and implementation, and finally, the organization of this document in the subsequent chapters.

## 1.1 Problem definition

The advent of Synthetic Aperture Radars (Moreira *et al.*, 2013) in remote sensing has enabled the collection of large amounts of data with a wide range of applications. These range from seamless imaging of areas regardless of weather conditions and detecting millimetric vertical displacements (Ferretti; Prati; Rocca, 2000) to generating a high-precision Digital Elevation Model (DEM) of the entire world (Krieger *et al.*, 2007). Whilst SAR data post-processing and analysis offer limitless possibilities, some applications require specific satellite configurations to be feasible. A notable example is the TanDEM-X mission, which employs two satellites in close proximity, flying in a Helix formation as shown in Figure 1.1, to enable single-pass multi-satellite imaging (Krieger *et al.*, 2007).

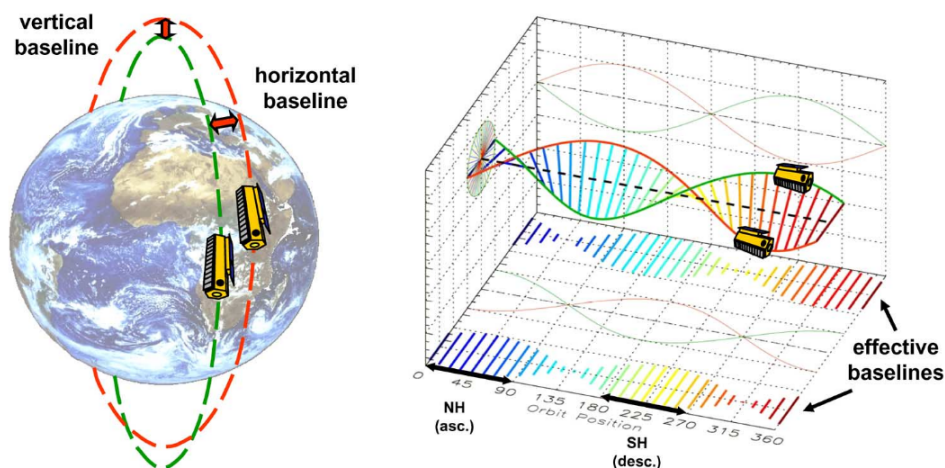


FIGURE 1.1 – HELIX satellite formation for TanDEM-X. (Left) Orbital arrangement. (Right) Cross-track baselines as function of the orbit position. The positions correspond to one complete orbit cycle, where NH and SH mean Northern and Southern Hemispheres, respectively (Krieger *et al.*, 2007).

This configuration requires the proper selection of nominal orbital elements to achieve the desired relative motion and separation between the satellites (D’Errico, 2012). Moreover, precise orbit control maneuvers are necessary to stabilize the formation, maintaining the designed close proximity while ensuring mission safety (Kahle *et al.*, 2012). However, future SAR mission concepts are considering the use of small satellites, which demand more efficient thruster systems with lower thrust magnitudes than those used in previous SAR missions (Mittermayer *et al.*, 2022; Nogueira Peixoto *et al.*, 2023). Hence, the viability of new techniques for such missions should be explored, particularly focusing on thrusters with lower thrust magnitudes and better cost-efficiency in terms of propellant usage.

Therefore, one application of this specific type of thruster would be the use of continuous linear control, specifically feedback control strategies that rely on measuring the current state and subsequent calculations of control gains to define the acceleration needed from the thruster to stabilize the system’s dynamics (Alfriend *et al.*, 2010). Unfortunately, determining these control gains or corresponding parameters requires a tuning step, which may vary depending on different geometries, separations, and initial state errors (Alfriend *et al.*, 2010; D’Errico, 2012). In this context, the literature on satellites formation flying typically addresses this analysis through manual tuning (Alfriend *et al.*, 2010; Vadali; Vaddi; Alfriend, 2002), lacking a systematic study of the corresponding search space using proper optimization-based methods, specifically looking into the trade-off between control usage and error minimization.

To handle the ill-posed optimization problem the application of metaheuristic optimization methods represent a promising solution. These techniques, such as the genetic algorithm (Kumar *et al.*, 2008), particle swarm optimization (Wang; Tan; Liu, 2017), ant colony (Chiha; Liouane; Borne, 2012; Thamir, 2020), and simulated annealing (Corana *et al.*, 1989), are well-suited to deal with complex and multiobjective optimization problems. These methods can find near-optimal solutions that minimize both control usage and state errors in a feasible time without relying on manual tuning, by searching the decision variable space efficiently. Furthermore, these optimization strategies provide flexibility for various mission configurations, geometries, and operational constraints, thus offering a robust framework for the tuning of control parameters in formation flying missions.

Once the system dynamics, real-time optimization, and control laws are established, the performance of various optimization algorithms and strategies is evaluated to address the inherently multiobjective nature of the problem. In this context, the decision variables consist of control gains or associated control weights corresponding to different modern control methodologies. The objective functions are designed to minimize both control usage and relative motion error, while ensuring the stability of the satellite formation. Accordingly, the central research question of this work is formulated as follows:

”What are the most effective multiobjective optimization strategies and algorithms — in terms of control efficiency and relative position error minimization — considering solution quality and robustness of the optimization process, when applied to the formation flying of two closely spaced satellites for synthetic aperture radar (SAR) applications?”

## 1.2 Hypotheses

The main hypotheses of this study relate to the effectiveness of formation flying dynamics modeling and heuristic optimization techniques in tuning the orbit control design, with the aim of achieving performance better than that obtained by manual tuning. Based on the formulation of the control problem and the objectives of this work, the following hypotheses are proposed:

- **Feasibility of Metaheuristic Optimization:** Metaheuristic optimization algorithms will be capable of finding viable control solutions that are at least as effective as those obtained through manual tuning.
- **Improved Gain Sensitivity Exploration:** Optimization algorithms will better explore the sensitivity of the control gain tuning process, leading to improved overall system performance, than manual tuning.
- **Geometry-Independent Optimization Performance:** For a given controller, the most effective optimization approach, including both strategy and algorithm, is expected to remain effective across different initial conditions, whether in formation maintenance or reconfiguration scenarios, and should not depend on a specific orbital configuration.
- **Advantage of Robust Search in Challenging Orbits:** For reference orbits where the controller exhibits convergence difficulties, optimization strategies that offer more robust exploration of the search space — such as multiobjective methods — will provide superior performance.

## 1.3 Objectives

The objective of this study is to investigate linear feedback control routines for a two-satellite cluster performing synthetic aperture radar interferometry. The focus is on the proper selection of controller gains, which can vary with different formation geometries. This research will explore the use of simple feedback control methods for approximating the dynamics and investigate the potential for an automatic control gain selector. The

proposed approach will be tested against existing literature to evaluate its performance in similar systems.

The specific objectives of this study can be broken down as follows:

- **Implement Formation Flying System Dynamics:** Develop a computationally efficient model of the formation flying system dynamics to facilitate the optimization process.
- **Investigate Optimization Algorithms and Strategies:** Explore various optimization algorithms and strategies to effectively tune the control parameters of formation flying systems, with a focus on multiobjective optimization.
- **Create a Guideline for Future Research:** Provide a simple and comprehensive guideline for future studies on the optimization of relative orbit control in formation flying systems, enabling easier adaptation and exploration of advanced techniques.

## 1.4 Motivation

The motivation for this study arises from the increasing number of new SAR mission concepts that rely on formation flying, requiring improved orbit design and more precise relative motion control. Additionally, the literature on tuning control parameters for formation flying systems, whether using classical or modern controllers, remains scarce.

The main SAR mission utilizing formation flying is the TanDEM-X (Krieger *et al.*, 2007) mission, which consists of two large, heavy satellites performing periodic orbital maneuvers using cold and hot gas propulsion. However, many emerging mission concepts focus on small satellites, which leverage electric and ion thrusters, enabling continuous control to maintain relative positioning. The key drivers of orbit control in these missions revolve around efficient thrust usage and maintaining accurate satellite dynamics, which can become unstable without proper consideration of orbital perturbations, navigation errors, and precise thrust application (Frey *et al.*, 2004; Kahle *et al.*, 2012).

In all these scenarios, controller parameter tuning is a crucial issue. Existing literature primarily discusses this tuning manually or heuristically (Alfriend *et al.*, 2010), without systematically exploring optimization-based approaches. Extensive research has been conducted on optimization-based control tuning in various dynamic systems (Bansal; Sharma; Ponpathirkootam, 2012), demonstrating the effectiveness of optimization techniques in improving control performance. Studies have proposed improved control approaches for formation flying systems from an analytical perspective of controller modeling but have not thoroughly explored parameter tuning optimization (Vadali; Vaddi; Alfriend, 2002).

This gap highlights both an academic and practical need to study the performance of different optimization methods, particularly those with fast convergence for the formation flying problem. Such optimization techniques could facilitate research by comparing control methods, refining ground segment operation routines, and even advancing the design of adaptive control strategies.

## 1.5 Work Organization

Chapter 1 presents the introduction of this study, outlining the main problem addressed in this work. Moreover, this chapter introduces the hypotheses considered, the objectives structured to be achieved in this research, and the rationale behind its significance and necessity.

Chapter 2 provides a review of the existing literature relevant to this study. It introduces the main concepts of Synthetic Aperture Radar and the applications of formation flying in this field. Following this, the chapter provides a more in-depth examination of formation flying control research and the optimization strategies that have already been explored.

Chapter 3 presents the theoretical foundation considered for this study, covering the main concepts of SAR, orbital mechanics, formation flying, control theory, and meta-heuristic optimization.

Chapter 4 outlines the methodology employed in this study, detailing the software tools, simulation framework, and statistical analysis used to evaluate the optimization strategies. Furthermore, Chapter 5 presents the preliminary numerical results obtained from simulations and statistical analysis, considering both single- and multiobjective optimizations.

Hence, Chapter 6 summarizes the main findings of this study, highlights its key contributions, and suggests potential directions for future research.

## 2 Literature Review

This chapter presents a literature review on the topics relevant to this study. The first section discusses the concept of satellites formation flying and their applications in Earth observation. The second section reviews the control strategies used in formation flying, with a focus on formation maintenance. The third section examines optimization techniques applied to control systems and, more specifically, to formation flying, highlighting their advantages and limitations. In this way, this chapter aims to provide the historical and technical context for the work developed in this study.

### 2.1 Formation Flying for Synthetic Aperture Radar

The concept of formation flying has been widely employed over the last few decades for Earth observation missions (Alfriend *et al.*, 2010). The use of multiple satellites flying in formation enables a new class of missions that rely on the proximity and active maintenance of satellite configurations to achieve a common objective. A notable example is the GRACE mission (**G**ravity **R**ecovery **A**nd **C**limate **E**xperiment), which utilized two satellites flying in the same orbit, approximately 220 km apart, to measure Earth's gravity field (D'Errico, 2012). This mission required a high level of precision in maintaining the satellite configuration and balancing fuel consumption. As a result, formation maneuvers alternated between GRACE-1 and GRACE-2, depending on which satellite assumed control at a given time.

In the realm of Synthetic Aperture Radar (SAR), active sensors provide significantly more information about the observed scene compared to traditional optical satellites. The fundamental concept of SAR interferometry is to compare, for a given scene, complex radar images acquired from slightly different positions or at different times (Ferretti; Prati; Rocca, 2000). Since the phase of each SAR image pixel contains highly accurate range information, on the order of a fraction of the radar wavelength, it is possible to detect path length differences with centimetric or even millimetric scale (Moreira *et al.*, 2013). A prominent example is the TanDEM-X mission, which employed two satellites flying in close formation to generate a digital elevation model of Earth with unprecedented

resolution (Moreira *et al.*, 2013). Launched in 2010, the TanDEM-X mission remains active, providing high-resolution topographic data for a wide range of applications, including land use planning, disaster management, and environmental monitoring (Krieger *et al.*, 2007).

Current SAR mission concepts are being developed with a focus on smaller satellites, reduced costs, and lower-thrust but more efficient propulsion systems. This shift demands a different approach to formation flying design. The exploitation of CubeSats as add-ons in the TanDEM-X mission (Nogueira Peixoto *et al.*, 2023) for interferometry introduces the possibility of operating at closer proximities with smaller satellites. However, this also requires more precise and secure control strategies for formation maintenance. Similarly, the MirrorSAR mission employs a design involving three satellites trailing the main satellite, Sentinel-1. This configuration eliminates the need for larger satellites, as the smaller deputy satellites are used exclusively as receivers (RX), thereby reducing the complexity of their onboard systems (Mittermayer *et al.*, 2022).

## 2.2 Formation Flying Control

The definition of spacecraft formation flying control, as proposed by NASA's Goddard Space Flight Center (GSFC), encompasses the requirements for two or more spacecraft to perform active and cooperative control to track or maintain a desired relative separation, orientation, or position between or among them (Alfriend *et al.*, 2010). By design, satellites in formation typically share a common nominal orbit with similar orbital elements, often implying close proximity and long-duration missions that demand safe, collision-free operation. These requirements have inspired a range of approaches in the literature, including the application of both classical and modern continuous control theories to stabilize and mitigate the differential effects caused by Earth's oblateness and atmospheric drag (Alfriend *et al.*, 2010).

In the case of larger satellites, such as those used in the TanDEM-X mission, impulsive control has been the preferred method for formation maintenance (Krieger *et al.*, 2007). This approach relies on the assumption that the spacecraft can be maneuvered using a series of instantaneous velocity changes, typically modeled as delta-v impulses. However, mission control must still perform periodic maneuvers on a daily or weekly basis. These maneuvers can be costly in terms of fuel consumption and operational complexity, and they remain susceptible to high levels of error and uncertainty in the control state (Kahle *et al.*, 2012).

## 2.3 Control Cost Optimization

Historically, metaheuristic optimization techniques have gained increasing attention in control systems due to their flexibility in formulating complex optimization problems (Bansal; Sharma; Ponpathirkoottam, 2012). Methods such as the genetic algorithm (Holland, 1975) have been widely applied for tuning Proportional-Integral-Derivative (PID) controllers (Kumar *et al.*, 2008). Their capability to address nonlinear, non-convex, and multiobjective problems has allowed metaheuristic approaches to achieve significant results across a variety of cost function and constraint combinations.

However, most existing applications of metaheuristic optimization techniques have been centered around different systems and control applications. Examples include the single objective PID tuning of a model bioreactor (Kumar *et al.*, 2008), multiobjective PID controller optimization using ant colony optimization (Chiha; Liouane; Borne, 2012), and its variations involving fuzzy logic integration (Tang *et al.*, 2001). Additionally, similar approaches have been extended to other linear control strategies, such as the Linear Quadratic Regulator (LQR) (Thamir, 2020).

The diversity of metaheuristic optimization techniques, each inspired by different natural or conceptual phenomena such as animal behavior (Wang; Tan; Liu, 2017), human processes (Holland, 1975), evolutionary mechanisms (Storn; Price, 1997), and physical principles (Corana *et al.*, 1989), makes the selection of an appropriate technique a challenging task. The performance of these algorithms is highly dependent on the specific characteristics of the problem being addressed, and the literature presents a wide variety of outcomes across different applications. One effective approach to compare their performance is through the experimental evaluation of these heuristic algorithms applied directly to the problem at hand (Rardin; Uzsoy, 2001), such as the formation flying control of satellites. This strategy has been employed in studies comparing local search evolutionary algorithms (Auger; Hansen, 2005) and in broader benchmarking initiatives for black-box optimization problems (Hansen *et al.*, 2010).

In summary, this work presents a comprehensive study on optimization-based control tuning applied to satellite formation flying for SAR missions. It systematically investigates optimization algorithms of different natures and inspirations within both single and multiobjective frameworks, aiming to improve controller performance and robustness. By combining classical and modern control approaches, such as PID and LQR, with advanced optimization strategies, this research establishes a framework for analyzing and enhancing control efficiency in a coupled and originally nonlinear system. The insights derived from this study provide a solid foundation for the development of adaptive control strategies applicable to future small-satellite formation missions.

## 3 Theoretical Foundation

This section presents the fundamental concepts and mathematical framework applied to this research. It is divided into five parts as follows: the first consolidates the basis of SAR to situate the work within its space mission context, the second and third develop the theory governing the system dynamics, the fourth details the theory applied to control these dynamics, and the fifth provides the relevant optimization methods, their definitions and interpretations.

### 3.1 Synthetic Aperture Radar

Synthetic Aperture Radar (SAR) is an active microwave remote sensing technology capable of producing high-resolution, two-dimensional images of the Earth’s surface (Moreira *et al.*, 2013). As an active sensor, SAR provides its own illumination by transmitting electromagnetic pulses and then recording the echoes backscattered from the scene (Moreira *et al.*, 2013). This fundamental characteristic grants SAR a significant operational advantage over passive optical systems: the ability to acquire data regardless of daylight, cloud coverage, or adverse weather conditions, enabling reliable and continuous monitoring of dynamic processes on a global scale (Moreira *et al.*, 2013).

The system is typically mounted on a moving platform, such as a satellite, and operates with a side-looking imaging geometry, as depicted in Figure 3.1. The direction of the platform’s motion at velocity  $v$  is known as azimuth, while the line-of-sight direction perpendicular to the flight path is the slant range (Moreira *et al.*, 2013). The radar illuminates a strip of the Earth’s surface, referred to as the swath, located to the side of its ground path (the nadir track). The “Synthetic Aperture” concept arises from this geometry: as the platform moves, its antenna illuminates a target for a duration determined by the azimuth beamwidth ( $\Theta_a$ ). The path length traveled during this illumination time constitutes the synthetic aperture (Moreira *et al.*, 2013). By coherently combining the radar echoes collected along this path, the system effectively synthesizes a much longer virtual antenna than its physical one. This process yields a high spatial resolution in the azimuth direction that is remarkably independent of the sensor’s altitude (Moreira

*et al.*, 2013). Resolution in the cross-track direction (slant range) is achieved by transmitting wide-bandwidth pulses, commonly frequency-modulated *chirps*, and is inversely proportional to the signal bandwidth (Moreira *et al.*, 2013).

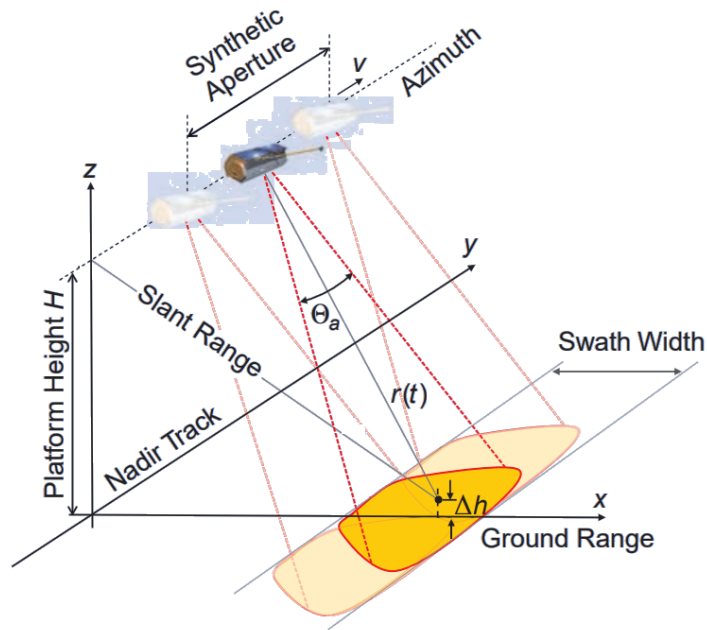


FIGURE 3.1 – Illustration of the SAR imaging geometry.  $r(t)$  stands for the shortest approach distance,  $\Theta_a$  for the azimuth beamwidth and  $v$  for the sensor velocity (Moreira *et al.*, 2013).

The final product is a complex-valued image, where each pixel contains both the amplitude and phase of the backscattered signal, representing a measure of the scene's radar reflectivity (Moreira *et al.*, 2013).

### 3.1.1 Interferometry

Interferometric SAR (InSAR) is a powerful remote sensing technique that leverages the phase information contained within SAR imagery to make precise measurements of the Earth's surface (Moreira *et al.*, 2013). The fundamental principle of InSAR is the comparison of the phase from two or more complex SAR images acquired over the same area but from slightly different viewing positions (Moreira *et al.*, 2013). Since the phase of each pixel is directly related to the round-trip distance between the sensor and the target with an accuracy on the order of the radar wavelength, the phase difference between two images, the interferogram, reveals minute path length differences with centimetric or even millimetric precision (Moreira *et al.*, 2013).

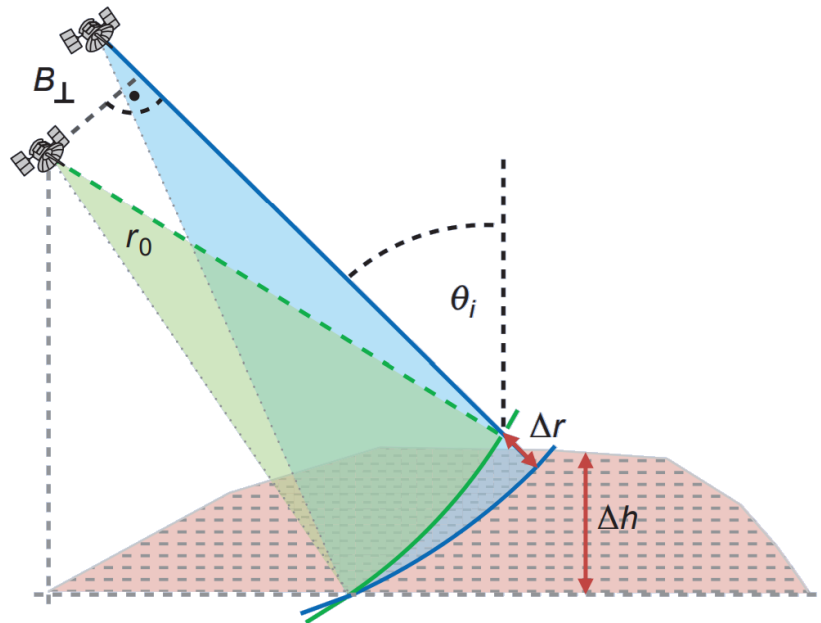


FIGURE 3.2 – Across-track SAR interferometry employs antennas that move on parallel but mutually displaced flight paths (the flight paths are not shown since they are pointing into the page). The slant range  $r_0$ , the incident angle  $\theta_i$  and the effective baseline  $B_{\perp}$  are all defined in a plane perpendicular to the flight paths. A change in the surface height by  $\Delta h$  causes a change in the range difference by  $\Delta r$  (Moreira *et al.*, 2013).

This high sensitivity to path length differences enables the accurate measurement of surface topography through a technique known as across-track interferometry, illustrated in Figure 3.2. The technique requires acquiring two images from antennas separated by a known perpendicular distance, or “baseline” ( $B_{\perp}$ ). As shown in the figure, this spatial separation causes a change in surface height ( $\Delta h$ ) to manifest as a measurable change in the range difference ( $\Delta r$ ) between the two acquisitions. This range difference is precisely what is captured by the interferometric phase, which can then be related to terrain elevation, allowing for the generation of high-resolution Digital Elevation Models (DEMs) (Moreira *et al.*, 2013).

These acquisitions can be performed in a “repeat-pass” configuration, where a single satellite revisits an area, or a “single-pass” configuration. Repeat-pass interferometry is susceptible to temporal decorrelation, where changes in the scene or atmospheric conditions between acquisitions introduce phase errors (Moreira *et al.*, 2013). To overcome these limitations and achieve the highest accuracy, single-pass interferometry is employed. This method utilizes two satellites flying in a close, precisely controlled formation to acquire both images simultaneously (Moreira *et al.*, 2013). This configuration effectively eliminates errors from temporal decorrelation and atmospheric disturbances, making it the preferred approach for high-fidelity global topographic mapping missions, such as the TanDEM-X mission (Krieger *et al.*, 2007). Therefore, the stringent requirements of single-pass SAR interferometry are a primary driver for the development and operation

of satellite formation flying missions.

### 3.1.2 TanDEM-X Mission

The TanDEM-X (TerraSAR-X add-on for Digital Elevation Measurement) mission represents a pioneering implementation of a bistatic Synthetic Aperture Radar (SAR) system designed to generate a global, high-precision Digital Elevation Model (DEM) (Krieger *et al.*, 2007). The mission's success relies on two nearly identical satellites, TerraSAR-X and TanDEM-X, operating as a large single-pass radar interferometer. Central to this concept is the innovative helix flight formation, which allows for precise and flexible adjustment of the interferometric baseline: a critical parameter for optimizing DEM accuracy across varied topographies (Krieger *et al.*, 2007).

This orbital configuration was fundamental to the mission scenario, which enabled the acquisition of a global DEM in under three years (Krieger *et al.*, 2007). The strategy involved multiple data takes with different baselines, varying incident angles, and observations from both ascending and descending orbits to effectively map challenging terrains such as mountains and valleys (Krieger *et al.*, 2007). In its standard bistatic mode, one satellite transmits radar pulses while both simultaneously receive the backscattered echoes (Krieger *et al.*, 2007). This **across-track interferometry** technique allows for the direct measurement of topographic height by analyzing the phase difference between the signals, thereby overcoming the limitations of repeat-pass interferometry, such as temporal decorrelation, and ensuring a consistent, highly accurate global DEM (Krieger *et al.*, 2007; D'Errico, 2012) with unprecedented accuracy and resolution (12 m horizontal and 2 m vertical resolution) (D'Errico, 2012).

## 3.2 Orbital Mechanics

Orbital mechanics is a key area of study for understanding and predicting how objects like satellites move in space under the force of gravity (Curtis, 2014). Modern space systems, such as satellite constellations and spacecraft formation flying, depend on orbital mechanics to keep their exact positions and alignments with each other (Alfriend *et al.*, 2010). This allows them to work together as one coordinated system. This subsection will review the basic principles of motion needed to analyze both simple two-body orbits and the more complex relative movements involved in formation flying, including orbital disturbances.

### 3.2.1 Coordinates Systems

The study of a system's kinematics and dynamics requires the definition of a well-structured reference frame upon which the analysis is based. From this reference frame, coordinate systems are established to effectively formulate the equations describing the forces and motions acting on the system. While the study of orbital mechanics is generally centered on an inertial reference frame, non-inertial reference frames are also employed to better describe specific physical quantities of interest (Alfriend *et al.*, 2010).

The Earth-Centered Inertial (ECI) coordinate system is a non-rotating reference frame centered at the Earth's center of mass. It is commonly used to describe the position and motion of satellites relative to Earth and is particularly suitable for analyzing geodesic effects in Earth's gravitational field (Curtis, 2014). The ECI frame is defined such that the unit vector  $\hat{x}$  points from Earth's center toward the vernal equinox,  $\hat{z}$  is aligned with the Earth's rotation axis, positive toward the geographic North Pole, and  $\hat{y}$  completes the right-handed Cartesian system, as illustrated in Figure 3.3.

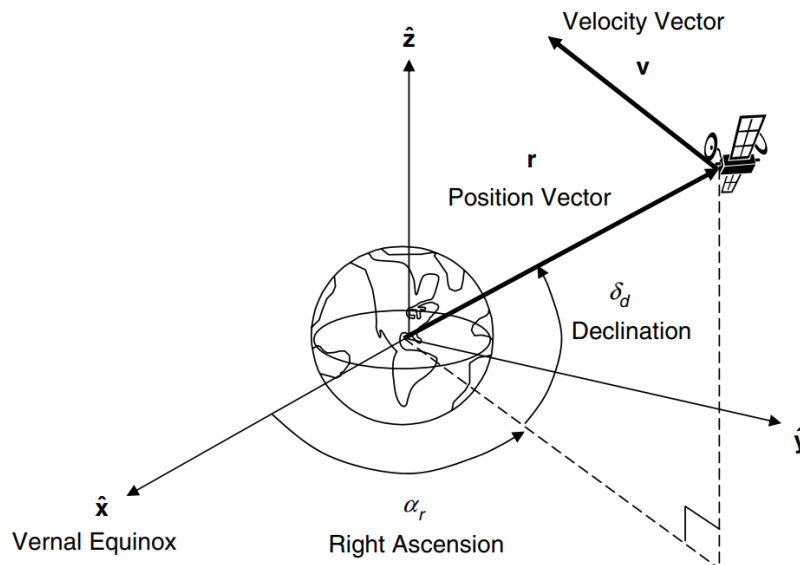


FIGURE 3.3 – The Earth-centered inertial (ECI) coordinate system. Also shown are  $r$  and  $v$ , the position and velocity vectors, respectively, as well as the right ascension,  $\alpha_r$ , and the declination,  $\delta_d$  (Alfriend *et al.*, 2010).

The Local-Vertical Local-Horizontal (LVLH) coordinate system is a rotating reference frame centered at a satellite's center of mass. The LVLH frame is defined such that the unit vector  $\hat{x}$  points radially outward from the Earth toward the satellite,  $\hat{z}$  is normal to the fundamental plane, and  $\hat{y}$  completes the right-handed Cartesian system, aligned with the direction of orbital motion (Alfriend *et al.*, 2010), as illustrated in Figure 3.4.

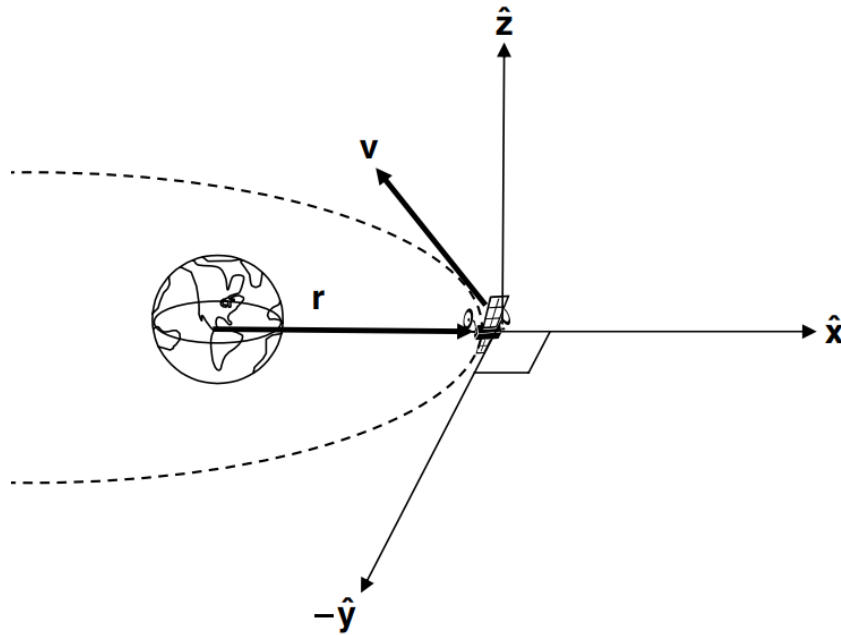


FIGURE 3.4 – Local-vertical, local-horizon rotating coordinate system, centered at the spacecraft (Alfriend *et al.*, 2010).

### 3.2.2 Equations of Motion

The two-body problem analyzes two punctual masses with spherical symmetry,  $m_1$  and  $m_2$ , moving exclusively under their mutual gravitational force (Curtis, 2014). Their motion is described relative to an inertial reference frame, as shown in Figure 3.5.

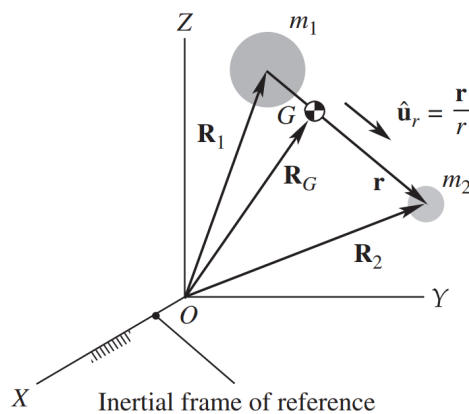


FIGURE 3.5 – Relative motion of two bodies in an inertial reference frame (Curtis, 2014).

The position of mass  $m_2$  with respect to  $m_1$  is defined by the relative position vector  $\mathbf{r}$  in Equation 3.1.

$$\mathbf{r} = \mathbf{R}_2 - \mathbf{R}_1 \quad (3.1)$$

Differentiating Equation 3.1 twice with respect to time yields the relative acceleration

vector,  $\ddot{\mathbf{r}}$ , shown in Equation 3.2.

$$\ddot{\mathbf{r}} = \ddot{\mathbf{R}}_2 - \ddot{\mathbf{R}}_1 \quad (3.2)$$

By applying Newton's laws of motion and universal gravitation (Curtis, 2014), the accelerations  $\ddot{\mathbf{R}}_1$  and  $\ddot{\mathbf{R}}_2$  can be substituted into Equation 3.2. This yields the fundamental equation of motion for the two-body problem, presented as Equation 3.3.

$$\ddot{\mathbf{r}} = -\frac{G(m_1 + m_2)}{r^2} \hat{\mathbf{u}}_r \quad (3.3)$$

To simplify, the standard gravitational parameter,  $\mu$ , is introduced, as defined in Equation 3.4. For most spacecraft applications, the mass of the spacecraft is negligible compared to the central body ( $m_2 \ll m_1$ ), so  $\mu \approx Gm_1$ .

$$\mu = G(m_1 + m_2) \quad (3.4)$$

By substituting the definition of  $\mu$  from Equation 3.4 and the unit vector  $\hat{\mathbf{u}}_r = \mathbf{r}/r$  into Equation 3.3, the equation of motion is expressed in its final, compact form in Equation 3.5.

$$\ddot{\mathbf{r}} = -\frac{\mu}{r^3} \mathbf{r} \quad (3.5)$$

Equation 3.5 is a second-order nonlinear differential equation whose solution is a conic section (Curtis, 2014). For an Earth observation satellite mission, this trajectory must be a closed path, which is characteristically an ellipse (Curtis, 2014; D'Errico, 2012).

### 3.2.3 Orbital Elements

The motion of a satellite in a two-body system is uniquely defined by six parameters known as the classical orbital elements, which are illustrated in Figure 3.6. These elements provide an intuitive description of the orbit's size, shape, and orientation in three-dimensional space, as well as the satellite's position within it, which is equivalent to the time variable in the original Equation 3.5.

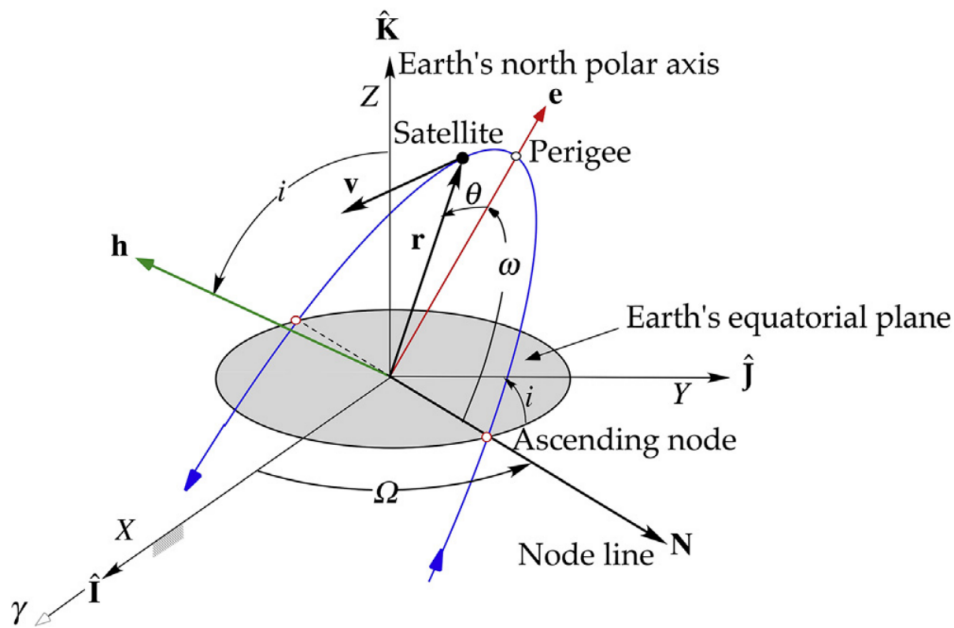


FIGURE 3.6 – Geocentric equatorial frame and the orbital elements (Curtis, 2014).

The classical orbital elements are defined as follows (Alfriend *et al.*, 2010; Curtis, 2014):

- **Semimajor Axis ( $a$ ):** This element defines the size of the orbit and is directly proportional to its energy. For an elliptical orbit, it represents half of the longest diameter of the ellipse. A larger semimajor axis corresponds to a longer orbital period.
- **Eccentricity ( $e$ ):** This dimensionless parameter describes the shape of the orbit by measuring its deviation from a perfect circle. A value of  $e = 0$  indicates a circular orbit, while  $0 < e < 1$  defines an ellipse.
- **Inclination ( $i$ ):** This angle specifies the inclination of the orbital plane relative to the Earth's equatorial plane. An inclination of  $0^\circ$  corresponds to an equatorial orbit,  $90^\circ$  to a polar orbit, and values between  $90^\circ$  and  $180^\circ$  represent retrograde orbits, which move against the direction of Earth's rotation.
- **Right Ascension of the Ascending Node ( $\Omega$ ):** This element orients the orbital plane in three-dimensional space. It is the angle measured eastward in the equatorial plane from a fixed inertial direction (the vernal equinox,  $\gamma$ ) to the point where the satellite crosses the equator from south to north.
- **Argument of Perigee ( $\omega$ ):** This angle defines the orientation of the ellipse within its orbital plane. It is measured in the direction of the satellite's motion from the ascending node to the orbit's point of closest approach to Earth, known as the perigee.

- **True Anomaly ( $f$ ):** This is the only element that changes with time in an unperturbed two-body orbit. It specifies the satellite's exact position along its path at a given instant. The true anomaly is the angle measured from the perigee to the satellite's current position vector.

Whilst the classical orbital elements provide a geometrically intuitive framework for orbit design, they present mathematical singularities in specific cases that are common in operational missions. For instance, in near-circular orbits, such as that of TanDEM-X (Krieger *et al.*, 2007), the perigee is not well-defined, causing the argument of perigee ( $\omega$ ) and true anomaly ( $f$ ) to become indeterminate.

To handle these limitations in orbit propagation and analysis, designers often employ **quasi-non-singular** or **non-singular orbital elements** (D'Errico, 2012). For missions requiring high precision in orbits that are both near-circular and near-equatorial, such as those in geostationary rings or low-Earth orbit constellations, a fully **non-singular** set like the **equinoctial elements** is used instead (D'Errico, 2012). Though less geometrically intuitive, these elements are mathematically robust, avoiding singularities and providing more stability and reliability for numerical integration and **long-term** perturbation analysis.

### 3.2.4 Orbital Perturbations

A satellite's motion, in reality, is not governed solely by the gravitational pull of a perfectly spherical central body. Any effect that causes the trajectory to deviate from the ideal two-body Keplerian orbit is known as a perturbation (Curtis, 2014). These effects are modeled by adding a perturbing acceleration vector,  $\mathbf{p}$ , to the two-body equation of motion as shown in Equation 3.6:

$$\ddot{\mathbf{r}} = -\frac{\mu}{r^3}\mathbf{r} + \mathbf{p} \quad (3.6)$$

The vector  $\mathbf{p}$  is the sum of all non-Keplerian accelerations acting on the satellite. The relative magnitudes of the most significant perturbations for an Earth-orbiting satellite are illustrated in Figure 3.7.

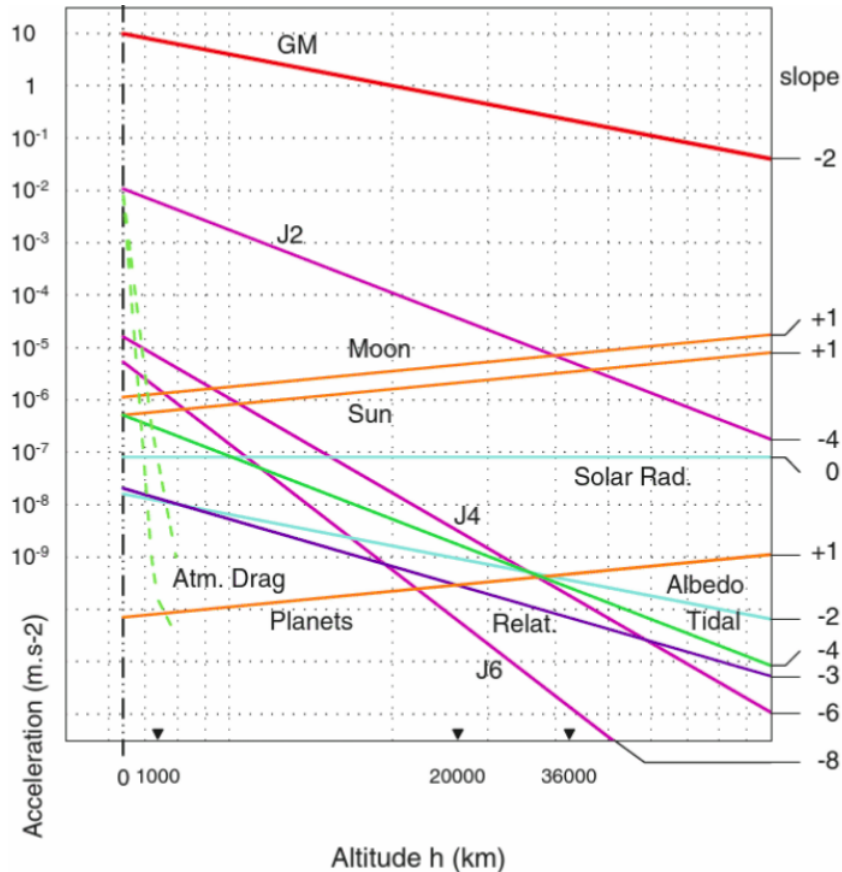


FIGURE 3.7 – Central acceleration and perturbative accelerations as a function of the distance  $r$  of the satellite from the center of the Earth, shown on a log-log scale (Capderou, 2014).

The primary perturbations handled in this context are:

- **Gravitational Perturbations:** The Earth is not a perfect sphere. This non-uniform mass distribution creates a gravitational potential that varies with latitude. This effect is modeled using a series of spherical harmonics, where the dominant term is the second zonal harmonic,  $J_2$  (Curtis, 2014). The  $J_2$  perturbation does not cause long-term changes to the orbit's size or shape but produces significant secular (long-term) drifts in the right ascension of the ascending node ( $\Omega$ ) and the argument of perigee ( $\omega$ ) (Alfriend *et al.*, 2010).
- **Atmospheric Drag:** For satellites in Low Earth Orbit (LEO), the most significant perturbation is atmospheric drag. This force arises from the friction between the satellite and particles in the upper atmosphere, acting opposite to the satellite's velocity vector relative to the atmosphere. It causes a loss of orbital energy, which leads to a decrease in the semimajor axis causing the orbit to decay (Curtis, 2014).
- **Third-Body Perturbations:** The gravitational forces from other celestial bodies, primarily the Sun and the Moon, also perturb a satellite's orbit around the Earth.

The magnitude of these third-body effects increases with the satellite's altitude (Curtis, 2014).

- **Solar Radiation Pressure:** This perturbation arises from the momentum flux of solar photons impacting the satellite surface, resulting in a small force directed away from the Sun. Although the force exerted is relatively small, it can accumulate over time, leading to significant changes in the orbit, particularly for satellites with large, lightweight structures, causing long-term periodic and secular variations in the orbital elements (Curtis, 2014).

### 3.2.5 Sun-Synchronous Orbit

The secular drift in the right ascension of the ascending node ( $\dot{\Omega}$ ), caused by the Earth's oblateness is a predictable effect that can be strategically exploited in orbit design. A Sun-Synchronous Orbit (SSO) is a prime example of this, where the orbit is designed to precess eastward at the same rate as the Earth's mean orbital motion around the Sun, approximately  $0.9856^\circ$  per day (Curtis, 2014). To achieve this, the secular nodal precession rate,  $\dot{\Omega}$ , is set equal to the Earth's mean motion. For a given semimajor axis and eccentricity, this condition determines the required orbital inclination, which is typically retrograde for satellites in Low Earth Orbit (LEO) (Curtis, 2014). Evaluation of the required SSO inclination for circular orbits is shown in Figure 3.8.

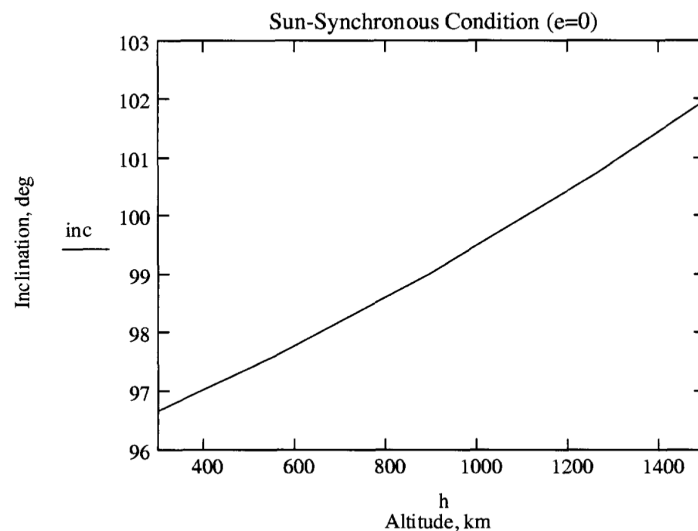


FIGURE 3.8 – Sun-synchronous Condition: Inclination vs. Altitude ( $e = 0$ ) (Boain, 2005).

An SSO offers two significant advantages for Earth observation missions. Firstly, the satellite's orbital plane maintains a nearly constant orientation relative to the Sun-Earth line throughout the year. This provides consistent and predictable illumination conditions for the satellite, which is fundamental for designing the power subsystems, especially for

satellites with high power requirements, such as those equipped with a radar antenna. Secondly, a satellite in an SSO passes over any given point on the Earth’s surface at the same local solar time on each pass. This consistency in lighting and atmospheric conditions simplifies the process of detecting changes over time and reduces issues caused by temporal and atmospheric decorrelation, thereby easing post-processing.

### 3.3 Formation Flying

Spacecraft formation flying involves the tracking and maintenance of a desired relative separation, orientation, or position among multiple spacecraft (Alfriend *et al.*, 2010). By functioning as a cohesive, distributed unit, these formations can achieve complex mission objectives that are often beyond the capacity of a single, monolithic satellite (D’Errico, 2012).

#### 3.3.1 Relative Dynamics

The analysis of relative motion between two satellites orbiting a central body, such as the Earth, designates one spacecraft as the *chief* and the other as the *deputy*. The derivation begins by defining the absolute motion of each satellite in an Earth-Centered Inertial (ECI) frame using the Keplerian two-body equation. Subsequently, to determine the relative dynamics, the state vector of the *deputy* is transformed into the *chief*’s moving Local-Vertical/Local-Horizontal (LVLH) frame. This transformation allows for the direct analysis of the *deputy*’s position and velocity relative to the *chief*, as illustrated in Figure 3.9.

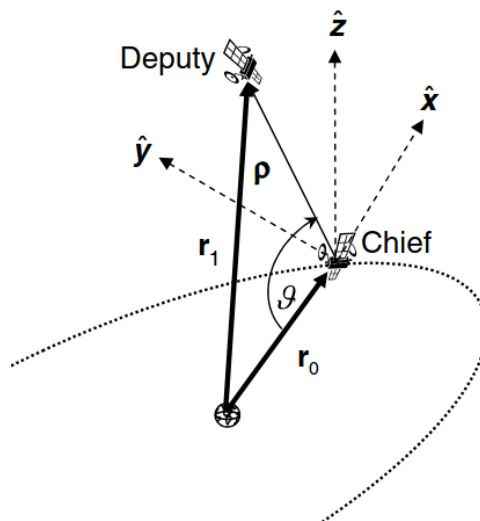


FIGURE 3.9 – Rotating Euler–Hill frame, centered at the chief spacecraft (Alfriend *et al.*, 2010).

Applying the two-body equation of motion (Equation 3.5) to the chief satellite yields its inertial equation of motion, shown in Equation 3.7:

$$\ddot{\mathbf{r}}_0 = -\frac{\mu}{r_0^3}\mathbf{r}_0 \quad (3.7)$$

where  $r_0$  is the magnitude of the chief's position vector,  $\mathbf{r}_0$ , given by the orbit equation in Equation 3.8.

$$r_0 = \|\mathbf{r}_0\| = \frac{a_0(1 - e_0^2)}{1 + e_0 \cos f_0} \quad (3.8)$$

Analogously, the deputy satellite's inertial equation of motion is given by Equation 3.9:

$$\ddot{\mathbf{r}}_1 = -\frac{\mu}{r_1^3}\mathbf{r}_1 \quad (3.9)$$

The position of the deputy relative to the chief is denoted by the vector  $\boldsymbol{\rho}$ , as defined in Equation 3.10:

$$\boldsymbol{\rho} = \mathbf{r}_1 - \mathbf{r}_0 \quad (3.10)$$

Furthermore, the acceleration of the deputy relative to the chief,  $\ddot{\boldsymbol{\rho}}$ , is the difference between their inertial accelerations. Substituting Equations 3.7 and 3.9 results in the exact nonlinear equation for the relative dynamics, shown in Equation 3.11:

$$\ddot{\boldsymbol{\rho}} = -\frac{\mu(\mathbf{r}_0 + \boldsymbol{\rho})}{\|\mathbf{r}_0 + \boldsymbol{\rho}\|^3} + \frac{\mu}{r_0^3}\mathbf{r}_0 \quad (3.11)$$

The equations for relative motion in the non-inertial LVLH frame are derived by applying a reference frame transformation. This transformation accounts for the rotation of the chief's LVLH frame, which has an angular velocity of  $\boldsymbol{\omega} = \dot{\theta}_0 \hat{\mathbf{z}}$ . The components of the relative position vector  $\boldsymbol{\rho}$  in this frame are defined as  $x$ ,  $y$ , and  $z$ , corresponding to the radial, in-track, and cross-track directions, as shown in Figure 3.9. The resulting equations of motion are given by Equations 3.12, 3.13, and 3.14:

$$\ddot{x} - 2\dot{\theta}_0\dot{y} - \ddot{\theta}_0 y - \dot{\theta}_0^2 x = -\frac{\mu(r_0 + x)}{[(r_0 + x)^2 + y^2 + z^2]^{3/2}} + \frac{\mu}{r_0^2} \quad (3.12)$$

$$\ddot{y} + 2\dot{\theta}_0\dot{x} + \ddot{\theta}_0 x - \dot{\theta}_0^2 y = -\frac{\mu y}{[(r_0 + x)^2 + y^2 + z^2]^{3/2}} \quad (3.13)$$

$$\ddot{z} = -\frac{\mu z}{[(r_0 + x)^2 + y^2 + z^2]^{3/2}} \quad (3.14)$$

These are supplemented by Equations 3.15 and 3.16 to fully describe the chief's motion:

$$\ddot{r}_0 = r_0 \dot{\theta}_0^2 - \frac{\mu}{r_0^2} \quad (3.15)$$

$$\ddot{\theta}_0 = -\frac{2\dot{r}_0 \dot{\theta}_0}{r_0} \quad (3.16)$$

### 3.3.2 Linear Equations of Relative Motion

When two satellites have very similar orbits, with only small differences in shape (eccentricity) and orientation (inclination and ascending node), their motion relative to each other remains small. For these cases of close-proximity flight, the complex nonlinear equations of relative motion can be simplified into a linear version. These linearized equations are known as the Clohessy-Wiltshire (CW) equations (Clohessy; Wiltshire, 1960), which provide a direct, solvable model for the deputy's motion relative to the chief.

The CW equations are derived by performing a Taylor's expansion of the full nonlinear dynamics (Equations 3.12, 3.13, and 3.14) around the origin of the chief's LVLH frame. This process results in the set of linear differential equations shown in Equations 3.17, 3.18, and 3.19 (Alfriend *et al.*, 2010).

$$\ddot{x} - 2n_0 \dot{y} - 3n_0^2 x = 0 \quad (3.17)$$

$$\ddot{y} + 2n_0 \dot{x} = 0 \quad (3.18)$$

$$\ddot{z} + n_0^2 z = 0 \quad (3.19)$$

where  $n_0$  is the mean motion of the chief satellite, defined in Equation 3.20:

$$n_0 = \sqrt{\frac{\mu}{a_0^3}} \quad (3.20)$$

### 3.3.3 Helix Formation

Hence, the relative motion of a deputy satellite with respect to a chief in a nearby circular orbit can be described by the CW Equations (3.17) - (3.19). These linear equations

with constant coefficients can be solved analytically to determine the deputy's position over time based on its initial relative position and velocity. The general solution to the CW equations is given by Equation 3.21 in terms of the initial conditions at time ( $t = 0$ ) (D'Errico, 2012).

$$\begin{cases} x(t) = \frac{\dot{x}(0)}{n_0} \sin(n_0 t) - \left( 3x(0) + \frac{2\dot{y}(0)}{n_0} \right) \cos(n_0 t) + 4x(0) + \frac{2\dot{y}(0)}{n_0} \\ y(t) = \frac{2\dot{x}(0)}{n_0} \cos(n_0 t) + \left( 6x(0) + \frac{4\dot{y}(0)}{n_0} \right) \sin(n_0 t) - (6n_0 x(0) + 3\dot{y}(0))t - \frac{2\dot{x}(0)}{n_0} + y(0) \\ z(t) = \frac{\dot{z}(0)}{n_0} \sin(n_0 t) + z(0) \cos(n_0 t) \end{cases} \quad (3.21)$$

From this analytical solution, the fundamental characteristics of the relative motion emerge. The radial ( $x$ ) and along-track ( $y$ ) components are coupled, tracing a 2 : 1 elliptical projection in the orbital plane ( $xy$ ). In contrast, the cross-track ( $z$ ) motion is an independent simple harmonic oscillation. The phase shift between the in-plane and out-of-plane motions can be adjusted by the initial conditions to produce a variety of three-dimensional trajectories. A critical characteristic of this solution is the secular drift term in the  $y$ -component, which, unless nullified, causes a linear growth in the along-track separation over time (D'Errico, 2012).

To achieve a stable relative trajectory, this secular drift must be eliminated. The CW framework establishes a stability condition by selecting initial velocity components that cancel the drift term, as shown in Equation 3.22 (D'Errico, 2012).

$$\dot{y} = -2n_0 x \quad (3.22)$$

It is important, however, to acknowledge the limitations of this analysis. The CW equations are derived under simplifying assumptions, and more complex models, such as the Tschauner-Hempel equations (Alfriend *et al.*, 2010), yield different stability conditions for eccentric orbits (Alfriend *et al.*, 2010). Nonetheless, for most practical applications involving close-proximity formation flying in Low Earth Orbit (LEO), the CW model provides a sufficiently accurate representation of the relative dynamics (Kahle *et al.*, 2012).

Furthermore the CW solution can also be expressed in terms of relative orbital elements (ROEs), which describe the differences in the classical orbital elements between the deputy and chief satellites. This formulation, presented in Equation 3.23, provides a more intuitive link between orbital design and the resulting formation geometry (D'Errico,

2012).

$$\begin{cases} x(t) \approx \delta a - a\delta e \cos(f) \\ y(t) \approx 2a\delta e \sin(f) + a(\delta\omega + \delta M_0 + \delta\Omega \cos i) - \frac{3a}{2}(f - f(0))\delta a \\ z(t) \approx a\sqrt{\delta i^2 + \sin^2 i \delta\Omega^2} \cos(\omega + f - \phi) \end{cases} \quad (3.23)$$

where the auxiliary angle  $\phi$  is defined in Equation 3.24:

$$\phi = \tan^{-1} \left( \frac{\delta i}{-\sin i \delta\Omega} \right) \quad (3.24)$$

Ingenuously selecting the phase shifts between these in-plane and out-of-plane oscillations, the relative motion can trace distinct three-dimensional geometries, as illustrated in Figure 3.10 (D’Errico, 2012).

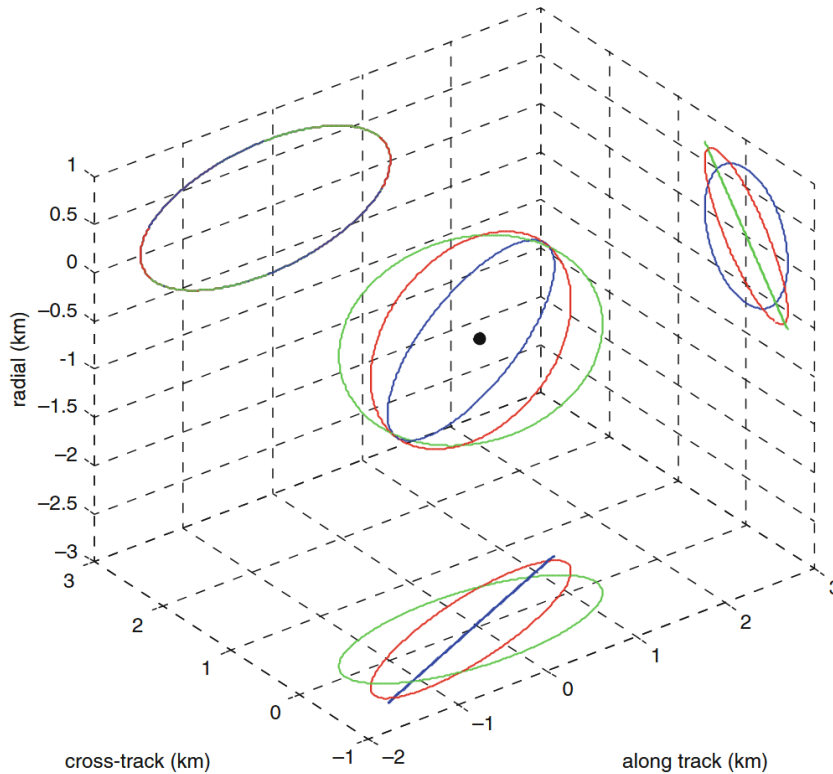


FIGURE 3.10 – 3D relative motion and its projection on the coordinate planes for a formation with  $e = 0.001$ ,  $a = 7,000$  km,  $\delta e = 1 \times 10^{-4}$ ,  $\delta\Omega = 0.005^\circ$ , and different choices for the two perigees ( $0^\circ, 45^\circ, 90^\circ$ ) (D’Errico, 2012).

The formation geometry outlined in red in Figure 3.10, which corresponds to a  $90^\circ$  phase shift, is known as the **helix formation**. This configuration is particularly valuable for applications like interferometry because it maintains a near-constant baseline distance. The specific dimensions of the helix can be precisely engineered to meet mission requirements by adjusting the relative orbital elements, primarily  $\delta e$  and  $\delta\Omega$ .

Furthermore, the helix formation is an inherently safe configuration that minimizes collision risk. Since the satellites are constantly separated across multiple axes, they are never aligned solely along the unstable along-track direction. This characteristic also allows mission controllers to design a safe formation breakup procedure by intentionally inducing the natural along-track drift to separate the satellites in a controlled manner (Kahle *et al.*, 2012).

A notable mission that successfully implemented this concept is the TanDEM-X (Krieger *et al.*, 2007). Figure 3.11 shows the historical relative motion between the TanDEM-X (deputy) and TerraSAR-X (chief) satellites. This example not only demonstrates the long-term stability of the helix formation but also illustrates how orbital perturbations, such as the differential J2 effect, can be strategically leveraged to modify the interferometric baseline over time, thereby optimizing the DEM acquisition plan (Krieger *et al.*, 2007).

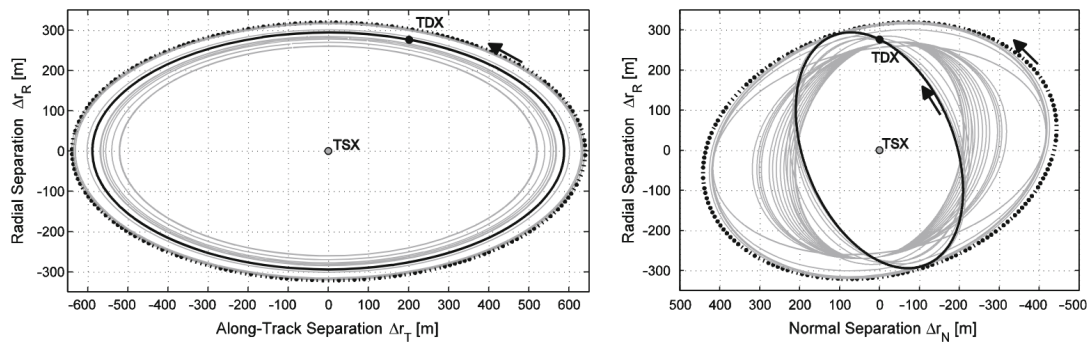


FIGURE 3.11 – Evolution of TDX-TSX relative motion in the Hill frame: radial-/along-track separation (left) and radial/normal separation (right). The formation geometries were flown during the period from December 2010 (dotted ellipse) to December 2011 (bold black ellipse). Arrows indicate the relative motion direction. The filled black circle indicates the TDX relative position at  $90^\circ$  argument of latitude (Kahle *et al.*, 2012; D’Errico, 2012).

### 3.4 Control Theory

Based on Equations 3.17, 3.18, and 3.19, the equations of motion can be augmented to include control inputs and disturbances, yielding Equations 3.25, 3.26, and 3.27 (Alfriend *et al.*, 2010).

$$\ddot{x} - 2n_0\dot{y} - 3n_0^2x = d_x + u_x \quad (3.25)$$

$$\ddot{y} + 2n_0\dot{x} = d_y + u_y \quad (3.26)$$

$$\ddot{z} + n_0^2 z = d_z + u_z \quad (3.27)$$

Once a mathematical model of the controlled relative dynamics is established, control strategies can be designed to manage the system's behavior. The objective is typically to track a desired relative trajectory by applying a control acceleration,  $\mathbf{u}$ , provided by thrusters. For design purposes, it is often assumed that the thrusters can be modulated to provide continuous control. Given that the Clohessy-Wiltshire equations are linear, the system can be represented in the standard state-space form (Ogata, 2010), as shown in Equation 3.28:

$$\dot{\mathbf{X}} = \mathbf{A}\mathbf{X} + \mathbf{B}\mathbf{U} \quad (3.28)$$

where  $\mathbf{X} = [x, y, z, \dot{x}, \dot{y}, \dot{z}]^T$  is the state vector,  $\mathbf{U} = [u_x, u_y, u_z]^T$  is the control input vector, and  $A$  and  $B$  are the system and input matrices, respectively. The system matrix  $A$ , which represents the linearized dynamics from Equations 3.25, 3.26, and 3.27, is defined as:

$$A = \begin{bmatrix} 0 & 0 & 0 & 1 & 0 & 0 \\ 0 & 0 & 0 & 0 & 1 & 0 \\ 0 & 0 & 0 & 0 & 0 & 1 \\ 3n_0^2 & 0 & 0 & 0 & 2n_0 & 0 \\ 0 & 0 & 0 & -2n_0 & 0 & 0 \\ 0 & 0 & -n_0^2 & 0 & 0 & 0 \end{bmatrix} \quad (3.29)$$

And the input matrix  $B$  is defined as:

$$B = \begin{bmatrix} 0 & 0 & 0 \\ 0 & 0 & 0 \\ 0 & 0 & 0 \\ 1 & 0 & 0 \\ 0 & 1 & 0 \\ 0 & 0 & 1 \end{bmatrix} \quad (3.30)$$

When considering orbital perturbations, the main influence on the relative dynamics is the differential effect of the Earth's oblateness ( $J_2$ ). This effect causes secular drifts in the right ascension of the ascending node ( $\Omega$ ), the argument of perigee ( $\omega$ ), and the mean anomaly ( $M$ ) (Alfriend *et al.*, 2010). By incorporating these differential secular drifts into the CW framework, the equations of relative motion are expressed as follows (Alfriend *et al.*, 2010):

$$\ddot{x} - 2\dot{M}_0\dot{y} - 3\dot{M}_0^2 x = -3n_0^2\delta a - 2n_0a_0(\delta\dot{\lambda} + \delta\dot{\Omega}\cos i_0) + u_x \quad (3.31)$$

$$\ddot{y} + 2\dot{M}_0\dot{x} = u_y \quad (3.32)$$

$$\ddot{z} + \dot{\lambda}_0^2 z = 2a_0\dot{\lambda}_0\delta\Omega\sin i_0\sin\lambda_0 + u_z \quad (3.33)$$

In these equations,  $\dot{M}_0$  and  $\dot{\lambda}_0$  denote the secular rates of change for the chief satellite's mean anomaly and mean argument of latitude, respectively. The terms  $\delta a$  and  $\delta\Omega$  represent the differences in the semi-major axis and the right ascension of the ascending node between the deputy and chief satellites. Furthermore,  $\delta\dot{\lambda}$  and  $\delta\dot{\Omega}$  are the differential secular rates of change in the mean argument of latitude and the right ascension of the ascending node, due to the  $J_2$  perturbation (Alfriend *et al.*, 2010). The terms  $u_x$ ,  $u_y$ , and  $u_z$  represent the control inputs.

Based on this expanded model, control strategies can be adapted to account for the additional dynamics introduced by orbital perturbations. The perturbation terms on the right-hand side of Equations 3.31, 3.32, and 3.33 can be treated as known disturbances. Therefore, the controller design can use the simpler state-space representation of Equation 3.28, ensuring that the control inputs,  $\mathbf{U}$ , effectively mitigate the effects of these perturbations on the relative motion of the satellites.

### 3.4.1 Linear Quadratic Regulator Controller

The Linear Quadratic Regulator (LQR) is an optimal control strategy designed for a linear time-invariant (LTI) system of the form  $\dot{\mathbf{X}} = \mathbf{A}\mathbf{X} + \mathbf{B}\mathbf{U}$ . The objective is to find a state-feedback control law  $\mathbf{U} = -\mathbf{K}\mathbf{X}$  that minimizes an infinite-horizon quadratic performance index, or cost function,  $\mathcal{J}$  (Ogata, 2010) defined in Equation 3.34.

$$\mathcal{J} = \frac{1}{2} \int_0^\infty (\mathbf{X}^T \mathbf{Q} \mathbf{X} + \mathbf{U}^T \mathbf{R} \mathbf{U}) dt \quad (3.34)$$

where  $\mathbf{Q}$  is a positive semi-definite ( $\mathbf{Q} \geq 0$ ) state weighting matrix and  $\mathbf{R}$  is a positive definite ( $\mathbf{R} > 0$ ) control weighting matrix. These weighted matrices are to be tuned based on the specific requirements of the control system and the desired performance characteristics.

The solution to this optimization problem is achieved through the following control law:

$$\mathbf{U}(t) = -\mathbf{K}\mathbf{X}(t) \quad (3.35)$$

where the constant gain matrix  $K$  is computed as  $K = R^{-1}B^T S$ . The matrix  $S$  is the unique, symmetric, positive definite solution to the continuous-time Algebraic Riccati Equation (ARE) in Equation 3.36 (Ogata, 2010).

$$A^T S + SA - SBR^{-1}B^T S + Q = 0 \quad (3.36)$$

### 3.4.2 Frequency Domain

While modern control strategies such as the Linear Quadratic Regulator (LQR) are formulated in the state-space, classical control theory offers powerful and intuitive methods grounded in the frequency domain. These methods rely on the Laplace Transform to convert the system's differential equations modeling into an algebraic representation. This transformation is fundamental to the analysis and design of classical controllers, including the Proportional-Integral-Derivative (PID) controller discussed subsequently (Ogata, 2010).

The application of the Laplace Transform leads to the concept of the *transfer function*, which provides a model of a Linear Time-Invariant (LTI) system's input-output dynamics. The transfer function  $G(s)$  in Equation 3.37 is defined as the ratio of the Laplace Transform of the output,  $Y(s)$ , to the Laplace Transform of the input control,  $U(s)$ , assuming zero initial conditions.

$$G(s) = \frac{Y(s)}{U(s)} \quad (3.37)$$

where  $s$  represents the complex frequency variable of the Laplace domain.

The transfer function encapsulates the intrinsic dynamics of the system. The roots of its denominator polynomial, known as poles, govern the system's stability. For a continuous Linear Time-Invariant (LTI) system to be stable, all its poles must lie in the left-half of the complex  $s$ -plane, which requires that their real parts be negative. Graphical analysis methods, such as the Root Locus, Bode plots, and the Nyquist stability criterion, utilize the transfer function to evaluate system performance (Ogata, 2010). Key metrics derived from these methods include gain and phase margins, which are critical indicators of relative stability (Ogata, 2010).

### 3.4.3 Time Domain

Complementing the frequency-domain analysis, time-domain performance metrics are essential for assessing the behavior of control systems. These metrics of rise time, overshoot, settling time, and steady-state error are central to characterizing the dynamic response of a system and, consequently, fundamental to the optimization problem addressed

in this study.

Figure 3.12 illustrates the transient time response of a standard second-order system to a unit-step input, highlighting the key performance metrics commonly used in time-domain analysis (Ogata, 2002).

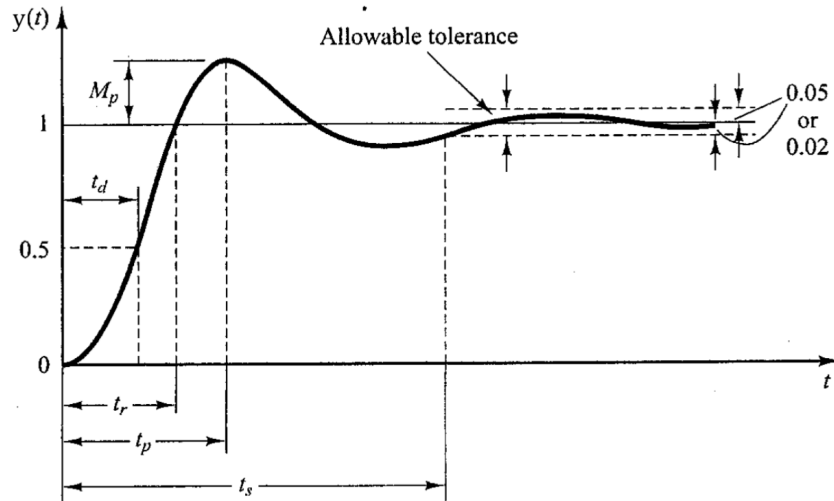


FIGURE 3.12 – Transient response of a unit-step input showing rise time, overshoot, settling time, and steady-state error (Ogata, 2002).

The performance metrics shown in Figure 3.12 are defined as follows:

- **Rise Time ( $t_r$ ):** The time required for the system response to increase from 0% to 100% of its final value.
- **Overshoot ( $M_p$ ):** The amount by which the response's maximum peak exceeds the final value, typically expressed as a percentage. This occurs at the peak time ( $t_p$ ).
- **Settling Time ( $t_s$ ):** The time taken for the response to enter and remain within a specified tolerance band (commonly 2% or 5%) of its final value.
- **Steady-State Error ( $e_{ss}$ ):** The difference between the desired setpoint and the actual output of the system as time approaches infinity.

The dynamic equations employed in this study yield second-order system responses, as demonstrated later in Section 4.2. Hence, the time-domain performance metrics described above are directly applicable for assessing the quality of the optimized control strategies implemented for satellite formation flying.

### 3.4.4 Proportional-Integral-Derivative (PID) Controller

The PID controller is one of the most widely implemented feedback control structures in industrial and aerospace applications due to its simplicity, reliability, and effectiveness (Ogata, 2010). It calculates a control action  $u(t)$  based on a weighted sum of the present error  $e(t)$ , the accumulation of past errors, and a prediction of future errors. The error signal is defined as the difference between a desired setpoint and the measured output. The PID control law in the time domain is formulated as shown in Equation 3.38 (Ogata, 2010).

$$u(t) = K_p e(t) + K_i \int_0^t e(\tau) d\tau + K_d \frac{de(t)}{dt} \quad (3.38)$$

where  $K_p$ ,  $K_i$ , and  $K_d$  are the proportional, integral, and derivative gains, respectively. Each term serves a distinct purpose:

- **Proportional Term ( $K_p$ ):** This term provides a control action proportional to the current error. A higher  $K_p$  gain results in a faster system response but can increase overshoot and system oscillations.
- **Integral Term ( $K_i$ ):** This term is proportional to accumulative error. By integrating the error over time, it generates a control action that drives the steady-state error to zero for step inputs. However, it can destabilize the system if not properly tuned, leading to increased overshoot and oscillatory behavior.
- **Derivative Term ( $K_d$ ):** This term is proportional to the rate of change of the error. It acts predictively, providing a damping effect that reduces overshoot and improves the transient response.

Applying the Laplace Transform to Equation 3.38 and assuming zero initial conditions, we obtain the transfer function of the PID controller,  $C(s)$ :

$$C(s) = \frac{U(s)}{E(s)} = K_p + \frac{K_i}{s} + K_d s = \frac{K_d s^2 + K_p s + K_i}{s} \quad (3.39)$$

This transfer function representation is fundamental for designing and tuning the PID controller within the frequency-domain framework. The tuning of the gains  $K_p$ ,  $K_i$ , and  $K_d$  is a critical process aimed at achieving a desired balance between performance metrics such as rise time, overshoot, settling time, and steady-state error as shown in Figure 3.12. The integral and derivative gains can also be expressed in terms of time constants,  $T_i$  and  $T_d$ , respectively, as shown in Equation 3.40.

$$K_i = \frac{K_p}{T_i}, \quad K_d = K_p T_d \quad (3.40)$$

### 3.4.5 Ziegler-Nichols Tuning Method

The Ziegler-Nichols tuning method is a heuristic approach for determining initial parameters for a PID controller based on the system's response characteristics (Ogata, 2010). This approach consists of two main methods: the step-response method and the frequency-response method.

The first method, based on the open-loop response, is applied to systems that exhibit a damped, S-shaped unit-step response curve. From this curve, characteristic parameters (such as time delay and time constant) are found by drawing a tangent line at the inflection point. The PID gains are then set according to tabulated rules based on these parameters (Ogata, 2010). Since the system under study is naturally unstable and oscillatory, this method is not suitable for the problem at hand and will not be discussed further.

The second method, called the **ultimate-gain** or **closed-loop** method, is used for this work. This procedure involves setting the controller to pure proportional action ( $T_i = \infty$ ,  $T_d = 0$ ) and gradually increasing the proportional gain ( $K_p$ ) from a small value until the closed-loop response exhibits sustained, approximately sinusoidal oscillations. The gain value at which this occurs is called the **critical gain** ( $K_{cr}$ ), and the period of these oscillations is the **critical period** ( $P_{cr}$ ). These two experimentally determined values,  $K_{cr}$  and  $P_{cr}$ , are then used to set the initial PID gains based on the rules shown in Table 3.1 (Ogata, 2010).

TABLE 3.1 – Ziegler–Nichols tuning rules based on the critical gain  $K_{cr}$  and the critical period  $P_{cr}$  (second method) (Ogata, 2010)

Controller Type	$K_p$	$T_i$	$T_d$
P	$0.5K_{cr}$	$\infty$	0
PI	$0.45K_{cr}$	$P_{cr}/1.2$	0
PID	$0.6K_{cr}$	$0.5P_{cr}$	$0.125P_{cr}$

These rules provide an educated starting point for controller tuning. The resulting system may still exhibit significant overshoot, so fine-tuning is often necessary to meet specific performance requirements (Ogata, 2010).

## 3.5 Optimization

The optimization process requires the definition of an objective function that guides the derivation of optimal solutions, as well as the specification of constraints that these solutions must satisfy. In the context of the space mission and the specific requirements

of the formation flying problem, two objective functions were established: the Integral of Time-weighted Absolute Error (ITAE) (Bansal; Sharma; Ponpathirkoottam, 2012), presented in Equation 3.41, representing the state error, and the total  $\Delta V$ , presented in Equation 3.42, representing the control usage.

$$\mathcal{J}_{ITAE} = \int_0^{t_f} t \|e(t)\| dt \quad (3.41)$$

$$\Delta V = \int_0^{t_f} \|u(t)\| dt \quad (3.42)$$

### 3.5.1 Metaheuristics Methods

The optimization algorithms utilized in this work are metaheuristic methods, which are designed for the efficient exploration of complex solution spaces. Figure 3.13 provides a schematic illustration of the general classification of these techniques.

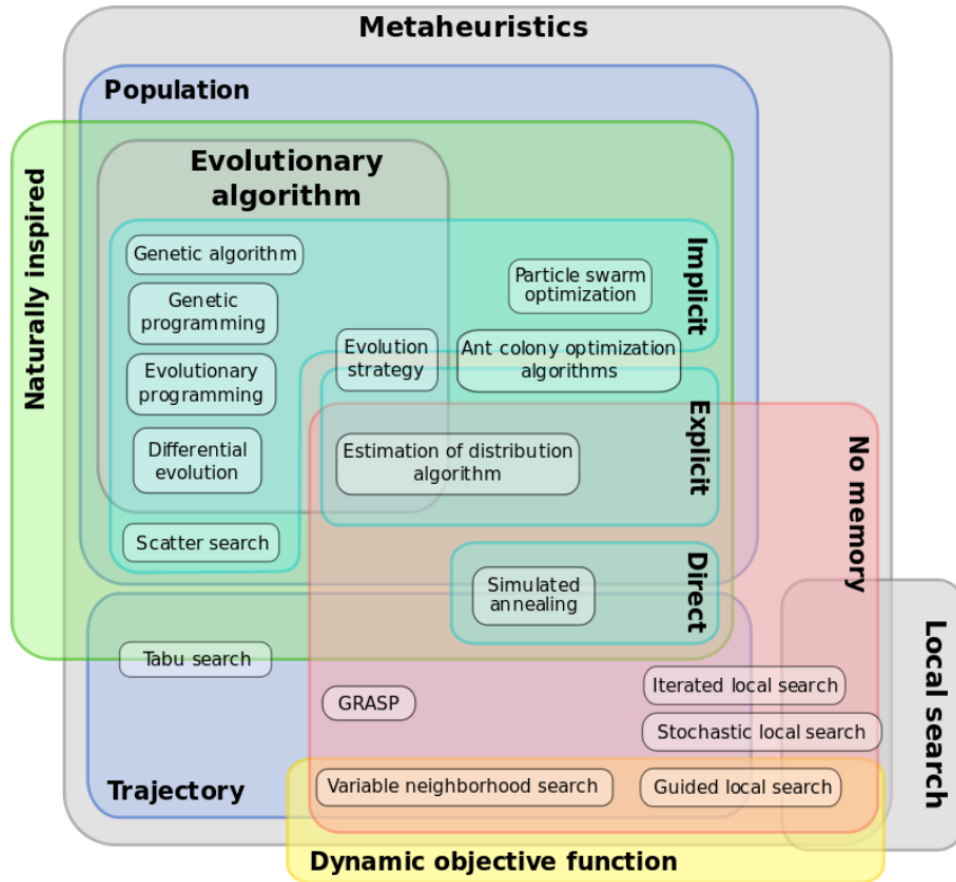


FIGURE 3.13 – Classification of metaheuristic methods (Naimi Sadigh *et al.*, 2012).

Based on the taxonomy presented in Figure 3.13, the algorithms employed here primarily fall under the naturally inspired region. This region is categorized by its source of

inspiration: Evolutionary Algorithms are inspired by biological evolution, encompassing processes such as selection, recombination, and mutation. Swarm Intelligence algorithms model the collective behavior of social animals and insects. Physical Algorithms draw inspiration from natural physical processes, such as the cooling and crystallization of materials.

Beyond their natural inspiration, metaheuristic algorithms are further distinguished by several key characteristics related to their operational mechanics:

- **Population-based and Trajectory-based:** Population methods, like genetic algorithms (Beasley; Bulley; Martin, 1993) and particle swarm optimization (Wang; Tan; Liu, 2017), maintain and evolve a set of candidate solutions simultaneously. In contrast, trajectory methods, such as simulated annealing (Corana *et al.*, 1989), iteratively improve a single candidate solution by exploring its neighborhood over time.
- **Memory Usage:** Some algorithms incorporate memory to guide the search process, which helps in avoiding previously explored areas or getting stuck in cycles. Others, such as the fundamental forms of simulated annealing and covariance matrix adaptation evolution strategy (Hansen, 2006), are often classified as memoryless because their exploration process does not explicitly account for past candidate solutions beyond the current state or population.
- **Search Strategy (Implicit, Explicit, or Direct):** This classification relates to how solutions are represented and manipulated. **Implicit strategies** use an indirect model or representation, such as particle velocities (Wang; Tan; Liu, 2017), pheromone trails (Chiha; Liouane; Borne, 2012), or gene codification (Beasley; Bulley; Martin, 1993), to guide the search process. **Explicit strategies** build a probabilistic model (Hansen, 2006) of promising solutions from which new candidates are sampled. **Direct strategies** use the objective function values (Corana *et al.*, 1989) directly to guide the search.

Leveraging the capabilities of the Python library PyGMO (Biscani; Izzo, 2020) and aiming for a comprehensive exploration across different branches of metaheuristic methods, the following algorithms were selected for this study:

- **ACO:** Extended Ant Colony Optimization
- **DE:** Differential Evolution
- **SADE:** Self-Adaptive Differential Evolution

- **PSO**: Particle Swarm Optimization
- **SGA**: Simple Genetic Algorithm
- **SA**: Corana’s Simulated Annealing
- **CMA-ES**: Covariance Matrix Adaptation Evolution Strategy
- **NSPSO**: Non-dominated Sorting Particle Swarm Optimization
- **MHACO**: Multiobjective Hypervolume-based Ant Colony Optimization
- **GMOEAD**: Multiobjective Evolutionary Algorithm with Decomposition Generational (Differential Evolution Variant)
- **MOEAD**: Multiobjective Evolutionary Algorithm with Decomposition (Differential Evolution Variant)
- **NSGA2**: Non-dominated Sorting Genetic Algorithm II

These algorithms were chosen for their diverse optimization approaches, facilitating a thorough analysis of the problem at hand. Importantly, the algorithms listed are a mixture of methods designed for single objective optimization (ACO, DE, SADE, PSO, SGA, SA, CMA-ES) and those specifically adapted for multiobjective problems (LIU; YANG; WHIDBORNE, 2003) (NSPSO, MHACO, GMOEAD, MOEAD, NSGA2). This selection ensures a broad coverage of unique strengths and weaknesses regarding exploration versus exploitation, convergence speed, and parameter sensitivity, making them collectively suitable for a comprehensive study across different optimization challenges.

### 3.5.2 Multiobjective Optimization

Since the defined optimization goal emphasizes minimizing both position errors and control usage, it is necessary to adopt a formulation that enables the use of single objective metaheuristic algorithms, in addition to multiobjective metaheuristic techniques.

Given this focus, one suitable alternative is to transform the original multiobjective problem into a single objective one through an additional formulation step. The  $\varepsilon$ -constraints method accomplishes this by converting a multiobjective optimization problem into a series of single objective problems (Bierlaire, 2020). It does so by selecting one of the objectives as the primary target for minimization, while imposing upper bounds on the remaining objectives .

Specifically, for a problem involving two objectives, a reference objective  $\ell$  is selected, and upper bounds  $\varepsilon_i$  are defined for the other objective. The resulting constrained optimization problem is formulated as:

$$\min_{x \in F} f_\ell(x) \quad (3.43)$$

subject to:

$$f_i(x) \leq \varepsilon_i, \quad \forall i \neq \ell \quad (3.44)$$

where  $f_\ell(x)$  is the objective function corresponding to the chosen reference objective, and  $F$  denotes the feasible region defined by the constraints and search space bounds.

This method guarantees that, if a solution exists, it is weakly Pareto-optimal (Bierlaire, 2020) — meaning that no other feasible solution can improve all objectives simultaneously without deteriorating at least one of them. By systematically varying the bounds  $\varepsilon_i$ , this approach yields a set of Pareto-optimal solutions, offering a practical framework for exploring trade-offs in multiobjective optimization.

In this work, the primary objective function selected as the reference was control usage, represented by the  $\Delta V$  budget. The state errors were treated as constraints, defined such that the error must not exceed a specified threshold. This threshold can be further adjusted based on mission requirements or specific imaging conditions.

Another approach is to address the problem characterized by often competing objectives to be minimized simultaneously (LIU; YANG; WHIDBORNE, 2003). Unlike single objective optimization where a single best solution typically exists, multiobjective optimization usually has no single optimal solution that optimizes all objectives at once due to inherent conflicts. Instead, it achieves a set of equally efficient, non-inferior, alternative solutions known as the Pareto-optimal set. Figure 3.14 illustrates this concept for two objective functions,  $\phi_1(p)$  and  $\phi_2(p)$ , dependent on a design parameter vector  $p$ . The shaded region represents the "Attainable set" of all possible objective value pairs achievable by varying  $p$ .

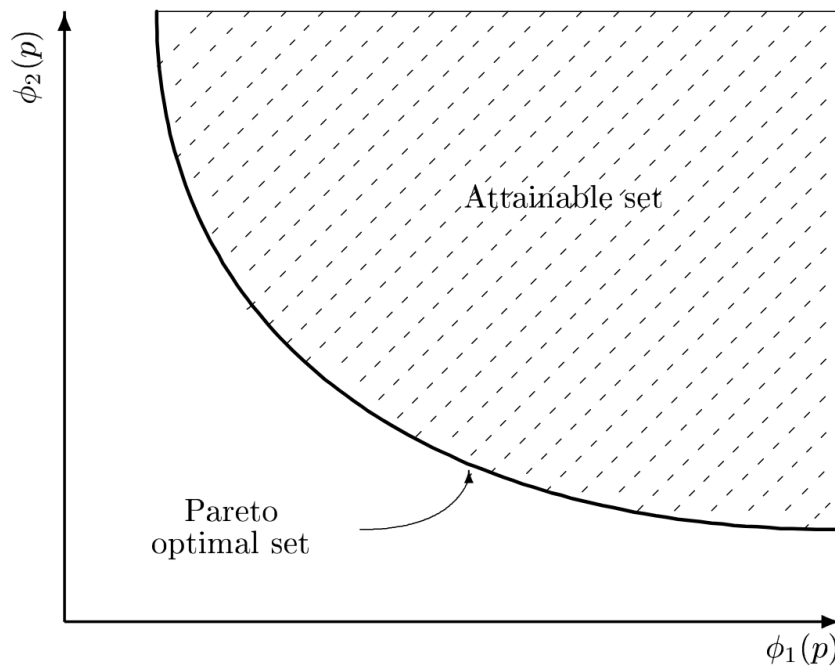


FIGURE 3.14 – A Pareto-optimal set (LIU; YANG; WHIDBORNE, 2003).

The boundary curve highlighted as the "Pareto optimal set" contains solutions where it is impossible to improve one objective without worsening the other. Moreover, any point inside the attainable set is suboptimal because both objectives could potentially be improved simultaneously. Therefore, multiobjective optimization identifies this Pareto-optimal frontier, presenting the designer with a range of optimal trade-off solutions from which a final compromise design must be selected. This framework transforms the technical challenge of optimization into a rational selection based on fully mapped engineering compromises.

### 3.5.3 Statistical Validation Framework

The metaheuristic algorithms explored in this work are stochastic, meaning their performance can vary from run to run due to inherent randomness. Consequently, comparing algorithms based on a single simulation run is insufficient and can lead to misleading conclusions.

To ensure a robust and statistically valid comparison, the methodology employs multiple independent simulation runs for each algorithm. The required number of runs must be sufficient to ensure the mean performance of an algorithm can be estimated with a specified level of confidence.

This study adopts a 95% confidence interval ( $\alpha = 0.05$ ), and the minimum sample size  $n$  is determined using the standard formula for mean estimation (NIST/SEMATECH,

2023) shown in Equation 3.45:

$$n = \frac{Z_{\alpha/2}^2 \sigma^2}{E_0^2} \quad (3.45)$$

where  $n$  is the required sample size,  $Z_{\alpha/2}$  is the critical value from the standard normal distribution (1.96 for a 95% confidence level),  $\sigma$  is the population standard deviation (estimated from preliminary samples), and  $E_0$  is the desired margin of error. As detailed in the next chapter, this approach justifies the number of simulation runs performed, ensuring the final comparisons are statistically significant.

# 4 Methodology

This section describes the methodology employed for the development of the numerical simulation and the statistical analysis of the resulting data. It is divided into five main parts: the first outlines the software tools utilized, the second presents a classical stability analysis of the system, the third details the numerical simulation procedure, the fourth describes the decision variables definition, and the fifth explains the statistical analysis of the collected data. Additionally, this section highlights potential points of limitations of the study, as well as possible alternatives and improvements to be considered in future, for more advanced research.

## 4.1 Software

The development of a simulation environment for satellite formation control and its subsequent optimization requires the use of appropriate software tools. Since this study involves the simulation of complex dynamic systems and the analysis of controller optimization, both of which demand speed and computational efficiency, the choice of software must meet these requirements. The main criteria guiding this selection can be summarized as follows:

- **Numerical Computation Suitability:** The programming language shall support high-performance numerical computation and scientific analysis.
- **Availability of Scientific Libraries:** The software shall provide access to robust and well-maintained libraries and frameworks specifically designed for numerical simulation, control systems, and optimization tasks.
- **Data Visualization Capabilities:** The environment shall include tools for visualizing simulation outputs, including time-series plots, histograms, error metrics, and three-dimensional representations for enhanced interpretation of results.
- **Integration with Research Community:** The software shall be widely adopted

within the scientific and engineering communities, facilitating collaboration, reproducibility, and access to existing knowledge bases and resources.

Based on the outlined requirements, the most suitable programming languages that receive ongoing updates and offer the desired features are **Fortran**, **Python**, **MATLAB**, **Julia**, and **C++**. Table 4.1 provides a comparative analysis of these languages according to the defined selection criteria. Each criterion is rated on a qualitative scale (Limited, Moderate, Good, or Excellent) to reflect the overall suitability of each language for the scope of this study.

The evaluation of numerical suitability considers the language’s efficiency in handling computational tasks typical of astrodynamics systems (Eichhorn *et al.*, 2018). The evaluation of scientific libraries and visualization tools are assessed through qualitative analysis of their documentation, functionality, and integration capabilities (Harris *et al.*, 2020; Virtanen *et al.*, 2020; Rackauckas; Nie, 2017; The MathWorks Inc., 2025a,b). Finally, the research community criterion is based on the accessibility of resources, community support, active forums, and the volume of scientific publications associated with each language.

TABLE 4.1 – Comparison of Programming Languages for Simulation and Optimization

<b>Criterion</b>	<b>Fortran</b>	<b>Python</b>	<b>MATLAB</b>	<b>Julia</b>	<b>C++</b>
Numerical Suitability	Excellent	Moderate	Moderate	Excellent	Excellent
Scientific Libraries	Excellent	Excellent	Good	Excellent	Moderate
Visualization tools	Limited	Excellent	Good	Excellent	Limited
Research Community	Excellent	Excellent	Excellent	Good	High

Considering a development environment that includes metaheuristic optimization libraries supporting parallel processing, Python stands out as one of the most suitable choices due to the availability of PyGMO (Biscani; Izzo, 2020). It also offers a broad range of scientific libraries, such as NumPy (Harris *et al.*, 2020), SciPy (Virtanen *et al.*, 2020), and Matplotlib, which facilitate data manipulation, numerical computation, and result visualization. Moreover, Python is widely used in the scientific and academic communities, particularly within the German Aerospace Center (DLR), where this study was initially developed.

As for **MATLAB**, it is a powerful tool for numerical computation and visualization, but it is not open-source and requires a paid license, limiting future development and reproducibility. **Julia**, although delivering high performance compared to other interpreted languages and offering a well-structured ecosystem of libraries for numerical and scientific work, is still relatively new and lacks extensive research community support. **C++** is a ro-

bust language for high-performance applications but may require more development time and effort for rapid prototyping and simulation tasks.

## 4.2 Classical Control Analysis

The dynamics of the Z-axis, as described by Equation 3.27, are decoupled from the in-plane motion. For this stability analysis, we consider the disturbance  $d_z$  and the reference position to be zero. The transfer function of the plant (Ogata, 2010) is:

$$G_p(s) = \frac{Z(s)}{U_z(s)} = \frac{1}{s^2 + n_0^2} \quad (4.1)$$

The general form of a PID controller is  $C(s) = K_p + \frac{K_i}{s} + K_d s$ . The resulting closed-loop characteristic equation for the system is:

$$s^3 + K_d s^2 + (n_0^2 + K_p)s + K_i = 0 \quad (4.2)$$

For a third-order polynomial  $s^3 + as^2 + bs + c = 0$  to have all its roots in the left half-plane, it is necessary and sufficient that all coefficients are positive and that the condition  $ab > c$  is met. We will now analyze the stability for each controller type by specializing this general equation.

### 4.2.1 Proportional (P) Controller

For a P controller, we set  $K_d = 0$  and  $K_i = 0$ , reducing the characteristic equation to:

$$s^2 + (n_0^2 + K_p) = 0 \quad (4.3)$$

The roots are  $s = \pm\sqrt{-(n_0^2 + K_p)}$ . For the roots to be purely imaginary, which results in sustained oscillations, the term under the square root must be negative, requiring  $n_0^2 + K_p > 0$ . Since the real part of the roots is always zero, a proportional controller alone can only achieve marginal stability and cannot asymptotically stabilize the system.

### 4.2.2 Proportional-Integral (PI) Controller

For a PI controller, we set  $K_d = 0$ , and the characteristic equation becomes:

$$s^3 + (n_0^2 + K_p)s + K_i = 0 \quad (4.4)$$

This is a third-order polynomial with the  $s^2$  term missing. From the polynomial's properties, we know that the sum of its roots ( $s_1, s_2, s_3$ ) equals the negative of the coefficient of the  $s^2$  term, which is zero. Therefore,  $s_1 + s_2 + s_3 = 0$ . It is impossible for all three roots to have negative real parts, as their sum must be negative. At least one root must have a non-negative real part, rendering the system unstable. Thus, a PI controller alone cannot stabilize this system.

### 4.2.3 Proportional-Derivative (PD) Controller

For a PD controller, we set  $K_i = 0$  in the general characteristic equation, which reduces to a second-order polynomial:

$$s^2 + K_d s + (n_0^2 + K_p) = 0 \quad (4.5)$$

The roots of this quadratic equation are  $s = \frac{-K_d \pm \sqrt{K_d^2 - 4(n_0^2 + K_p)}}{2}$ . For the roots to have negative real parts, it is required that  $\text{Re}(s) = -K_d/2 < 0$ , which implies  $K_d > 0$ . Furthermore, for a second-order system to be stable, all coefficients must be positive. This leads to the following conditions for asymptotic stability:

1.  $K_d > 0$
2.  $n_0^2 + K_p > 0$

Note that while a PD controller can stabilize the system, it cannot eliminate steady-state error in response to constant disturbances or setpoint changes (Ogata, 2010), rendering this solution only marginally acceptable for ideal scenarios without perturbations.

### 4.2.4 Proportional-Integral-Derivative (PID) Controller

For the full PID controller, the characteristic equation is given by Equation 4.2. Applying the stability conditions for a cubic polynomial with  $a = K_d$ ,  $b = n_0^2 + K_p$ , and  $c = K_i$ , we find that for asymptotic stability, assuming positive gains, the following conditions must be satisfied:

1.  $K_d > 0$
2.  $K_i > 0$
3.  $n_0^2 + K_p > 0$
4.  $K_d(n_0^2 + K_p) > K_i$

Therefore, we can infer that a PID controller is viable for this ideal linear system, as it can provide asymptotic stability and eliminate steady-state error. This suggests that, with proper tuning, a PID controller might be able to handle the complete nonlinear dynamics and perturbations of the spacecraft formation flying system.

### 4.3 Simulation

The simulation framework for this study was developed using the Python programming language, taking advantage of its extensive libraries for numerical computation and scientific analysis, as well as the parallel processing capabilities provided by the PyGMO library (Biscani; Izzo, 2020).

Based on SAR space missions, three simulation scenarios were derived, each representing a satellite formation with different characteristics and objectives. These scenarios were designed to assess the effectiveness of the proposed controller optimizations under varying operational conditions. Table 4.2 describes the specifications of each scenario, including the type of orbit, satellite altitude, adopted formation, and inter-satellite separation parameters. The orbital definition was inspired by the TanDEM-X (TDX) mission (Krieger *et al.*, 2007), which employs a Sun-synchronous orbit (SSO) at an altitude of 508 km with a helical formation, aiming to reflect an orbital configuration more closely aligned with typical choices in SAR mission design.

In particular, three distinct formation flying geometries were selected: the H3 helical formation from TanDEM-X (Krieger *et al.*, 2007), the Rx1 helical formation from MirrorSAR (Mittermayer *et al.*, 2022), and the Small Baseline formation with CubeSats as an extension of TanDEM-X (Nogueira Peixoto *et al.*, 2023). These formations were chosen to represent different flight configurations that align with the assumptions of this study—specifically, the requirement for small separations between the satellites in certain SAR applications to ensure signal coherence and to validate the use of linearized equations as suitable models for control formulation. Moreover, the actuator is inspired by an ambipolar thruster system (Sheehan *et al.*, 2015), which is capable of providing a low-thrust propulsion of 4 mN on all three axes of the local orbital frame, making it suitable for the selected formations, considering small satellites of 100 kg.

TABLE 4.2 – Formation geometry and initial conditions for the simulation scenarios.

Parameters	TanDEM-X	MirrorSAR	CubeSat add-on TanDEM-X
Orbit type	SSO (TDX)	SSO (TDX)	SSO (TDX)
Altitude [km]	508	508	508
Formation	Helix H3	Helix Rx1	Helix Small baseline
Out-plane separation [m]	550	250	157
In-plane separation [m]	440	157	126
Initial error [m]	1	1	1

The simulation campaign was structured in two distinct parts to systematically evaluate the proposed hypotheses. The complete set of test combinations, which includes different formation flying geometries, optimization strategies, controllers, and guidance references, is outlined in Figures 4.1 and 4.2.

The first part, outlined in Figure 4.1, was designed to test the hypothesis that the optimization results are independent of the formation’s geometry.

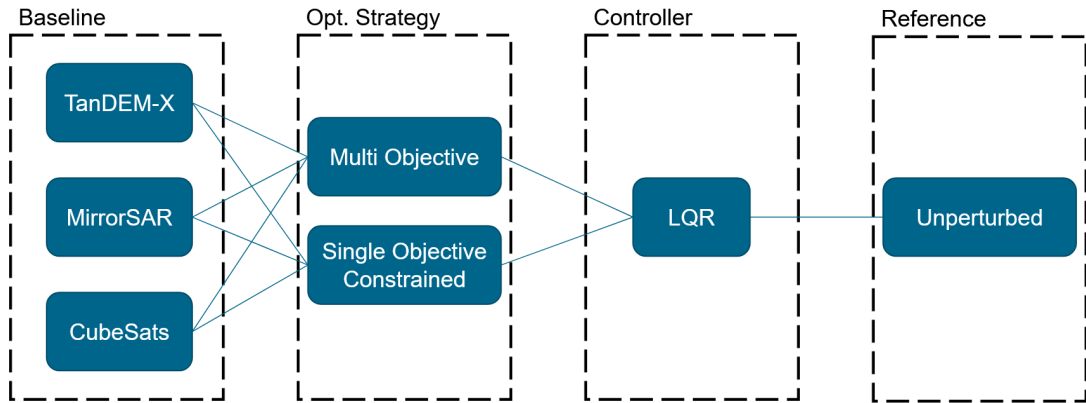


FIGURE 4.1 – Simulation test scenarios for the geometry-independence hypothesis.

The second part, outlined in Figure 4.2, focused on analyzing the performance of various optimization algorithms. Based on the assumption of geometry-independence, this analysis was conducted exclusively using the TanDEM-X formation geometry for simplicity. A practical control scenario for mission design, where radial thrust is considered dispensable (Alfriend *et al.*, 2010), was also included in the tests.

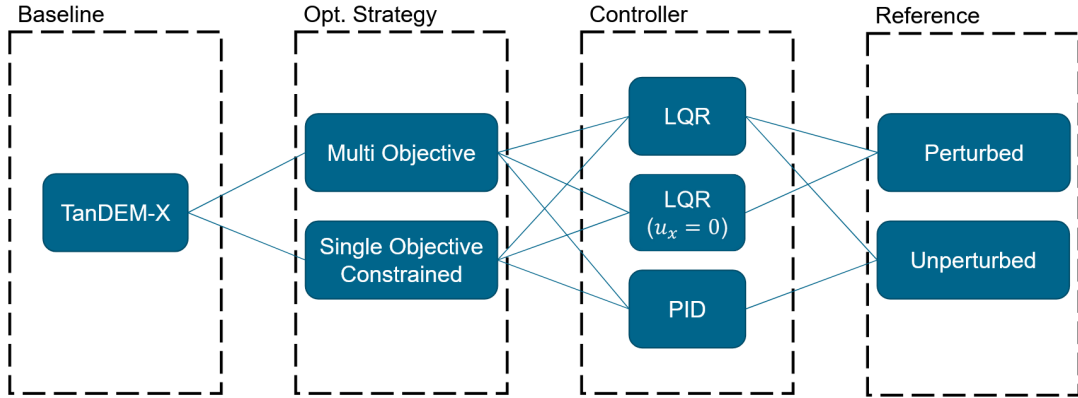


FIGURE 4.2 – Simulation test scenarios for the optimization analysis.

The *guidance perturbed reference* refers to a reference trajectory that incorporates the orbital perturbations discussed in Section 3.2.4, while the *guidance unperturbed reference* refers to a reference trajectory that nullifies these perturbations. In both cases, the initial error presented in Table 4.2 is taken into account.

To ensure statistically significant results, each test scenario was executed for  $n$  independent runs. The value of  $n$  was determined *a posteriori* using sampling theory based on Equation 3.45 to achieve a 95% confidence level in the statistical inferences. Based on the variance observed in preliminary trials, the number of repetitions was set to  $n = 10$  for every test case and optimization algorithm (both single and multi-objective). The complete simulation workflow, repeated for each run, is depicted in Figure 4.3.

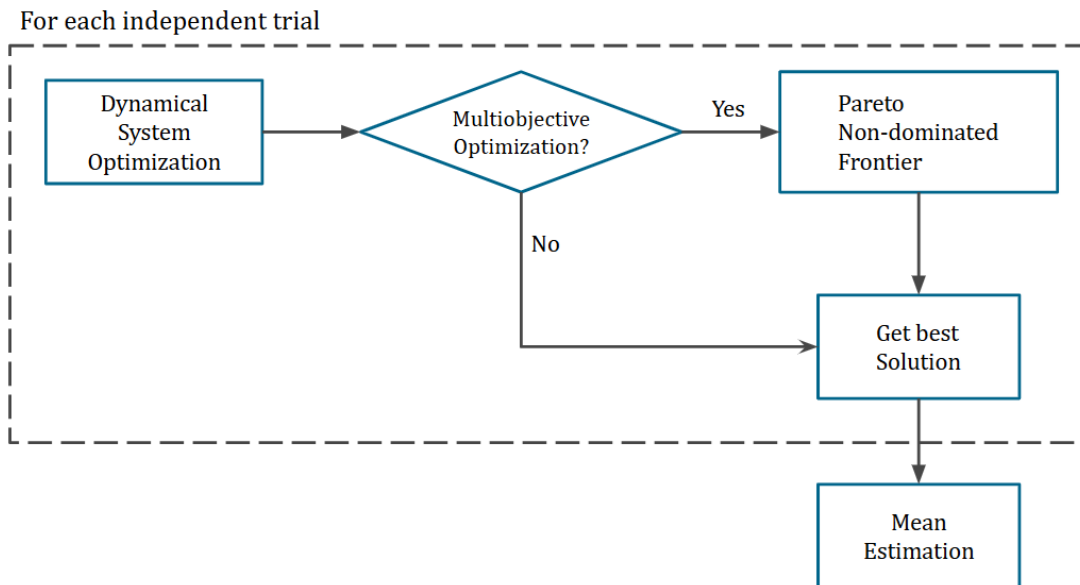


FIGURE 4.3 – Simulation workflow.

Aiming for a good balance between accuracy and simulation running time, the integrator available in SciPy (Virtanen *et al.*, 2020) chosen to solve the system's differential

equations was LSODA (Petzold, 1983), an adaptive, mixed-order integrator capable of handling both stiff and non-stiff systems. The integrator’s precision and simulation time settings were configured as shown in Table 4.3, ensuring sufficiently accurate results for the proposed simulations, inspired by the General Mission Analysis Tool (GMAT) (Hughes, 2007).

TABLE 4.3 – Numerical integration parameters.

<b>Parameters</b>	<b>Value</b>
Integrator	LSODA
Time	15 orbits ( $\sim 1$ day)
Max time step	2700 seconds
Absolute tolerance	$10^{-10}$
Relative tolerance	$10^{-10}$

The bounds for the optimization variables were established based on the system’s physical constraints and refined through preliminary analysis to identify intervals that yield a stable control response, as detailed in Table 4.4. These bounds ensure the optimization process operates within feasible limits that reflect realistic operational conditions. For the LQR controller, the weight matrix bounds were based on the standard literature values and further exploration of the search space, as illustrated in Figure 5.1. In contrast, the PID controller gain ranges were defined based on the stability analysis from Section 4.2, ensuring the search is centered on values known to produce stable responses.

Additionally, the search space was defined on a logarithmic scale. This approach allows the optimization algorithms to efficiently explore a wide range of values. Since typical solutions span several orders of magnitude, from  $10^{-12}$  to  $10^{15}$ , a linear scale would introduce an undesirable bias toward higher-valued parameters. This would hinder an effective exploration of the entire search space and reduce the overall efficiency of the optimization process.

TABLE 4.4 – Bounds of the optimization variables.

<b>Parameters</b>	<b>Control</b>	<b>Bounds (<math>10^k</math>)</b>
$Q$	LQR	[0, 8]
$R$	LQR	[4, 15]
$K_p$	PID	[-12, 2]
$K_i$	PID	[-12, -6]
$K_d$	PID	[-6, 2]

The tuning of parameters in each algorithm becomes less critical when the optimization is executed over a sufficient number of generations or iterations to guarantee convergence,

combined with a reasonably sized population (for methods where this metric is applicable). In such cases, the choice of the metaheuristic tuning parameters primarily influences the convergence speed rather than the quality of the final solution, which remains unaffected (Beasley; Bulley; Martin, 1993).

## 4.4 Decision Variables

Based on the optimization variables and bounds defined in Table 4.4, the optimization process was conducted for different configurations of the LQR weight matrices,  $Q$  and  $R$ , as defined in Section 3.4.1. This was accomplished by partitioning the diagonal matrices to create different sets of decision variables, hence, defining several variations of the optimization problem.

Initially, a simple configuration with only two decision variables,  $\{q, r\}$ , was considered, as shown in Equation 4.6. In this setup, the state weighting matrix,  $Q$ , penalizes all state errors (position and velocity) equally with a single weight  $q$ , and the control weighting matrix,  $R$ , penalizes the control effort in all three axes equally with a single weight  $r$ .

$$Q = \begin{bmatrix} q & 0 & 0 & 0 & 0 & 0 \\ 0 & q & 0 & 0 & 0 & 0 \\ 0 & 0 & q & 0 & 0 & 0 \\ 0 & 0 & 0 & q & 0 & 0 \\ 0 & 0 & 0 & 0 & q & 0 \\ 0 & 0 & 0 & 0 & 0 & q \end{bmatrix} \quad R = \begin{bmatrix} r & 0 & 0 \\ 0 & r & 0 \\ 0 & 0 & r \end{bmatrix} \quad (4.6)$$

The second step involved increasing the complexity to three decision variables,  $\{q_x, q_v, r\}$ , as shown in Equation 4.7. This breakdown separates the penalty on position errors from the penalty on velocity errors. The matrix  $Q$  was partitioned, applying the weight  $q_x$  to all position error states and  $q_v$  to all velocity error states, while the control weighting matrix  $R$  remained isotropic with a single weight  $r$ .

$$Q = \begin{bmatrix} q_x & 0 & 0 & 0 & 0 & 0 \\ 0 & q_x & 0 & 0 & 0 & 0 \\ 0 & 0 & q_x & 0 & 0 & 0 \\ 0 & 0 & 0 & q_v & 0 & 0 \\ 0 & 0 & 0 & 0 & q_v & 0 \\ 0 & 0 & 0 & 0 & 0 & q_v \end{bmatrix} \quad R = \begin{bmatrix} r & 0 & 0 \\ 0 & r & 0 \\ 0 & 0 & r \end{bmatrix} \quad (4.7)$$

To further refine the control allocation, the optimization was extended to five decision

variables:  $\{q_x, q_v, r_x, r_y, r_z\}$ . As shown in Equation 4.8, this configuration maintains the partitioned state weighting matrix  $Q$  but introduces an anisotropic control weighting matrix  $R$ . The weights  $r_x, r_y,$  and  $r_z$  allow for different penalties on the control effort along each of the respective axes in the local frame.

$$Q = \begin{bmatrix} q_x & 0 & 0 & 0 & 0 & 0 \\ 0 & q_x & 0 & 0 & 0 & 0 \\ 0 & 0 & q_x & 0 & 0 & 0 \\ 0 & 0 & 0 & q_v & 0 & 0 \\ 0 & 0 & 0 & 0 & q_v & 0 \\ 0 & 0 & 0 & 0 & 0 & q_v \end{bmatrix} \quad R = \begin{bmatrix} r_x & 0 & 0 \\ 0 & r_y & 0 \\ 0 & 0 & r_z \end{bmatrix} \quad (4.8)$$

The most detailed configuration utilized nine decision variables,  $\{q_x, q_y, q_z, q_{vx}, q_{vy}, q_{vz}, r_x, r_y, r_z\}$ , as shown in Equation 4.9. This represents a fully anisotropic weighting for both the state and control matrices. Each component of the position and velocity state error is penalized individually through the weights  $q_x, q_y, q_z$  and  $q_{vx}, q_{vy}, q_{vz}$ , respectively. The control weighting matrix  $R$  remains the same as in the five-variable case, penalizing control effort along each axis independently.

$$Q = \begin{bmatrix} q_x & 0 & 0 & 0 & 0 & 0 \\ 0 & q_y & 0 & 0 & 0 & 0 \\ 0 & 0 & q_z & 0 & 0 & 0 \\ 0 & 0 & 0 & q_{vx} & 0 & 0 \\ 0 & 0 & 0 & 0 & q_{vy} & 0 \\ 0 & 0 & 0 & 0 & 0 & q_{vz} \end{bmatrix} \quad R = \begin{bmatrix} r_x & 0 & 0 \\ 0 & r_y & 0 \\ 0 & 0 & r_z \end{bmatrix} \quad (4.9)$$

This progressive breakdown of the weighting matrices allowed for a systematic analysis of the impact of each set of decision variables on the optimization results. The different configurations are summarized in Table 4.5.

TABLE 4.5 – Summary of decision variable sets for LQR optimization.

Number of Decision Variables	Decision Variables
2	$q, r$
3	$q_x, q_v, r$
5	$q_x, q_v, r_x, r_y, r_z$
9	$q_x, q_y, q_z, q_{vx}, q_{vy}, q_{vz}, r_x, r_y, r_z$

For the PID controller, P, PI, and PID controllers were progressively used, representing 3, 6, and 9 decision variables, respectively, as detailed in Table 4.6. This approach was adopted to validate the results previously obtained from the polynomial analysis of the

poles in the frequency domain.

TABLE 4.6 – Summary of decision variable sets for PID controller optimization.

Number of Variables	Controller Type	Decision Variables (Gains)
3	P	$K_{px}, K_{py}, K_{pz}$
6	PI	$K_{px}, K_{py}, K_{pz}, K_{ix}, K_{iy}, K_{iz}$
9	PID	$K_{px}, K_{py}, K_{pz}, K_{ix}, K_{iy}, K_{iz}, K_{dx}, K_{dy}, K_{dz}$

Considering the formulation of the numerical simulations, test scenarios, and the definition of the optimization problems, the validity of the results is grounded on the following assumptions, which define the scope of this study:

- The relative orbital elements ensure near-circular, close proximity orbits that comply with the linear perturbed dynamics model.
- The propulsion system can provide thrust rapidly without the need to consider delays.
- The navigation and guidance model of relative motion remains robust against orbital perturbations and state noise.
- The objective functions accurately represent the desired characteristics of the orbit control design.
- The optimization algorithms will converge to feasible solutions within the defined constraints, provided such solutions exist.
- The Pareto non-dominated frontier will contain suitable solutions for orbit control.

## 4.5 Statistical Analysis

Following the simulation framework detailed in the previous section, a series of independent computational experiments were conducted. The primary objective of these experiments was to identify the most effective optimization strategy for tuning the gains of the proposed satellite controllers. This involved statistically assessing the quality of solutions produced by various optimization approaches (Rardin; Uzsoy, 2001), evaluating single- and multiobjective optimization across various metaheuristic algorithms. Given that heuristic optimization algorithms, often employed for such complex tuning tasks, can inherently exhibit variability in their outcomes, particularly when applied to diverse problem instances conducting multiple independent runs is essential. For the purpose of

reproducibility and ensuring fair comparisons when specific random elements are part of the experimental setup (e.g., initial population generation in an evolutionary algorithm), fixing the random seed within the chosen software environment for each specific run or block of runs is a critical procedural step (Rardin; Uzsoy, 2001).

The number of independent experimental runs for each optimization strategy was initially planned based on sampling theory principles. This approach aims to ensure that statistical inferences regarding algorithm performance meet a desired level of confidence, allowing for robust conclusions about the superiority of one strategy over another, rather than attributing differences merely to random chance (Auger; Hansen, 2005). However, in instances where optimization runs consistently diverged or failed to produce viable solutions, these were considered indicative of the strategy's unsuitability or instability under those specific conditions. Such cases, where convergence to a meaningful solution was not achieved, were marked as critical performance outcomes themselves, and their exclusion from certain statistical analyses focused on the quality of converged solutions was necessary (Auger; Hansen, 2005), as divergence itself constitutes a significant finding. The data collected from successful experimental runs for final controller performance metrics (relative position accuracy, settling time, and control usage) and optimization process metrics (convergence speed, computational effort, and the overall variance of the obtained solutions) form the basis for the subsequent statistical comparisons.

Given the varied structures and operational mechanics of the optimization algorithms evaluated, ranging from evolutionary methods to algorithms inspired by physical phenomena, normalizing computational effort is crucial for fair comparison. Therefore, performance was primarily assessed based on a limited number of fitness function evaluations (Rardin; Uzsoy, 2001), rather than metrics like the number of populations or generations, which can be inconsistent across different algorithmic frameworks. Fitness function evaluations provide a more universal measure of the computational resources consumed, particularly when algorithm complexities differ significantly (Rardin; Uzsoy, 2001). Since the computational and time budget is a significant constraint for the potential operational applications of this study (akin to planning or control problem contexts), the number of evaluations was restricted to approximately 1,000 per optimization run. This decision leverages the characteristic of many heuristic optimization methods to achieve rapid convergence to reasonably good, if not strictly optimal, solutions, which is often sufficient for practical engineering applications.

Furthermore, a critical aspect of evaluating these optimization strategies is the distinction between **statistical significance** and **practical significance**. Statistical methods, such as the Analysis of Variance (ANOVA), can determine if observed performance differences between strategies are unlikely to be the result of random chance. However, such a finding does not independently establish the engineering superiority of a given strategy.

---

An improvement that is statistically significant may be practically irrelevant if its magnitude is insufficient to meaningfully affect the satellite's operational objectives. Likewise, a statistically validated improvement may be discounted if it incurs a disproportionate computational cost or if the resulting controller lacks robustness. A robust controller must demonstrate resilience against variations in operating conditions and unmodeled system dynamics. Robustness analysis therefore entails evaluating performance variance across perturbed test conditions and assessing the sensitivity of the optimized parameters to such variations.

## 5 Numerical Results and Discussion

This section presents the main results of the research which are divided into four main parts: the first focuses on the geometry-independency hypothesis. The second part focuses on the control results obtained with the LQR controller based on the literature and then the resulting weighting matrices yielded from the optimization process. Meanwhile the third part delves into the PID controller, starting with the classical control approach and then exploring the optimized gains. Finally, the fourth part provides a comparative analysis of the performance metrics of the different control strategies.

Before presenting the final control performance metrics, it is essential to first characterize the optimization problem itself. The core of the methodology relies on navigating a complex search space to find optimal controller gains with proper decision variables bounds. Figure 5.1 visualizes this search space, commonly referred to as a fitness landscape, which must be effectively handled by the optimization algorithms.

In this visualization, the axes represent the decision variables, while the color map indicates the value of the error objective function (ITAE). The landscape is characterized by local minima regions and a global minimum corresponding to the optimal solution. Its complexity, ruggedness, and multimodality emphasize the difficulty of the optimization task, as algorithms must navigate this space efficiently to identify the global optimum without becoming trapped in suboptimal regions. The crosses and the red dot denote the best solutions found during optimization, with the red dot highlighting the overall best solution across all groups.

Figure 5.1 represents the optimization results for the TanDEM-X geometry tracking the unperturbed reference, using the two decision variable structure described in Table 4.5.

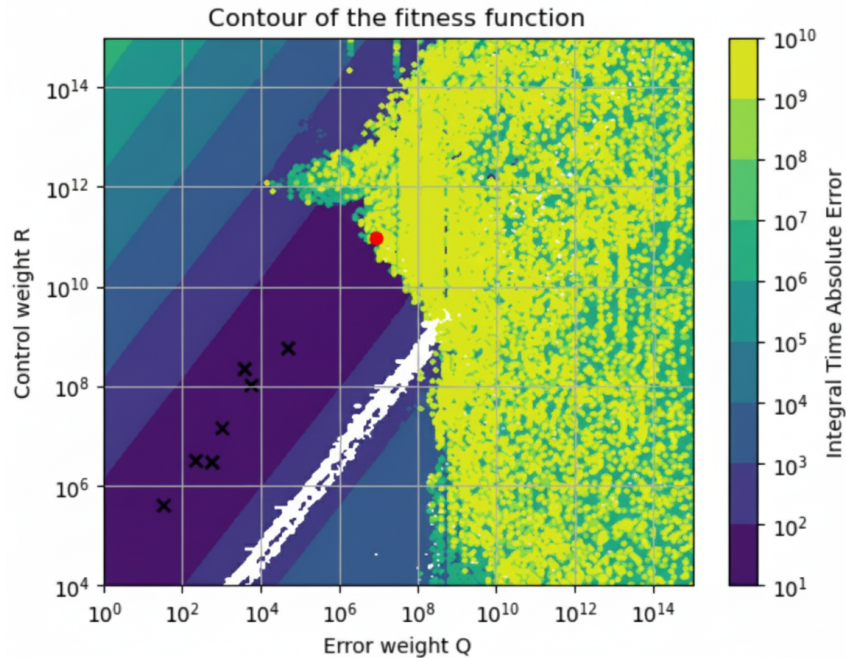


FIGURE 5.1 – Representation of the fitness function landscape for an optimization problem with 2 decision variables. The horizontal and vertical axes represent controller decision variables, while the color map shows the objective function value to be minimized. The crosses indicate the best solutions found for each group, and the red dot indicates the overall best solution.

Although this is a simplified fitness landscape, it enables an understanding of the optimization problem and gives us insights into the possible bounds of the optimization. Thus, the bounds for the optimization variables for the weight matrices of the LQR controller shown in Table 4.4 were derived from Figure 5.1, aiming for numerically stable regions of the optimization.

In practice, the optimization problem incorporates up to nine decision variables, which constitutes a high-dimensional search space. The white regions within this space denote parameter combinations that yield numerically unstable solutions to the algebraic Riccati equation. Concurrently, the yellow regions identify parameter sets that result in either divergent control gains or errors exceeding the predefined convergence timeout threshold.

## 5.1 Geometry-Independence Hypothesis

When comparing the results yielded by the optimization, it is hypothesized that the optimal combinations of algorithms, strategy, and decision variables will be maintained regardless of the specific formation flying geometry for a given simulation scenario, as the search space is expected to retain a similar level of complexity.

Figures 5.2 and 5.3 present the results using the same controller, guidance reference, and optimization strategy, consistent with those presented in Figure 4.1. The objective

is to verify whether the performance of the optimization algorithms remains consistent across the different formation geometries.

The subsequent plots illustrate the comparative performance of various optimization algorithms. The x-axis represents the different optimization algorithms tested. The data is further categorized according to the number of decision variables used for the LQR controller, as further detailed in Section 4.4. The y-axis indicates the mean value of the objective function, which corresponds to the daily control usage (daily  $\Delta V$ ), averaged over  $n = 10$  independent runs. In this analysis, a lower objective function value signifies superior optimization algorithm performance and greater efficiency in formation-keeping control usage.

The thickness of each bar visualizes the result variability by representing the 95% confidence interval range. For clarity, only combinations of algorithms and decision variables that produced feasible results across all  $n$  independent runs are presented. Therefore, not all possible categories may be displayed in the figures.

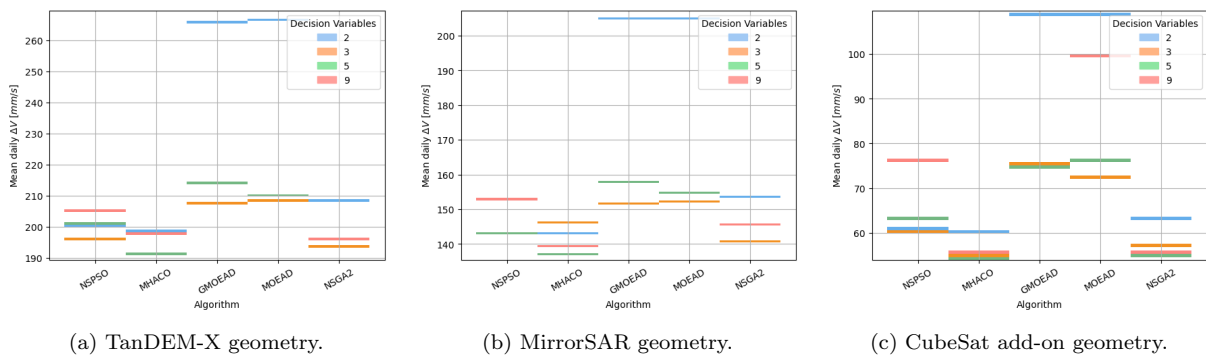


FIGURE 5.2 – Comparison of the mean values of the objective function estimation for each algorithm in the multiobjective optimization of the LQR controller across different formation geometries. The y-axis represents the average estimated value of the objective function, which is the daily control usage  $\Delta V$ . The x-axis lists the optimization algorithms used.

Observing the performance under a multiobjective strategy, the same performance trend is noted for the optimization algorithms across the different formation geometries. The best results are consistently achieved by the same algorithms and numbers of decision variables, regardless of the specific formation geometry. This suggests that the complexity of the search space remains relatively constant across the different geometric configurations, allowing the algorithms to maintain their efficacy. For all geometries, the MHACO and NSPSO algorithms stand out, especially with a smaller number of decision variables (three and five), indicating that these methods are particularly effective at exploring the solution space under these conditions.

The variation in the y-axis range across the figures is attributed to the different initial conditions of the formation geometry, as detailed in Table 4.2. The larger separations in the TDX geometry lead to higher control usage, while the smaller separations in the

CubeSat add-on geometry result in lower control usage. This aligns with the expected system behavior, as maintaining formation over greater distances typically requires more propellant, as the required changes in absolute velocity are more pronounced for larger separations.

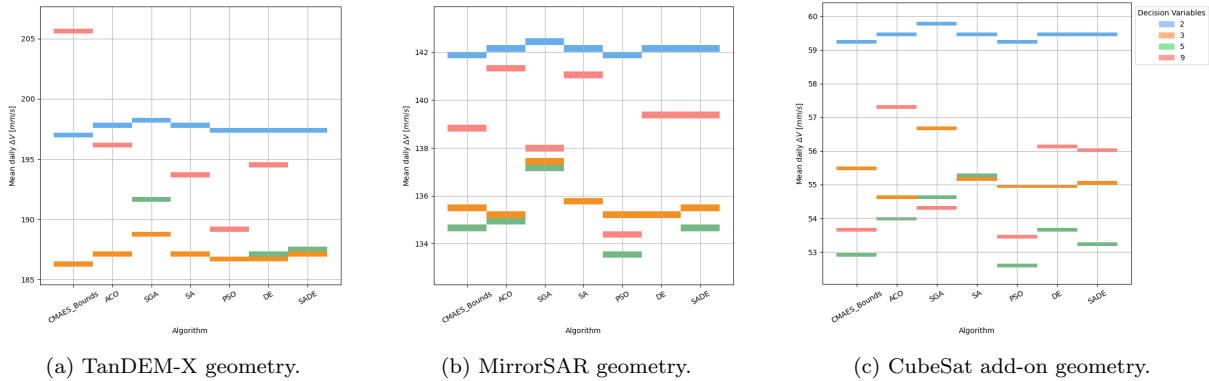


FIGURE 5.3 – Comparison of the mean values of the objective function estimation for each algorithm in the single objective optimization of the LQR controller across different formation geometries. The y-axis represents the average estimated value of the objective function, which is the daily control usage  $\Delta V$ . The x-axis lists the optimization algorithms used.

From a qualitative analysis, the results profile for the single objective case remains consistent across the different formations. For all geometries, the results for two decision variables exhibit a performance plateau at a suboptimal level, suggesting that this limitation restricts the ability of the optimization algorithms to effectively explore the solution space. In contrast, configurations with three and five decision variables consistently produce the best results, indicating that this level of complexity is adequate to capture the nuances of the control problem without overburdening the optimization process. Furthermore, the CMAES and PSO algorithms particularly stand out in scenarios where the algorithms yield more heterogeneous results.

Conversely, the results using nine decision variables show high variance. This can be attributed to exploration dynamics that may hinder algorithmic convergence within the available optimization budget, rendering the comparison for this configuration less reliable.

This indicates that the choice of formation geometry does not significantly impact the performance of the optimization algorithms in this context, allowing for a more straightforward comparison of the algorithms' effectiveness across different scenarios. Furthermore, it enables us to analyze and compare the optimization strategies focusing on only one geometry for simplicity.

Since the unperturbed reference trajectory demands greater control effort to maintain the formation, optimization results for this trajectory generally exhibit higher control usage compared to the perturbed one. Consequently, the controller's response is generally

more complex, and the optimization search space is more challenging. Therefore, the controller's time-domain response to an initial error is more informative for assessing the types of solutions the optimization method can achieve. Thus, the time-domain responses for the best solutions are presented in the following sections, evaluated in terms of state error and control usage.

## 5.2 Linear Quadratic Regulator (LQR)

In this section, the simulation and optimization of the LQR controller will be presented, focusing on the definition of its weighting matrices  $Q$  and  $R$ . The LQR controller showed an easier optimization process, since the extra layer of abstraction provided by these matrices and the algebraic Riccati equation allowed the optimization algorithms to explore a more manageable search space. This is particularly true when compared to the PID controller, which directly optimizes the controller gains. The analysis will present the results from the single objective and multiobjective optimizations, which will be analyzed and compared against a reference case study from the literature.

### 5.2.1 Reference Study Case

Due to the coupled, multiple-input multiple-output (MIMO) nature of the complete dynamical system, classical control methodologies are not extensively covered in the literature. Nevertheless, some guidelines for selecting the weighting matrices  $Q$  and  $R$  are available. One of the literature suggestions (Alfriend *et al.*, 2010) is a diagonal structure wherein the control weighting matrix  $R$  is defined with diagonal entries of  $n_0^{-4}$  and the state weighting matrix  $Q$  is also diagonal with unit weights for position errors and weights of  $n_0^{-2}$  for rate errors along each axis, as shown in Equation 5.1.

$$Q = \begin{bmatrix} 1 & 0 & 0 & 0 & 0 & 0 \\ 0 & 1 & 0 & 0 & 0 & 0 \\ 0 & 0 & 1 & 0 & 0 & 0 \\ 0 & 0 & 0 & n_0^{-2} & 0 & 0 \\ 0 & 0 & 0 & 0 & n_0^{-2} & 0 \\ 0 & 0 & 0 & 0 & 0 & n_0^{-2} \end{bmatrix} \quad R = \begin{bmatrix} n_0^{-4} & 0 & 0 \\ 0 & n_0^{-4} & 0 \\ 0 & 0 & n_0^{-4} \end{bmatrix} \quad (5.1)$$

This configuration yields a stable performance, with a converging control, but it is not optimal in terms of state error as illustrated in Figure 5.4. The state error demonstrates a stable behavior but does not converge to zero. This solution results in a lower mean control usage of 181 mm/s per day for the TDX formation geometry tracking the unperturbed

reference trajectory, but the steady-state error behavior indicates potential divergence if the others perturbations and error sources, such as sensor dynamics, are added into the simulation.

Figure 5.4 presents the time-domain response of the LQR controller, showing both state error evolution and control usage. The state error plot focuses on two key metrics: the effective baseline ( $B_{\perp}$ ) error and the along-track error. The  $B_{\perp}$  error, a linear combination of radial and cross-track errors, is crucial for evaluating formation keeping performance as it directly relates to interferometric measurement quality (Moreira *et al.*, 2013; Krieger *et al.*, 2007) as previously shown in Figure 3.2. The along-track error is also included as it indicates the main axis along which potential drift and eventual formation disruption can occur. Additionally, the figure displays the control usage, outlining the acceleration profile over time and indicating the saturation mark defined in Section 4.3.

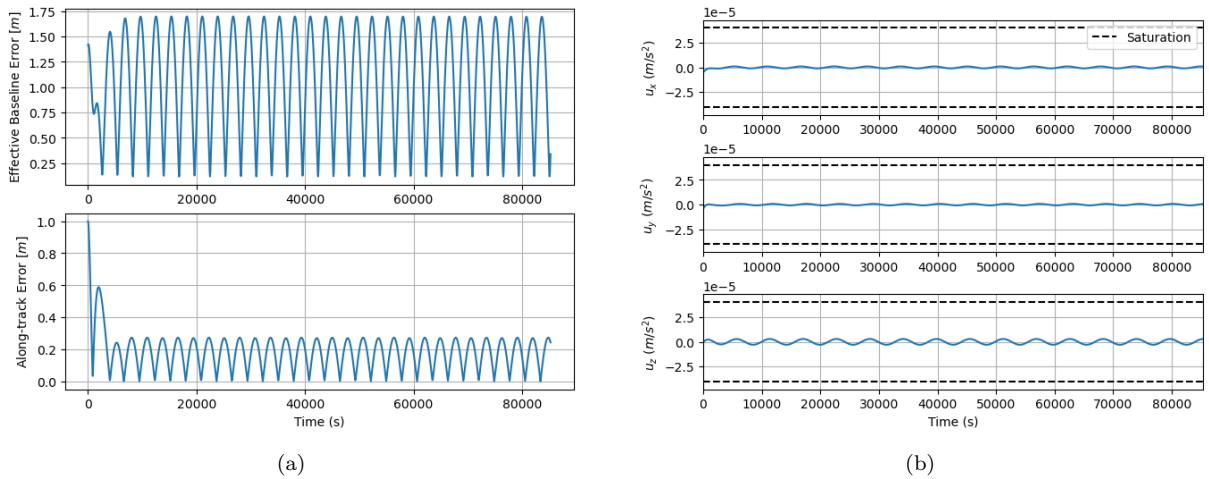


FIGURE 5.4 – Simulation of LQR controller with the literature-suggested weighting matrices using the unperturbed reference formation. (a) State error evolution; (b) Control acceleration profile.

An alternative is to modify this literature suggested weighting matrices where  $R$  is still defined with diagonal entries of  $n_0^{-4}$  and  $Q$  is completely define as a diagonal state weighting matrix with entries  $n_0^{-1}$ , as shown in Equation 5.2.

$$Q = \begin{bmatrix} n_0^{-1} & 0 & 0 & 0 & 0 & 0 \\ 0 & n_0^{-1} & 0 & 0 & 0 & 0 \\ 0 & 0 & n_0^{-1} & 0 & 0 & 0 \\ 0 & 0 & 0 & n_0^{-1} & 0 & 0 \\ 0 & 0 & 0 & 0 & n_0^{-1} & 0 \\ 0 & 0 & 0 & 0 & 0 & n_0^{-1} \end{bmatrix} \quad R = \begin{bmatrix} n_0^{-4} & 0 & 0 \\ 0 & n_0^{-4} & 0 \\ 0 & 0 & n_0^{-4} \end{bmatrix} \quad (5.2)$$

This configuration is shown in Figure 5.5 and yields a converging state error, but with a higher mean control usage of 198 mm/s per day for the TDX formation geometry tracking

the unperturbed reference trajectory. This indicates that while the state error converges to zero, it does so at the cost of increased control usage, highlighting the trade-off between accuracy and efficiency in controller design.

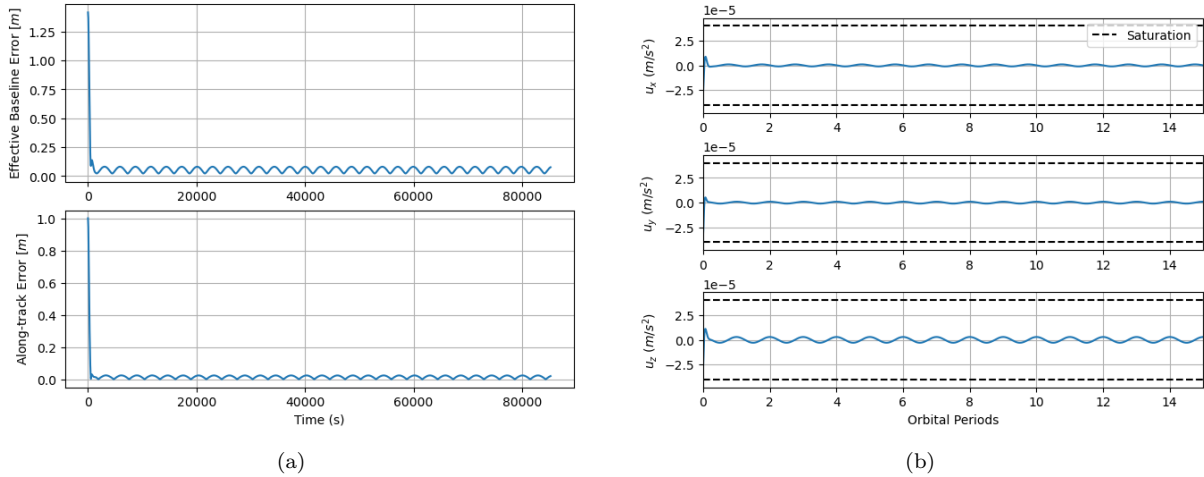


FIGURE 5.5 – Simulation of LQR controller with the literature inspired weighting matrices using the unperturbed reference formation. (a) State error evolution; (b) Control acceleration profile.

## 5.2.2 Single Objective Optimization

Figures 5.6 and 5.7 present the results of the single objective optimization of the LQR controller applied to the TDX formation geometry. Specifically, Figure 5.6 illustrates the controller’s performance when tracking the unperturbed reference trajectory, actively compensating for orbital perturbation effects. In contrast, Figure 5.7 shows the results for the perturbed reference trajectory, in which the controller allows the secular drift induced by orbital perturbations.

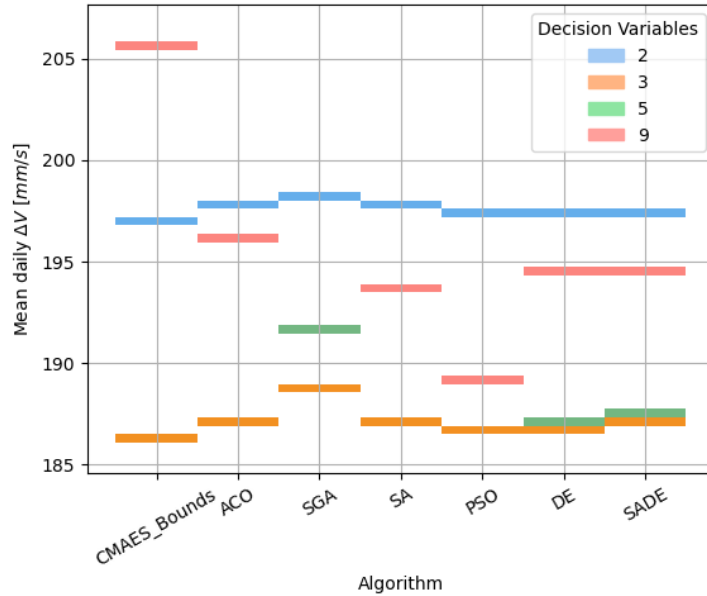


FIGURE 5.6 – Mean estimation of the single objective optimization of the LQR controller for the TDX geometry tracking the unperturbed reference trajectory.

Given the increased difficulty in compensating for orbital perturbations, the limited optimization budget, approximately one thousand evaluations of the objective function, led to the best solutions emerging with a lower number of decision variables (three and five), as this reduces the available search space. These configurations still yielded favorable results in terms of control usage. This suggests that the optimization algorithms were effective in solving the single objective optimization problem for the LQR controller, even when the degrees of freedom in the weighting matrices were restricted.

Comparing the optimization algorithms, the solutions obtained with three decision variables were similar across all methods. Nonetheless, CMAES and PSO stood out, exhibiting the best average performance. Since both are population-based methods, as depicted in Figure 3.13, they offer a greater diversity of candidate solutions and are better at avoiding premature convergence to local minima. Furthermore, these algorithms possess mechanisms that are often computationally more efficient (Wang; Tan; Liu, 2017; Hansen, 2006), requiring fewer steps, intermediate calculations, and hyperparameters to tune and determine the next generation (offspring) (Wang; Tan; Liu, 2017; Hansen, 2006). Conversely, we observe the poorest performance from SA. This can be attributed to the fact that SA, being a direct search strategy that only uses the objective function value, lacks the abstraction or encoding mechanisms (Corana *et al.*, 1989) to effectively explore a complex and noisy search space, thereby being less resilient to such environments.

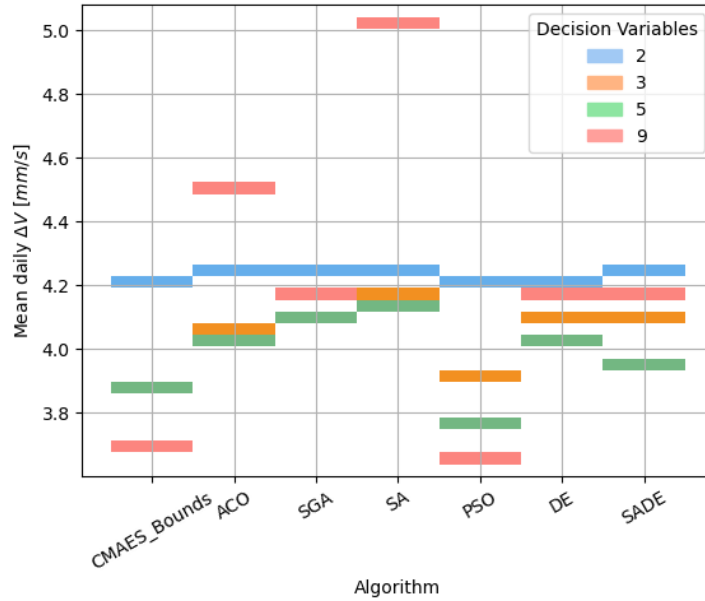


FIGURE 5.7 – Mean estimation of the single objective optimization of the LQR controller for the TDX geometry tracking the perturbed reference trajectory.

Since this reference trajectory is intended only to correct the initial errors in the FF, the control task becomes simpler, which in turn reduces the complexity of the optimizer’s search space. As a result, algorithms with a higher number of decision variables (five and nine) are able to find better solutions within the same optimization budget, the same number of objective function evaluations. The increased degrees of freedom in defining the weighting matrices  $Q$  and  $R$  are therefore more effectively leveraged in this scenario.

Therefore, similar to the previous case in Figure 5.10, among the algorithms, it is noted that the same computational efficiency properties (Wang; Tan; Liu, 2017; Hansen, 2006) stand out for better exploration of the search space, with CMAES and PSO presenting the best average performances.

In this case, the temporal response of the single objective optimized LQR controller is presented in Figure 5.8. The optimized response demonstrates superior overall quality, featuring a smoother and more damped transient response. Additionally, the steady-state regime exhibits a very low residual error, on the order of millimeters, which is consistent with the expected performance of an optimal controller in a dynamic system devoid of the irregularities introduced by physical sensors and actuators (Chiha; Liouane; Borne, 2012; Thamir, 2020).

It is worth noting the accommodation time of approximately one orbital period, which is a reasonable timeframe for formation-keeping maneuvers in low Earth orbit scenarios (Kahle *et al.*, 2012). Furthermore, unlike the responses shown in Figures 5.4 and 5.5, there is an absence of visible small oscillations caused by the remaining unmodeled orbital perturbations.

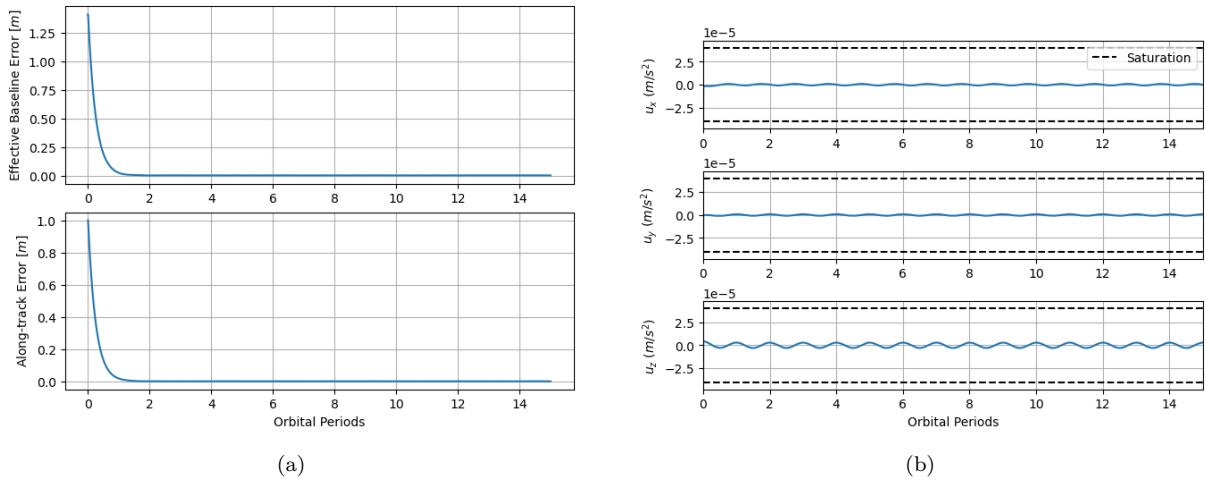


FIGURE 5.8 – Simulation of LQR controller with the single objective optimized weighting matrices using the unperturbed reference formation. (a) State error evolution; (b) Control acceleration profile.

Furthermore, for the perturbed reference trajectory, which already exhibits simpler convergence and a reduced cost, an additional optimization was performed by constraining the radial control component  $u_x$  to be zero. The results, presented in Figure 5.9, indicate that the absence of radial control does not significantly degrade the system’s performance (Alfriend *et al.*, 2010), while maintaining control usage levels comparable to those achieved with the fully actuated controller. This finding suggests that the radial control may be considered dispensable for this particular trajectory, potentially simplifying the controller design without sacrificing operational efficiency.

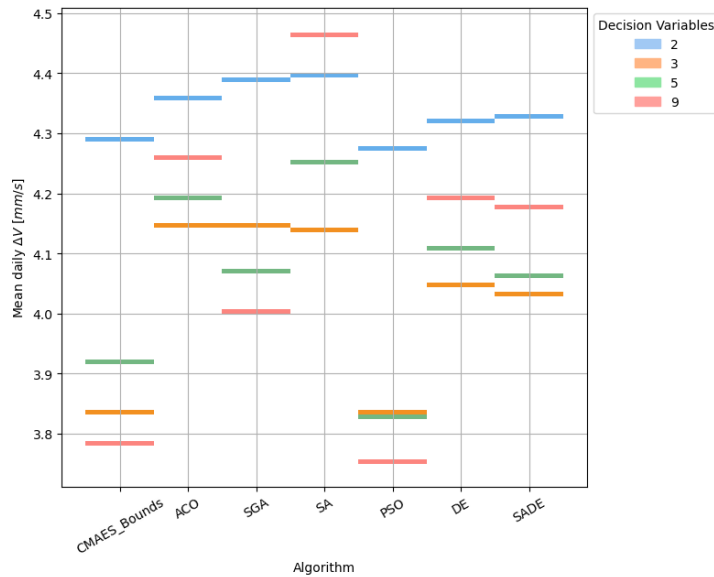


FIGURE 5.9 – Mean estimation of the single objective optimization of the LQR controller for the TDX geometry tracking the perturbed reference trajectory without radial thrust.

### 5.2.3 Multiobjective Optimization

Figure 5.10 presents the results of the multiobjective optimization of the LQR controller for the TDX geometry. Specifically, Figure 5.10 shows the performance when tracking the unperturbed reference trajectory.

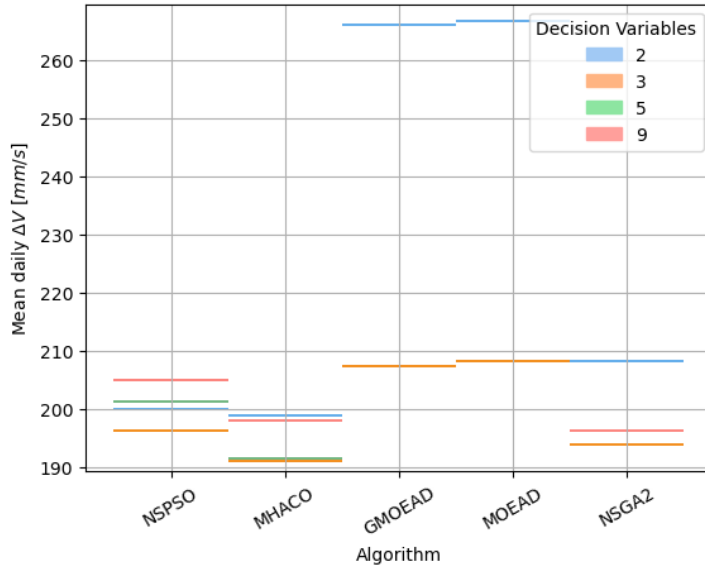


FIGURE 5.10 – Mean estimation of the multiobjective optimization of the LQR controller for the TDX geometry tracking the unperturbed reference trajectory.

Similar to the single objective constrained case, the best optimization results for the unperturbed reference trajectory are obtained with a lower number of decision variables (three and five). When delving into the optimization algorithms, there is a consistently poor performance from MOEAD and GMOEAD across all decision variables. This can be attributed to their core mechanics. These algorithms rely on localized search through information exchange between neighboring subproblems (Zhang; Li, 2008), a method designed to generate an evenly distributed Pareto front approximation (Zhang; Li, 2008). However, this characteristic may limit their exploration capabilities in highly complex and multimodal search spaces, such as the one presented in this optimization problem (Zhang; Li, 2008). This limitation can lead to premature convergence to suboptimal solutions and a Pareto front that does not fully capture the trade-offs and scale between the objectives.

In contrast, algorithms like NSGA2 operate on a different principle. Selection is performed using a fast nondominated sorting approach, which ranks solutions into hierarchical fronts (Deb *et al.*, 2002). To maintain diversity and prevent premature convergence, it utilizes a crowding-comparison operator, which assesses solution density by calculating the average distance to neighboring solutions along each objective, preferring individuals located in less crowded regions (Deb *et al.*, 2002). This global diversity management, rather than a localized neighborhood search, allows for more effective exploration of the

search space. Similarly, the MHACO algorithm demonstrates a robust approach by integrating nondominated sorting with the hypervolume metric (Acciarini; Izzo; Mooij, 2020). It ranks solutions using a “hypervolume-comparison operator”. This operator prioritizes solutions based on their nondomination rank, for solutions on the same front (Acciarini; Izzo; Mooij, 2020). The population evolves using a solution archive that stores the best individuals, providing a different and more global evolutionary dynamic than the fixed-neighbor structure of MOEAD.

The control response with the optimized gains is similar to the one presented in Figure 5.11, with a smooth transient response and a very low steady-state error also on the order of millimeters.

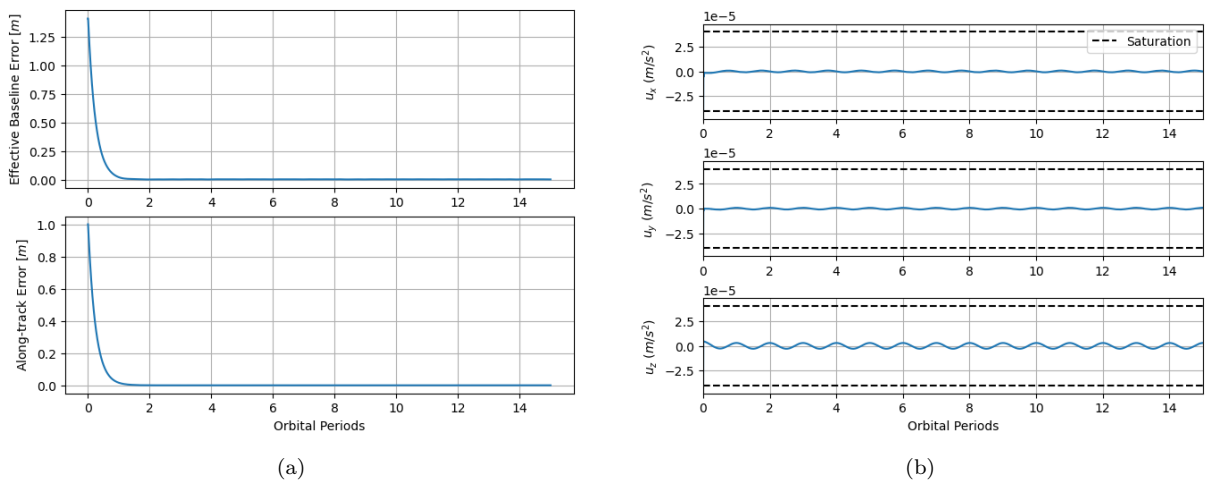


FIGURE 5.11 – Simulation of LQR controller with the multiobjective optimized weighting matrices using the unperturbed reference formation. (a) State error evolution; (b) Control acceleration profile.

Meanwhile, Figure 5.12 presents the results for the perturbed reference trajectory, where the control task is simpler, the best solutions are achieved with a higher number of decision variables (five and nine).

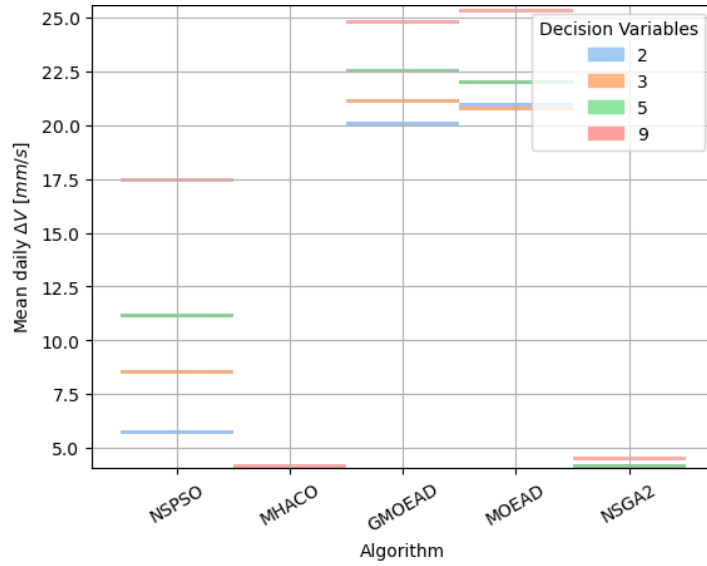


FIGURE 5.12 – Mean estimation of the multiobjective optimization of the LQR controller for the TDX geometry tracking the perturbed reference trajectory.

Similarly, multiobjective optimization was conducted for the case where the radial control  $u_x$  is constrained to zero. The results, presented in Figure 5.13, show that the absence of radial control does not significantly degrade system performance (Alfriend *et al.*, 2010), maintaining control usage levels comparable to those achieved with the fully actuated controller.

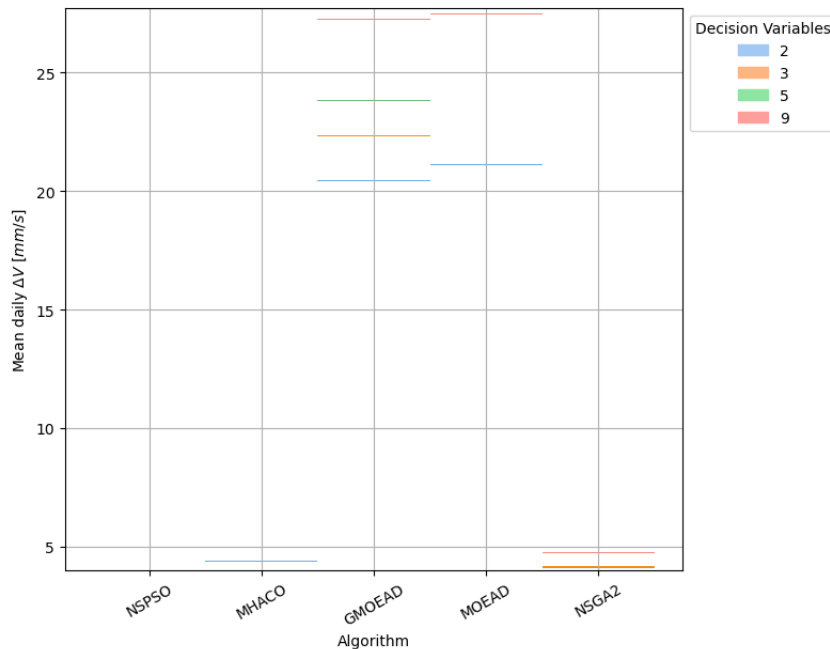


FIGURE 5.13 – Mean estimation of the multiobjective optimization of the LQR controller for the TDX geometry tracking the perturbed reference trajectory without radial thrust.

Graphically, it is noteworthy that the NSPSO was unable to find a feasible solution. Although the extreme points are similar to those presented in Figure 5.12, the traces

are thinner, indicating lower variance in the results. This also suggests that the absence of radial control can reduce the search space, thereby facilitating the convergence of the optimization algorithms.

Despite differences in the resulting values, the multiobjective optimization outcomes exhibit a similar trend to those of the single objective optimization, particularly when observing the best-performing algorithms and decision variables under comparable LQR controller conditions. This indicates that multiobjective strategies effectively explore the search space to identify viable and efficient solutions for the LQR controller, even with an increased number of decision variables.

### 5.3 Proportional-Integral-Derivative (PID) Control

The initial stability analysis in Section 4.2, conducted using classical control theory, evaluated the performance of various control architectures and determined that the PID controller is the most effective approach. The results showed that the closed-loop system is unstable under both P and PI control, and while the PD controller can achieve stability, it is unable to eliminate the steady-state error. This section details the design and tuning process for this PID architecture. First, classical tuning methods, namely Ziegler-Nichols and Root Locus analysis, are used to establish a baseline configuration and analyze system stability. Following this, computational optimization techniques are applied, beginning with a single objective formulation and concluding with a multiobjective optimization framework to find optimal controller gains.

It must be noted, however, that due to the nonlinear dynamics and inherent perturbations present in spacecraft formation flying, these classical methods are insufficient to guarantee stability across all operational conditions. Nevertheless, they serve as a valuable starting point for assessing controller viability and provide a foundation for the design process.

#### 5.3.1 Ziegler-Nichols Tuning and Root Locus Analysis

Systematic methods can be employed to provide a starting point for tuning the PID controller gains. The Ziegler-Nichols tuning rules and Root Locus analysis are two classical approaches that offer insight into the system's stability and response characteristics as a function of the controller parameters (Ogata, 2010).

The second Ziegler-Nichols method bases its tuning on the critical gain ( $K_{cr}$ ) and the critical period ( $P_{cr}$ ), which is the period of sustained oscillation at the stability limit under proportional-only control (Ogata, 2010). Since the plant is inherently oscillatory,

this method is not directly applicable in its standard form. However, the critical period, in this case the orbit period, can be used to establish the integral and derivative times according to the Ziegler-Nichols rules:

$$T_i = 0.5P_{cr} \quad (5.3)$$

$$T_d = 0.125P_{cr} \quad (5.4)$$

This approach provides a systematic starting point for tuning the controller. Subsequently, a root locus can be sketched to visualize the effect of varying the proportional gain ( $K_p$ ) on the closed-loop pole locations. Figure 5.14 illustrates the root locus for the Z-axis PID control system.

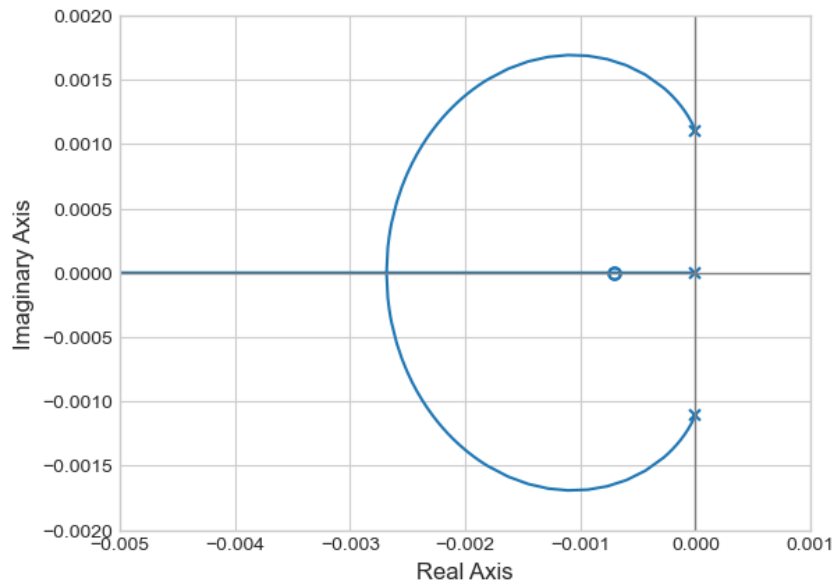


FIGURE 5.14 – Root locus of the closed-loop system with a PID controller for the Z-axis, showing the effect of varying the proportional gain ( $K_p$ ) on the pole locations.

Figure 5.14 displays the trajectories of the closed-loop poles in the complex plane as  $K_p$  varies, providing insight into the system's stability and transient response. In this case, the poles remain in the left half-plane for all positive values of  $K_p$ , indicating that the system is stable across the entire range of positive proportional gain.

Analogously, this analysis can be extended to the coupled X and Y axes. To remain within the scope of the presented mathematical framework, it is assumed for simplicity that the controller maintains the same ratio between proportional, integral, and derivative gains. Figure 5.15 shows the root locus for the closed-loop system with a PID controller for the in-plane motion.

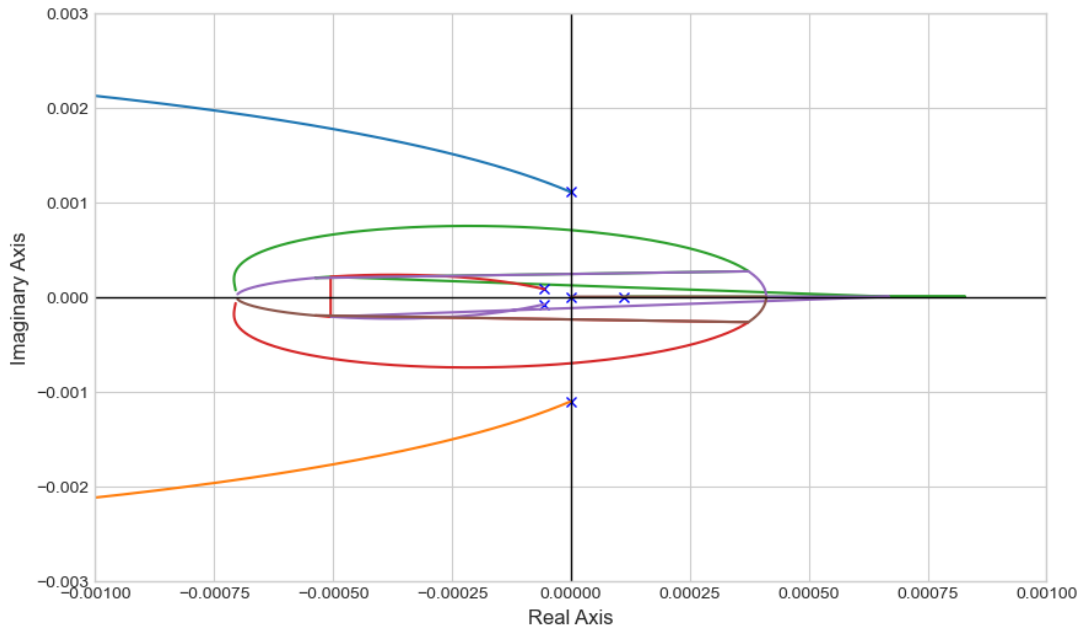


FIGURE 5.15 – Root locus of the closed-loop system with a PID controller for the X and Y axes, showing the effect of varying the proportional gain ( $K_p$ ) on the pole locations.

For the X and Y axes, it is noted that the closed-loop poles do not remain in the left half-plane for all positive values of  $K_p$ . This indicates that the system is initially unstable but can be stabilized for a specific range of the proportional gain, thus demonstrating conditional stability. Combining both analyses, it is evident that a PID controller can be tuned to stabilize the complete system, provided that the gains for the X and Y axes are selected from the stable region identified in Figure 5.15, while the gains for the Z-axis are derived from Figure 5.14.

For the simplified system, which does not model nonlinearities and perturbations, the Ziegler-Nichols tuning method provided a reasonably stable response, as shown in Figure 5.16. However, the transient response is highly oscillatory, and the steady-state error is significant, on the order of several meters. This indicates that while the Ziegler-Nichols method offers a systematic approach, it is far from optimal for this application.

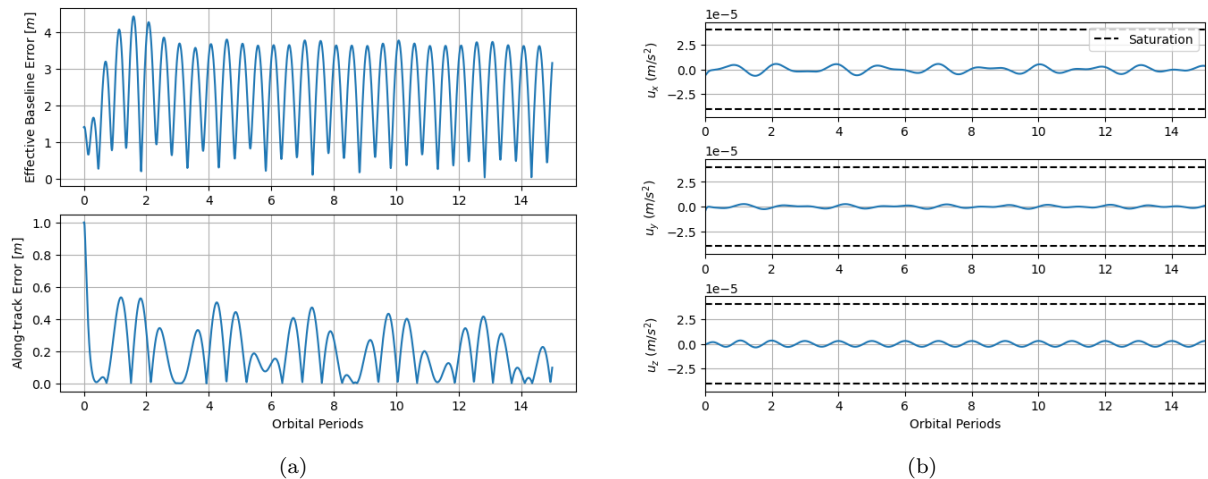


FIGURE 5.16 – Simulation of the PID controller with the literature (Ogata, 2010) inspired Ziegler-Nichols method using the unperturbed reference formation. (a) State error evolution; (b) Control acceleration profile.

It is worth noting that several assumptions are required to constrain the root locus construction to a single variable, which, although systematic, imposes significant limitations on the available solution space. Therefore, further optimization of the PID gains is necessary to enhance performance.

### 5.3.2 Single Objective Optimization

None of the optimization algorithms were able to find a solution for the single-objective optimization of the PID controller. This is likely due to the limitations of the constrained single-objective formulation, which requires the optimizer to identify viable solutions that satisfy the given error constraints. This challenge is amplified by the high dimensionality of the search space when considering the full PID configuration with nine decision variables.

Since stable and convergent PID gains are unlikely to be present in the initial random population, the algorithms struggle to generate a feasible starting point that also respects the imposed error constraint. Without such a point from which the search space can be effectively explored, all simulations conducted under this formulation were hindered from the very first generation.

### 5.3.3 Multiobjective Optimization

Figure 5.17 presents the results of the multiobjective optimization of the PID controller for the TDX geometry when tracking the unperturbed reference trajectory. The results indicate that the optimization algorithms were able to find a solution for this case, demonstrating the effectiveness of the multiobjective optimization strategies for the PID

controller in this context.

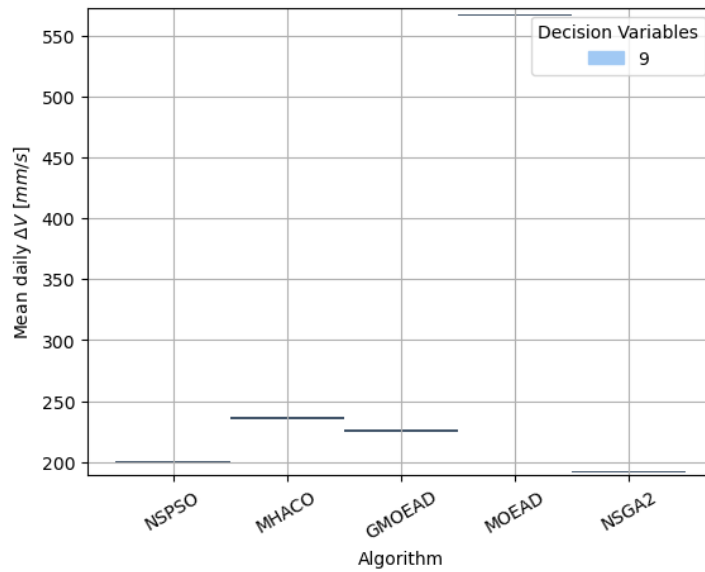


FIGURE 5.17 – Mean estimation of the single objective optimization of the PID controller for the TDX geometry tracking the unperturbed reference trajectory.

For the PID controller, the number of decision variables depends on the selected configuration, whether P, PI, PD, or full PID. The optimization results indicate that the full PID configuration, comprising nine decision variables, is necessary to ensure both system convergence and stability, thereby ratifying the previous analysis.

Although the single objective constrained formulation was not able to find viable solutions, the use of a multiobjective optimization framework enables the algorithms to effectively explore the search space for convergent PID controller gains and then for fuel-efficient solutions. This improved flexibility is largely due to methods such as decomposition-based approaches (Zhang; Li, 2008). Furthermore, an error threshold can be applied afterward to the resulting Pareto non-dominated frontier to select only the acceptable trade-offs.

The control response with the optimized gains for the PID is presented in Figure 5.18, with a smooth transient response and a very low steady-state error. Nonetheless, it demonstrates superior overall quality, featuring a smoother and more damped transient response.

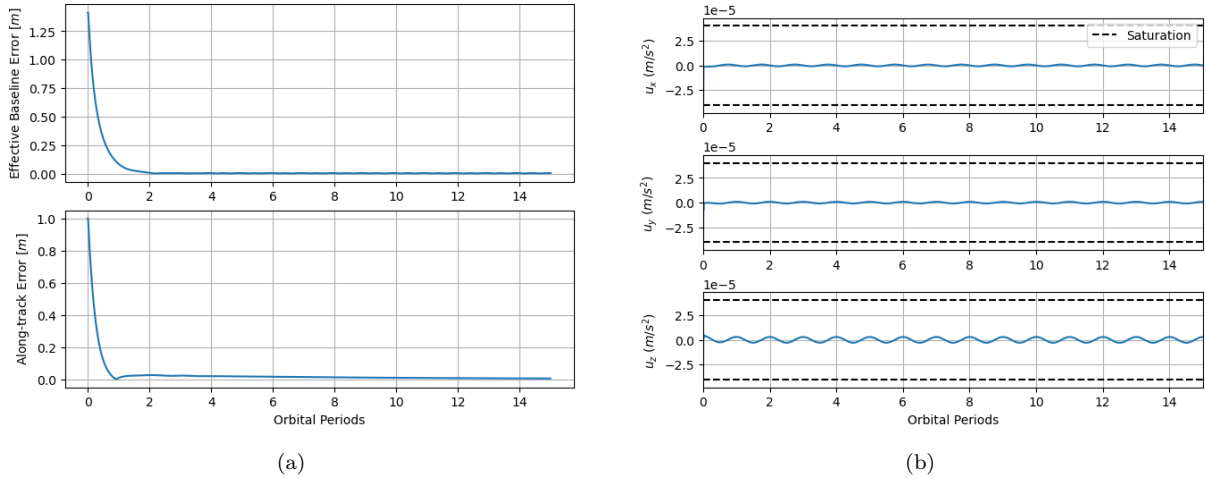


FIGURE 5.18 – Simulation of LQR controller with the multiobjective optimized weighting matrices using the unperturbed reference formation. (a) State error evolution; (b) Control acceleration profile.

## 5.4 Comparison of Optimization Strategies

A comprehensive comparison of the performance metrics for the different control strategies is presented in Tables 5.1 for the unperturbed reference and 5.2 for the perturbed reference. The results clearly demonstrate the significant advantages of the optimization-based approaches over the classical, literature-derived approaches. For the best solution of a given strategie, the respective optimization algorithm and number of decision variables are indicated in parentheses.

TABLE 5.1 – Comparison of the controllers performance tracking the unperturbed reference.

Controller	Strategie / Algorithm	ITAE [ $m^2 s^2$ ]	Steady Error [cm]	Daily $\Delta V$ [mm/s]
LQR	Reference Study Case (Alfriend <i>et al.</i> , 2010)	$2.1 \cdot 10^5$	8.4	198.1
LQR	Single Objective (PSO - 3)	$9.4 \cdot 10^3$	0.2	186.7
LQR	Multiobjective (MHACO - 3)	$1.1 \cdot 10^4$	0.3	186.9
PID	Ziegler-Nichols (Ogata, 2010)	$8.7 \cdot 10^6$	378.2	304.3
PID	Single Objective	–	–	–
PID	Multiobjective (NSGA2 - 9)	$4.6 \cdot 10^4$	1.4	186.7

For the unperturbed reference trajectory, the optimized LQR controllers achieved a remarkable reduction in both the Integral of Time-weighted Absolute Error (ITAE) and the

steady-state error when compared to the literature-based gains. The ITAE was reduced by over an order of magnitude, from  $2.1 \cdot 10^5$  to approximately  $1.1 \cdot 10^4 \text{ m}^2 \text{ s}^2$ , while the steady-state error decreased from 8.4 cm to the sub-centimeter level (0.2-0.3 cm). This substantial improvement in tracking performance was also accompanied by a significant control acceleration saving, with the daily  $\Delta V$  consumption being reduced from 198 mm/s to around 187 mm/s.

Similarly, the PID controller optimized by the multiobjective strategy showed a notable improvement over its literature-based counterpart. Although its ITAE of  $4.6 \cdot 10^4 \text{ m}^2 \text{ s}^2$  was higher than that of the optimized LQR, it represented a reduction of two orders of magnitude compared to the literature PID's ITAE of  $8.7 \cdot 10^6 \text{ m}^2 \text{ s}^2$ . The steady-state error was also drastically reduced from 378.2 cm to just 1.4 cm. Most impressively, the control usage for the multiobjective PID was 186.7 mm/s, a value comparable to the optimized LQR and a significant improvement over the 304.3 mm/s of the literature-based PID.

It is worth noting that the control laws from each controller type are fundamentally different since the PID feedback, for instance, includes the error integral, which can lead to different control effort distributions over time. This distinction validates the optimization approach for generic controller design, as it succeeded with dissimilar structures.

It is also important to note that the single objective optimization did not yield a valid solution for the PID controller. This failure highlights the efficacy of the multiobjective approach in this scenario, as previously discussed.

TABLE 5.2 – Comparison of the LQR controllers performance tracking the perturbed reference.

<b>Strategie</b>	<b>ITAE [<math>\text{m}^2 \text{ s}^2</math>]</b>	<b>Steady Error [cm]</b>	<b>Daily <math>\Delta V</math> [mm/s]</b>
Reference Study Case (Alfriend <i>et al.</i> , 2010)	$8.4 \cdot 10^2$	0.03	10.5
Single Objective (PSO - 9)	$4.5 \cdot 10^5$	3.3	3.6
Single Objective ( $u_x = 0$ ) (PSO - 9)	$8.0 \cdot 10^5$	4.7	3.7
Multiobjective (NSGA2 - 5)	$3.6 \cdot 10^3$	0.1	4.0
Multiobjective ( $u_x = 0$ ) (NSGA2 - 5)	$1.3 \cdot 10^5$	1.5	4.0

In the case of the perturbed reference trajectory represented in Table 5.2, the analysis focuses solely on the LQR controller. Here, a trade-off between tracking accuracy and control acceleration efficiency becomes evident. The literature-based approach yielded a very low ITAE ( $8.4 \cdot 10^2 \text{ m}^2 \text{ s}^2$ ) and a negligible steady-error (0.03 cm), but at a higher

control cost with a  $\Delta V$  of 10.5 mm/s. In contrast, the optimization strategies yield a better balance of steady-error and control usage efficiency. The multiobjective approach, for instance, achieved a daily  $\Delta V$  of 4.0 mm/s, which is less than half that of the literature method, while maintaining a steady-state error of only 0.1 cm. The single objective strategies resulted in even lower control usage (3.6 - 3.7 mm/s) but with a significant increase in ITAE and steady-state error.

The constrained optimization cases, where radial thrust ( $u_x = 0$ ) was disallowed, demonstrated that formation control could still be effectively maintained. For the multiobjective case, the control usage remained at 4.0 mm/s, identical to the unconstrained case, with only a moderate increase in ITAE and steady-state error. This confirms that for certain trajectories, radial control may be considered dispensable without a significant loss in performance or efficiency, as suggested in Alfriend *et al.* (2010). It is worth noting that for both the complete and the constrained case without radial control, the best optimization strategy remained the same, indicating that this change of control actuator did not significantly alter the optimization landscape, thereby implying flexibility to the results achieved.

In summary, the optimization-based strategies consistently outperform the classical tuning methods. For the unperturbed case, they provide superior tracking accuracy while improving control usage efficiency by approximately 6% for the LQR controller and over 38% for the PID controller when compared to their respective literature-based counterparts. For the perturbed case, where control budget is often a primary design driver, the optimization strategies offer a clear advantage. By prioritizing  $\Delta V$  conservation, the single objective LQR controller reduced the daily  $\Delta V$  by more than 65% compared to the literature approach, which focuses on basic orbit corrections. This significant control acceleration saving is achieved while maintaining acceptable levels of tracking error, underscoring the effectiveness of optimization in balancing performance objectives for long-duration space missions.

## 6 Conclusions

It is inferred, therefore, that it was possible to develop and systematically compare adaptive control strategies for baseline maintenance in multi-satellite synthetic aperture radar formations. This work established a computationally efficient model of the formation flying dynamics, providing the necessary framework for control system analysis. Subsequently, the performance of linear quadratic regulator and proportional-integral-derivative controllers was evaluated, contrasting classical tuning methods from the literature with modern optimization-based approaches. The two primary methodologies, classical and optimized tuning, yielded different outcomes, a result attributed to the distinct performance objectives and system constraints prioritized by each approach.

Analysis of key performance metrics, such as the integral time absolute error (ITAE) for tracking accuracy and the total velocity increment ( $\Delta V$ ), enabled the determination of the superior control configuration for various mission scenarios. For the LQR controller, the optimization-based strategy, specifically, single objective optimization using the particle swarm optimization (PSO) metaheuristic, proved substantially more effective. The numerical results demonstrated considerable enhancements in both tracking precision and delta-V efficiency, particularly under the influence of orbital perturbations and actuator constraints. These improvements ranged from approximately 6% for the unperturbed reference trajectory up to 64% for the perturbed reference trajectory in terms of  $\Delta V$ .

A similar conclusion was reached for the PID controller. Control gains derived from the multiobjective optimization process were better adapted to the complex, coupled dynamics of formation flying. The model employing these optimized gains exhibited a markedly lower ITAE and a more efficient distribution of control effort when contrasted with the controller tuned via classical rules, which struggled to balance performance and control usage. The optimal PID configuration was achieved through multiobjective optimization using the non-dominated sorting genetic algorithm II (NSGA-II). This method effectively navigated the trade-offs between competing objectives and achieved performance comparable to the optimal LQR controller, with  $\Delta V$  improvements of up to 38% for the perturbed reference trajectory.

The observed performance differences, even under nominal conditions, can be at-

tributed to inherent trade-offs in multiobjective problems and the simplifications adopted during modeling. For instance, the state-space model formulation for both controllers involved an approximation by linearizing the relative dynamics, which does not fully capture nonlinear orbital effects such as the differential  $J_2$  perturbation. Furthermore, the analysis of a constrained control architecture, where radial thrust was disallowed, confirmed that system performance is not significantly compromised for certain reference trajectories. This finding suggests that the optimization framework can effectively compensate for actuator limitations, a critical insight for designing cost-effective and resilient small satellite missions.

This study validates that the application of multi-objective optimization algorithms provides a robust and flexible framework for designing adaptive controllers for satellite formation flying. This modern approach consistently outperforms traditional tuning methods and offers a viable pathway toward the implementation of autonomous, real-time controller adjustments in complex, long-duration mission environments. The outcomes and methodologies developed throughout this research also served as the foundation for the paper “Motion Planning Strategies for Safety Procedure of Multi-Satellite Formation Flying Systems”, published in the American Institute of Aeronautics and Astronautics (AIAA) journal, further demonstrating the relevance and applicability of the proposed framework to the broader aerospace research community.

For future research, this study identifies several promising directions to be explored. The first involves enhancing the realism of the system dynamics model, which was simplified in the present analysis. This includes incorporating more detailed thruster and sensor models, as well as accounting for significant orbital effects such as differential atmospheric drag. Another important direction is to extend the framework to formations with a larger number of satellites, where distance-based potential functions can be employed for collision avoidance. Additionally, the proven optimization framework could be applied to investigate other advanced control strategies, including Model Predictive Control, Fuzzy PID controllers, PID controllers with online tuning, and robust control methods. Finally, there is a strong potential to validate the proposed methodologies in a Hardware-in-the-Loop testbed, providing an experimental assessment of their effectiveness in realistic operational conditions.

# References

ACCIARINI, Giacomo; IZZO, Dario; MOOIJ, Erwin. MHACO: a Multi-Objective Hypervolume-Based Ant Colony Optimizer for Space Trajectory Optimization, p. 1–8, 2020. DOI: 10.1109/CEC48606.2020.9185694.

ALFRIEND, K. *et al.* **Spacecraft Formation Flying: Dynamics, Control and Navigation**. [*S. l.*]: Butterworth-Heinemann, 2010. (Elsevier Astrodynamics Series).

AUGER, A.; HANSEN, N. Performance evaluation of an advanced local search evolutionary algorithm. *In*: 2005 IEEE Congress on Evolutionary Computation. [*S. l.*: *s. n.*], 2005. v. 2, 1777–1784 vol. 2. DOI: 10.1109/CEC.2005.1554903.

BANSAL, Hari; SHARMA, Rajamayyoor; PONPATHIRKOOTTAM, Shreeraman. PID Controller Tuning Techniques: A Review. v. 2, p. 168–176, Nov. 2012.

BEASLEY, David; BULLEY, David R.; MARTIN, Ralph R. An Overview of Genetic Algorithms: Part 1, Fundamentals. **University Computing**, Inter-University Committee on Computing, v. 15, n. 2, p. 58–69, 1993.

BIERLAIRE, Michel. **Optimization and Simulation: Multi-objective Optimization**. [*S. l.*: *s. n.*], 2020. <https://www.youtube.com/watch?v=vCaEtY6K61c>. Video lecture published on YouTube. Accessed: 2024-08-26.

BISCANI, Francesco; IZZO, Dario. A parallel global multiobjective framework for optimization: pagmo. **Journal of Open Source Software**, v. 5, n. 53, p. 2338, 2020.

BOAIN, Ronald. A-B-Cs of sun-synchronous orbit mission design, Feb. 2005.

CAPDEROU, Michel. **Handbook of Satellite Orbits: From Kepler to GPS**. [*S. l.*]: Springer International Publishing, 2014.

CHIHA, Ibtissem; LIOUANE, N.; BORNE, Pierre. Tuning PID Controller Using Multiobjective Ant Colony Optimization. **Applied Computational Intelligence and Soft Computing**, v. 2012, Apr. 2012.

- CLOHESSY, W.; WILTSHIRE, R. Terminal Guidance System for Satellite Rendezvous. **Journal of the Astronautical Sciences**, v. 27, n. 9, p. 653–678, 1960.
- CORANA, Angelo *et al.* “Minimizing Multimodal Functions of Continuous Variables with the ‘Simulated Annealing’ Algorithm”. **ACM Transactions on Mathematical Software - TOMS**, v. 15, p. 287, Sept. 1989.
- CURTIS, H.D. **Orbital Mechanics for Engineering Students**. [S. l.]: Butterworth-Heinemann, 2014. (Aerospace Engineering).
- D’ERRICO, M. **Distributed Space Missions for Earth System Monitoring**. [S. l.]: Springer New York, 2012. (Space Technology Library). ISBN 9781461445418.
- DEB, Kalyanmoy *et al.* A fast and elitist multiobjective genetic algorithm: NSGA-II. **IEEE transactions on evolutionary computation**, IEEE, v. 6, n. 2, p. 182–197, 2002.
- EICHHORN, Helge *et al.* A comparative study of programming languages for next-generation astrodynamics systems. **CEAS Space Journal**, v. 10, n. 1, p. 115–123, 2018. DOI: 10.1007/s12567-017-0170-8. Available from: <https://doi.org/10.1007/s12567-017-0170-8>.
- FERRETTI, A.; PRATI, C.; ROCCA, F. Nonlinear subsidence rate estimation using permanent scatterers in differential SAR interferometry. **IEEE Transactions on Geoscience and Remote Sensing**, v. 38, n. 5, p. 2202–2212, 2000.
- FREY, Othmar *et al.* Geometric Error Budget Analysis for TerraSAR-X. *In*:
- HANSEN, Nikolaus. The CMA Evolution Strategy: A Comparing Review. Ed. by Jose A. Lozano. Springer Berlin Heidelberg, p. 75–102, 2006.
- HANSEN, Nikolaus *et al.* Comparing results of 31 algorithms from the black-box optimization benchmarking BBOB-2009. *In*: PROCEEDINGS of the 12th Annual Conference Companion on Genetic and Evolutionary Computation. Portland, Oregon, USA: Association for Computing Machinery, 2010. (GECCO ’10), p. 1689–1696. ISBN 9781450300735. DOI: 10.1145/1830761.1830790.
- HARRIS, Charles R *et al.* Array programming with NumPy. **Nature**, Nature Publishing Group, v. 585, n. 7825, p. 357–362, 2020.
- HOLLAND, John H. **Adaptation in natural and artificial systems: an introductory analysis with applications to biology, control, and artificial intelligence**. [S. l.]: MIT press, 1975.

- HUGHES, Steven P. **General Mission Analysis Tool (GMAT)**. Greenbelt, MD, United States, 2007. Work of the U.S. Government. Public use permitted. Available from: <https://ntrs.nasa.gov/citations/20080045879>.
- KAHLE, Ralph *et al.* Flight Dynamics Operations of the TanDEM-X Formation. *In*: DOI: 10.2514/6.2012-1275094.
- KRIEGER, Gerhard *et al.* TanDEM-X: A Satellite Formation for High-Resolution SAR Interferometry. **IEEE Transactions on Geoscience and Remote Sensing**, v. 45, n. 11, p. 3317–3341, 2007.
- KUMAR, S *et al.* Genetic Algorithm Based PID Controller Tuning for a Model Bioreactor. **Indian Chemical Engineering.**, v. 50, Jan. 2008.
- LIU, G. P.; YANG, J. B.; WHIDBORNE, J. F. **Multiobjective Optimisation and Control**. 1st. [*S. l.*]: Research Studies Press Ltd, 2003. (ENGINEERING SYSTEMS MODELLING AND CONTROL SERIES).
- MITTERMAYER, Josef *et al.* MirrorSAR: An HRWS Add-On for Single-Pass Multi-Baseline SAR Interferometry. **IEEE Transactions on Geoscience and Remote Sensing**, v. 60, p. 1–18, 2022.
- MOREIRA, Alberto *et al.* A Tutorial on Synthetic Aperture Radar. **IEEE Geoscience and Remote Sensing Magazine (GRSM)**, v. 1, p. 6–43, Mar. 2013.
- NAIMI SADIGH, Ali *et al.* Cardinality Constrained Portfolio Optimization Using a Hybrid Approach Based on Particle Swarm Optimization and Hopfield Neural Network. **Advanced Science Letters**, v. 17, p. 11–20, Oct. 2012. DOI: 10.1166/asl.2012.3666.
- NIST/SEMATECH. **e-Handbook of Statistical Methods**. [*S. l.*: *s. n.*], 2023. <https://www.itl.nist.gov/div898/handbook/prc/section2/prc242.htm>. Accessed: 2025-05-26.
- NOGUEIRA PEIXOTO, Maxwell *et al.* On the Exploitation of CubeSats for Highly Accurate and Robust Single-Pass SAR Interferometry. **IEEE Transactions on Geoscience and Remote Sensing**, v. 61, p. 1–16, 2023.
- OGATA, K. **Modern Control Engineering**. 4th. [*S. l.*]: Aeeizh, 2002. (Instrumentation and controls series).
- OGATA, K. **Modern Control Engineering**. 5th. [*S. l.*]: Prentice Hall, 2010. (Instrumentation and controls series).

- PETZOLD, Linda. Automatic Selection of Methods for Solving Stiff and Nonstiff Systems of Ordinary Differential Equations. **SIAM Journal on Scientific and Statistical Computing**, v. 4, Mar. 1983. DOI: 10.1137/0904010.
- RACKAUCKAS, Christopher; NIE, Qing. DifferentialEquations.jl—a performant and feature-rich ecosystem for solving differential equations in Julia. **Journal of Open Research Software**, Ubiquity Press, v. 5, n. 1, 2017.
- RARDIN, Ronald L.; UZSOY, Reha. Experimental Evaluation of Heuristic Optimization Algorithms: A Tutorial. **Journal of Heuristics**, v. 7, n. 3, p. 261–304, 2001. ISSN 1572-9397. DOI: 10.1023/A:1011319115230.
- SHEEHAN, J. P. *et al.* Initial operation of the CubeSat Ambipolar Thruster, p. 1–1, 2015. DOI: 10.1109/PLASMA.2015.7179981.
- STORN, Rainer; PRICE, Kenneth. Differential Evolution – A Simple and Efficient Heuristic for Global Optimization over Continuous Spaces. **Journal of Global Optimization**, v. 11, n. 4, p. 341–359, 1997. ISSN 1573-2916. DOI: 10.1023/A:1008202821328.
- TANG, K.S. *et al.* An optimal fuzzy PID controller. **IEEE Transactions on Industrial Electronics**, v. 48, n. 4, p. 757–765, 2001. DOI: 10.1109/41.937407.
- THAMIR, Luay. Optimal Tuning of Linear Quadratic Regulator Controller Using Ant Colony Optimization Algorithm for Position Control of a Permanent Magnet DC Motor. **Iraqi Journal of Computer, Communication, Control and System Engineering**, v. 20, p. 29–41, Oct. 2020.
- THE MATHWORKS INC. **MATLAB version: 9.13.0 (R2025a)**. Natick, Massachusetts, United States: The MathWorks Inc., 2025.
- THE MATHWORKS INC. **Optimization Toolbox version: 9.4 (R2025a)**. Natick, Massachusetts, United States: The MathWorks Inc., 2025.
- VADALI, Srinivas Rao; VADDI, Sessa Sai; ALFRIEND, Kyle. T. An intelligent control concept for formation flying satellites. **International Journal of Robust and Nonlinear Control**, v. 12, 2002.
- VIRTANEN, Pauli *et al.* SciPy 1.0: Fundamental Algorithms for Scientific Computing in Python. **Nature Methods**, v. 17, p. 261–272, 2020. DOI: 10.1038/s41592-019-0686-2.
- WANG, Dongshu; TAN, Dapei; LIU, Lei. Particle swarm optimization algorithm: an overview. **Soft Computing**, v. 22, p. 387–408, 2017.

---

ZHANG, Qingfu; LI, Hui. MOEA/D: A Multiobjective Evolutionary Algorithm Based on Decomposition. **Evolutionary Computation, IEEE Transactions on**, v. 11, p. 712–731, Jan. 2008. DOI: 10.1109/TEVC.2007.892759.

## FOLHA DE REGISTRO DO DOCUMENTO

1. CLASSIFICAÇÃO/TIPO <p style="text-align: center;">TC</p>	2. DATA <p style="text-align: center;">11 de novembro de 2025</p>	3. DOCUMENTO Nº <p style="text-align: center;">DCTA/ITA/TC-045/2025</p>	4. Nº DE PÁGINAS <p style="text-align: center;">98</p>
5. TÍTULO E SUBTÍTULO: Adaptive Control Strategies for Baseline Maintenance in Multi-Satellite SAR Formations			
6. AUTOR(ES): <b>Mateus Silva Borges</b>			
7. INSTITUIÇÃO(ÕES)/ÓRGÃO(S) INTERNO(S)/DIVISÃO(ÕES): Instituto Tecnológico de Aeronáutica – ITA			
8. PALAVRAS-CHAVE SUGERIDAS PELO AUTOR: Synthetic Aperture Radar; Formation Flying; Control; Optimization.			
9. PALAVRAS-CHAVE RESULTANTES DE INDEXAÇÃO: Radar de abertura sintética; Manutenção; Satélites; Voo em formação; Otimização; Controle; Engenharia eletrônica; Engenharia aeroespacial.			
10. APRESENTAÇÃO: <span style="float: right;">(X) Nacional ( ) Internacional</span> ITA, São José dos Campos. Curso de Graduação em Engenharia Aeroespacial. Orientador: Prof. Dr. Willer Gomes dos Santos; Coorientadora: Prof <sup>a</sup> . Dr <sup>a</sup> . Francesca Scala. Publicado em 2025. 98 páginas.			
11. RESUMO: Multi-satellite Synthetic Aperture Radar (SAR) applications benefit significantly from distributed concepts, such as satellites formation flying. The trend toward small satellite-based SAR missions enables the use of more efficient thrusters, particularly electric and ion engines, for baseline maintenance. This study focuses on optimizing continuous linear controllers for baseline maintenance in multi-satellite SAR formations. The proposed method addresses the challenges in tuning the parameters of continuous linear controllers, such as the weight matrices in the Linear Quadratic Regulator (LQR) and the control gains in Proportional-Integral-Derivative (PID) controllers, by identifying the optimal combination of optimization algorithms and strategies. This approach facilitates the development of a robust and flexible self-tuning regulator capable of handling various state errors, formation geometries, and system perturbations or uncertainties, resulting in an adaptive control strategy for formation flying dynamics. The results of this analysis can be applied to preliminary mission design, ground segment operations, and onboard implementations, enabling efficient and adaptive online tuning.			
12. GRAU DE SIGILO: <p style="text-align: center;">                     (X) OSTENSIVO                      ( ) RESERVADO                      ( ) SECRETO                 </p>			